Novel Imaging Contrast Methods for Hyperpolarized ^{13}C Magnetic Resonance Imaging

by

Galen Durant Reed

DISSERTATION

Submitted in partial satisfaction of the requirements for the degree of

DOCTOR OF PHILOSOPHY

in

Bioengineering

in the

GRADUATE DIVISION

of the

UNIVERSITY OF CALIFORNIA, SAN FRANCISCO

AND

UNIVERSITY OF CALIFORNIA, BERKELEY

Acknowledgements

First and foremost I would like to graciously acknowledge my thesis advisor Dan Vigneron. His devotion to his students and his ability to procure resources creates an environment which completely fosters creativity and allows students to work on the meaningful, interesting projects which balance at the intriguing intersection of biology, physics, and engineering. Thanks a million Dan, for your belief in your people, your dedication to out research, and for standing with us through thick and thin. I believe we made solid progress in this field, and I am supremely confident that your lab will continue to be the leader in hyperpolarized magnetic resonance.

John Kurhanewicz deserves particular praise in this work. John, your devotion to science is supremely contagious. You have a profound interest not only in the science, but in seeing your inventions translated clinically. Your standard for quality is unmatched in this department, as is your supreme friendliness and congeniality. It has been a supreme pleasure working with you.

My two main postdoctoral advisors, Cornelius and Peder, have played an extremely crucial role in my success. I am grateful for all of our coffee breaks, lunch hours, and time spent reflecting on science. I will never be able to go a half a dozen Mission Bay lunch places without thinking about you guys. Particularly, I want to thank you guys for being non-(or at least minimally) judgmental with new ideas, and for providing years of guidance to me during this period. And no speculative scientific discussion would be complete without Kayvan, whose journal club will never be matched as a forum for serious, honest scientific discussion in our lab. I miss you man, and I am supremely confident that you will rise to the top in this field.

Christine and Bertram both indirectly taught me the scientific process, and in working with you guys, I learned the true joy and satisfaction that comes when science works.

Bertram, I am deeply appreciative that I was able to work with you during this period, and I owe you a solid thanks for enabling me to graduate on time! Christine, thanks so much for putting up with us, for always being a positive cubicle mate, for always offering scientific insight, and, of course, for giving me my first live football games. I promise I will never wear black and purple around you!.

I had my first contact with UCSF in the summer of 2007, from my friend's parents' land line telephone in Castiglione Della Pescaia, Italy. This call was to John and Sue Noworolski, both of whom decided that I was worth a shot in their lab. That phone call was the beginning of my complete professional transformation, and I thank you guys immensely for thinking I was worthy of the opportunity! Sue Noworolski truly taught me the foundations of how to navigate my way around UCSF Radiology. Furthermore, she taught me almost everything I ever learned about Linux, C programming, shell scripting, and a million other absolutely essential skills. Sue, I am supremely grateful for your patience in this process! I know I must have been more than a little annoying with my incessant questions.

Christopher Sotto and Danny Lee were the best prostate imaging coworkers you could ask for. I look forward to the next happy hour and Chavos lunch break! Jed, Susan, Michelle, Bernie, Ken, I miss the old days, and I miss you guys. I was truly blessed with the opportunity to work with you guys, and I have many fond memories of our time spent together.

Miki Lustig has a devotion to his work which is truly amazing and contagious. I became acquainted with the MRI field when taking his class and an expert in the field when teaching along side him. He has a profound appreciation for all work in the field, not just that for which he is most well known. Thanks for all your help over the years! You are an excellent role model.

Steve Conolly taught me everything I know about linear response theory and indirectly gave me incredible insight about the strengths and weaknesses of my project. Thanks for your awesome classes, your feedback, and for being a stand up guy.

Our collaborations with clinicians provide meaning to it all. In particular, I am supremely grateful that Zhen Wang has taken the reins of the urea imaging. I want to thank Michael Ohliger and Andrew Taylor for their awesome insights and belief in my project. I will never cease to be amazed at how you guys can come to the lab one day per week and get two weeks of work done in that time! Antionio Westphalen was extremely pleasant to work with during the prostate years, and my first ever publications were with him.

I am supremely grateful for having many awesome mentors both inside and outside the lab: Myriam, Olga, Robert Bok, Sukumar, Lynn, Kristen, Vicky, Eugene O., Jason, Beck, Ilwoo, Peter Shin, Maryam, Maryam, and numerous other I may have forgotten. Thank you guys for being the best coworkers! Hong, Hsin Yu, David, Jessie, Zihan, Eugene M., and Shuyu are are the up and coming all stars, so I better see some awesome work coming from the lab soon!

Many thanks are due to my awesome friends from the L. A. years, particularly Josh, Marcos, Michele, and Federica. I miss you guys, and hope we can do a reunion soon.

I am supremely grateful to my family, and this work is detected to you guys.

to Teresa Anne Reed

Michael Wayne Reed

Meghan Reed

Jennie Livingston

Tracy Valva

Leslie Penglis

Ken and Joanne Marler

Bill and John Valva

in loving memory of Dorothy Reed

you don't know me but you don't like me, you say you care less how I feel. But how many of you that sit and judge me have ever walked the streets of Bakersfield?

Buck Owens

It ain't what you don't know that gets you into trouble. It's what you know for sure that just ain't so

Mark Twain

Abstract

Novel Imaging Contrast Methods for Hyperpolarized ^{13}C Magnetic Resonance Imaging

by

Galen Durant Reed

Doctor of Philosophy in Bioengineering

University of California, San Francisco

Magnetic resonance imaging using hyperpolarized ^{13}C-labeled small molecules has emerged as an extremely powerful tool for the *in vivo* monitoring of perfusion and metabolism. This work presents methods for improved imaging, parameter mapping, and image contrast generation for *in vivo* hyperpolarized ^{13}C MRI. Angiography using hyperpolarized urea was greatly improved with a highly T_2-weighted acquisition in combination with ^{15}N labeling of the urea amide groups. This is due to the fact that the T_2 of [^{13}C]urea is strongly limited by the scalar coupling to the neighboring quadrupolar ^{14}N. The long *in vivo* T_2 values of [^{13}C,^{15} N_2]urea were utilized for sub-millimeter projection angiography using a contrast agent that could be safely injected in concentrations of 10-100 mM while still tolerated in patients with renal insufficiency. This study also presented the first method for *in vivo* T_2 mapping of hyperpolarized ^{13}C compounds. The *in vivo* T_2 of urea was short in the blood and long within the kidneys. This persistent signal component was isolated to the renal filtrate, thus enabling for the first time direct detection of an imaging contrast agent undergoing glomerular filtration. While highly T_2-weighted acquisitions select for molecules with short rotational correlation times, high diffusion weighting selects for those with the long translational correlation times. A specialized spin-echo EPI sequence was developed in order to generate highly diffusion-weighted hyperpolarized ^{13}C images on a clinical MRI system operating within clinical peak-RF and gradient amplitude constraints. Low power adiabatic

spin echo pulses were developed in order to generate a sufficiently large refocused bandwidth while maintaining low nominal power. This diffusion weighted acquisition gave enhanced tumor contrast-to-noise ratio when imaging [1-^{13}C]lactate after infusion of [1-^{13}C]pyruvate. Finally, the first in-man hyperpolarized ^{13}C MRI clinical trial is discussed.

Contents

List of Figures

List of Tables

Chapter 1

Introduction

Magnetic resonance imaging (MRI) is an extremely powerful diagnostic medical imaging tool which provides flexible, tunable imaging contrast. The contrast generation mechanisms possible with MRI are sensitive to a host morphological and physiological parameters. Relaxation time (T_1 and T_2) contrast generates soft tissue detail which is unmatched by any other imaging modality. The resonance frequency of the ^{1}H nucleus is dependent on temperature, thus enabling real time thermometric feedback for ultrasound and radio frequency ablation therapy. Flow sensitivity via pulsed magnetic field gradients enables the only method currently available for angiographic imaging without contrast agents. An extension of this technique allows for noninvasive, directional monitoring of water diffusion *in vivo*; this technique has shown great utility for oncological imaging and for tracking the brain's fiber tracts. Millimolar concentrations of low molecular weight metabolites are possible to spatially map and quantify using ^{1}H spectroscopic imaging. MRI with hyperpolarized ^{13}C contrast agents is an emerging technique which utilizes dynamic nuclear polarization process to enhanced magnetic moment of a ^{13}C labeled compound, thus enabling direct imaging of this compound's distribution and metabolism *in vivo* after intravenous injection. In this thesis, we present new techniques for contrast generation and image quality improvement in the field

of hyperpolarized ^{13}C MRI.

In Chapter 3, we showed that liquid state spin spin relaxation time (T_2) of [^{13}C]urea is highly sensitive to ^{15}N labeling of the amide nitrogens. The T_2 increased by over 200 fold with ^{15}N labeling, indicating that the T_2 of [^{13}C]urea was strongly limited via scalar coupling to the neighboring quadrupolar ^{14}N. This was further proved via correlation time modulation experiments which showed a $T_2 \sim 1/\tau$ relationship for [^{13}C,^{15} N$_2$]urea and a $T_2 \sim \tau$ scaling for [^{13}C]urea. This study presented the first method for *in vivo* projection T_2 mapping of hyperpolarized ^{13}C compounds, thus enabling assessment of ^{13}C T_2 heterogeneity as a source of image contrast. Within the kidney, [^{13}C,^{15} N$_2$]urea showed a very large T_2 increase, while the T_2 of [^{13}C]urea decreased. This was concordant with the differential τ scaling of the two isotopes. The long *in vivo* T_2 values of [^{13}C,^{15} N$_2$]urea were utilized for acquiring the first sub-millimeter projection angiography scans with acquisition times less than 2 seconds and using a contrast agent which could be safely injected in concentrations of 10-100 mM, tolerable even in patients with renal insufficiency.

The study presented in Chapter 4 was motivated by the observation of the extremely long T_2 of [^{13}C,^{15} N$_2$]urea within the kidney. This long T_2 signal component was shown to report directly on glomerular filtration. This dependency was determined by the signal attenuation of a vascular relaxation agent infused 20 seconds after the injection of hyperpolarized urea and 7 seconds prior to imaging. The short T_2 component was strongly attenuated by the chaser injection, but the long T_2 component was unaffected. The long T_2 component within the kidney was shown to be sensitive to urea-specific transporters. Inducing antidiuresis activated the transporters UT-A1 and UT-A3, which in turn maximally concentrate urea to the deep portions of the inner medulla so that concentrated urine can still be produced with minimal loss of water. The T_2 of [^{13}C,^{15} N$_2$]urea was shown to be highly sensitive to diuresis and antidiuresis states. Finally, the long T_2 of the filtered urea pool was utilized for the full 3D encoding of the urea contrast agent within the tubules and collecting ducts. This study demonstrated for the first time a medical imaging contrast agent undergoing detectable

changes with glomerular filtration, thus enabling direct signal differentiation of vascular and filtered components. Furthermore, the novel ^{13}C renography method represented the first time 1 mm^3 isotropic resolution images of a non-^{1}H nucleus were acquired *in vivo* with scan times less than 10 seconds.

In the next studies, novel fast imaging methods were developed to spatially map the conversion of [1-^{13}C]pyruvate to [1-^{13}C]lactate. Chapter 5 demonstrates an EPI method in which the inherently low receiver bandwidth of EPI was utilized to encode both [1-^{13}C]pyruvate and [1-^{13}C]lactate dynamically. Signal models incorporating the exchange were utilized for selection of the optimum flip angle applied to each compound.

Chapter 6 studied diffusion contrast with hyperpolarized [1-^{13}C]pyruvate and [1-^{13}C]lactate. The same EPI sequence described in Chapter 5 was modified with a spin echo, twice-refocused diffusion preparation sequence which provided high diffusion weighting ($b \sim 1000$ s/m^2) in echo times much less than the *in vivo* T_2 measured for [1-^{13}C]lactate. Low power refocusing pulses were developed to enable use of the sequence with currently-existing clinical hardware. This study demonstrated the first highly-diffusion weighted ^{13}C sequence which is playable on a clinical scanner with rapid acquisition time (250 ms per slice).

Finally, Chapter 7 describes the first in-man experiments using a hyperpolarized ^{13}C contrast agent. 1D dynamic, 2D dynamic, and 3D imaging was performed in 31 patients with biopsy-proven prostate cancer. This study represents the first use of hyperpolarized ^{13}C contrast agents in human subjects.

Chapter 8 gives a summary of the fundings. Some preliminary data of current studies and potential future applications are explored.

Chapter 2

Background

2.1 Nuclear Magnetic Resonance

Nuclear magnetic resonance (NMR) is an extremely powerful tool with a wide array of physical, chemical, and biomedical applications. Continuous wave nuclear magnetic resonance phenomenon in liquids and solids was developed independently by Felix Bloch and Edward Purcell [Bloch, 1946; Purcell *et al.*, 1946], a discovery for which the two physicists shared the 1952 Nobel prize. Several years later the field of pulse magnetic resonance was developed by Erwin Hahn [Hahn, 1950] which enabled measurement of molecular diffusion times [Carr and Purcell, 1954], transverse decoherence times [Meiboom and Gill, 1958], and chemical exchange. [McConnell, 1958]. In this section, we describe magnetic resonance mathematically, derive the equations of motion, and give a summary of molecular processes which give rise to relaxation.

2.1.1 The Density Operator and its Time Evolution: Derivation of the Liouville von Nueman Equation

The calculation of the signal behavior of NMR experiments requires using the density matrix, the method of describing a system of mixed quantum states with some thermodynamic weighting. The net inductive signal detected in the receiver will be the result of the thermal mixing of 10^{23} particles, each in a pure state. The derivation of the equation of motion begins with the time-dependent Schrödinger Equation:

$$\hat{H}|\Psi\rangle = i\hbar\frac{\partial}{\partial t}|\Psi\rangle. \tag{2.1}$$

Here, $\hat{H}$ is the Hamiltonian operator, $\hbar$ the reduced Planck's constant, and $|\Psi\rangle$ is the wave function. This is a state vector in Hilbert space. Performing an eigenfunction expansion of $|\Psi\rangle$ gives

$$|\Psi\rangle = \sum_n c_n|\phi_n\rangle, \tag{2.2}$$

where each $|\phi_n\rangle$ satisfies the following eigenvalue problem, also known as the time-independent Schrödinger Equation

$$\hat{H}|\phi_n\rangle = E_n|\phi_n\rangle. \tag{2.3}$$

Here, the E_n are the corresponding energy eigenvalues of each $|\phi_n\rangle$. Since $\hat{H}$ is Hermitian, the $|\phi_n\rangle$ form an orthonormal basis. The quantities c_n are known as probability amplitudes, and their square modulus $|c_n|^2$ represent the probability of the system being found in the state $|\phi_n\rangle$. The expectation value of an operator $\hat{Q} = Q_{n',n}$ can be written as the following

Hilbert space inner product:

$$\begin{aligned}\langle\hat{Q}\rangle &= \langle\Psi|\hat{Q}|\Psi\rangle \\ &= \sum_{n',n}(c^*_{n'}\langle\phi_{n'}|)Q_{n',n}c_n|\phi_n\rangle \\ &= \sum_{n',n}c^*_{n'}c_nQ_{n',n}\langle\phi_{n'}|\phi_n\rangle \\ &= \sum_{n',n}c^*_{n'}c_nQ_{n',n}\end{aligned}$$

A non-pure system represented by pure states $\Psi^{(i)}$ with corresponding probabilities $p^{(i)}$ is

$$\begin{aligned}\langle Q\rangle &= \sum_i p^{(i)}\langle Q_i\rangle \\ &= \sum_{n,n'}Q_{n,n'}\sum_i p^{(i)}c^{(i)*}_{n'}c^{(i)}_n\end{aligned}$$

The density matrix ρ is defined as

$$\rho_{n',n} = \sum_i p^{(i)}c^{(i)*}_{n'}c^{(i)}_n, \tag{2.4}$$

and now the expectation value can be written as

$$\begin{aligned}\langle Q\rangle &= \sum_{n,n'}Q_{n,n'}\rho_{n',n} \\ &= \mathrm{Tr}(Q\rho)\end{aligned}$$

The density matrix has the following equation of motion:

$$\begin{aligned}
\frac{d\rho}{dt} &= \frac{d}{dt}\sum_i p_i|\Psi_i\rangle\langle\Psi_i| \\
&= \sum_i p_i \frac{d}{dt}|\Psi_i\rangle\langle\Psi_i| \\
&= \left(\frac{-i}{\hbar}\right)\sum_i p_i\left[\hat{H}, |\Psi_i\rangle\langle\Psi_i|\right] + \left(\frac{-i}{\hbar}\right)\left[\hat{H}, \sum_i p_i|\Psi_i\rangle\langle\Psi_i|\right] \\
&= \left(\frac{-i}{\hbar}\right)\left[\hat{H}, \rho\right]
\end{aligned}$$

This is the Liouville von Nueman (LVN) Equation. It is customary in NMR calculations to express $\hat{H}$ given in angular frequency (i.e. setting $\hbar = 1$). With this custom, the LVN equation is simply

$$\dot{\rho} = i[\rho, \hat{H}]. \tag{2.5}$$

Although this is non trivial to solve analytically, for a time-independent $\hat{H}$ (i.e. a constant magnetic field), the solution to (2.5) is given by

$$\rho(t) = e^{-i\hat{H}t}\rho_0 e^{i\hat{H}t},$$

which can easily be verified by substitution. Although this solution assumes a time-independent $\hat{H}$, it allows for numerical computation of ρ with any arbitrary $\hat{H}(t)$ by sufficiently fine discretization in the time domain. This is the so-called hard-pulse approximation [Pauly *et al.*, 1991a].

2.1.2 Uncoupled Spin-1/2 Particles: Derivation of the Bloch Equation

For the case of uncoupled spin 1/2 particles, the Liouville von Nueman equation for the density matrix can be expressed as a simple vector differential equation for the bulk mag-

netization. This is an extremely important case, since virtually all ^{1}H NMR experiments in MRI can utilize this simplified approach. A derivation of the Bloch equation is provided in this section.

For the case of spin 1/2 particles, the set of Pauli matrices, along with the identity matrix, form a set of basis vectors.

$$\sigma_x = \begin{pmatrix} 0 & 1 \\ 1 & 0 \end{pmatrix}, \sigma_y = \begin{pmatrix} 0 & -i \\ i & 0 \end{pmatrix}, \sigma_z = \begin{pmatrix} 1 & 0 \\ 0 & -1 \end{pmatrix}, \sigma_I = \begin{pmatrix} 1 & 0 \\ 0 & 1 \end{pmatrix},$$

The nuclear spin vector $\vec{S}$ is

$$\vec{S} = \frac{\hbar}{2}\left(\sigma_x + \sigma_y + \sigma_z\right).$$

The Pauli matrices obey the commutation relation

$$[\sigma_i, \sigma_j] = 2i\epsilon_{ijk}\sigma_k \tag{2.6}$$

The magnetic moment is defined as

$$\vec{\mu} = \gamma\vec{S}, \tag{2.7}$$

with the proportionality constant γ is the gyromagnetic ratio. The density matrix ρ can now be expressed as

$$\rho(t) = r_x(t)\sigma_x + r_y(t)\sigma_y + r_z(t)\sigma_z, \tag{2.8}$$

where $r_x(t)$, $r_y(t)$, and $r_z(t)$ are time-dependent amplitudes, sometimes called the components of the "Bloch Sphere." Although σ_I is technically a basis vector for the $SU(2)$, we do not have to consider its time evolution since and Hamiltonian commutes with σ_I, and by equation (2.5), the time derivative is zero. The magnetic field's three vector components are

the "controls" of the system and is a 3-vector

$$\vec{B} = B_x\hat{x} + B_y\hat{y} + B_z\hat{z}. \tag{2.9}$$

The Hamiltonian of this system is then

$$\begin{aligned} H &= -\vec{\mu}\cdot\vec{B} && (2.10)\\ &= -\gamma\vec{S}\cdot\vec{B} && (2.11)\\ &= -\frac{\gamma\hbar}{2}\left(\sigma_x B_x + \sigma_y B_y + \sigma_z B_z\right). && (2.12) \end{aligned}$$

Substituting equations (2.12) and (2.8) into the Liouville von Nueman (2.5) and expanding with the commutation relations given by (2.6) gives

$$\begin{aligned} \dot{\rho} &= \dot{r}_x\sigma_x + \dot{r}_y\sigma_y + \dot{r}_z\sigma_z && (2.13)\\ &= \frac{i\gamma\hbar}{2}\left[\sigma_x B_x + \sigma_y B_y + \sigma_z B_z, r_x\sigma_x + r_y\sigma_y + r_z\sigma_z\right] && (2.14)\\ &= i\gamma\hbar\left(B_x r_y - B_y r_x\right)(i\sigma_z) + i\gamma\hbar\left(B_x r_z - B_z r_x\right)(-i\sigma_y) + i\gamma\hbar\left(B_y r_z - B_z r_y\right)(i\sigma_x) && (2.15) \end{aligned}$$

Comparing the three components gives the following coupled ODEs

$$\begin{aligned} \dot{r}_x &= \gamma\hbar\left(B_z r_y - B_y r_z\right) && (2.16)\\ \dot{r}_y &= \gamma\hbar\left(B_z r_x - B_x r_z\right) && (2.17)\\ \dot{r}_z &= \gamma\hbar\left(B_y r_x - B_x r_y\right) && (2.18) \end{aligned}$$

Defining $\vec{r} = \hbar\vec{M}$ with $\vec{M}$ the macroscopic magnetization, the above equations are identical to the vector equation

$$\dot{\vec{M}} = \vec{M}\times\gamma\vec{B} \tag{2.19}$$

This is the Bloch equation in $SO(3)$ form.

2.1.3 Solutions of the Bloch Equation Equation: $SO(3)$ Rotations

We can show that the solutions $\vec{M}$ of the Bloch equation (2.19) is unitary by computing the time derivative of $\left|\vec{M}\right|^2$:

$$\frac{d}{dt}\left|\vec{M}\right|^2 = 2\vec{M}\cdot\dot{\vec{M}} \tag{2.20}$$

$$= 2\vec{M}\cdot\vec{M}\times\gamma\vec{B} \tag{2.21}$$

$$= 0. \tag{2.22}$$

Therefore, the time evolution of $\vec{M}$ is necessarily a rotation in 3-space. The solution to the D.C. input (a homogeneous, constant magnetic field) can be calculated explicitly by taking $\vec{B} = B_0\hat{z}$, with B_0 time-independent. (2.19) then becomes

$$\frac{d}{dt}\begin{pmatrix} M_x \\ M_y \\ M_z \end{pmatrix} = \begin{vmatrix} \hat{x} & \hat{y} & \hat{z} \\ M_z & M_y & M_z \\ 0 & 0 & \gamma B_0 \end{vmatrix} = \begin{pmatrix} M_y\gamma B_0 \\ -M_z\gamma B_0 \\ 0 \end{pmatrix} \tag{2.23}$$

This leads to two differential equations for the components of M which are orthogonal to $\vec{B}$:

$$\ddot{M}_x + \left(\gamma^2 B_0^2\right) M_x = 0 \tag{2.24}$$

$$\ddot{M}_y + \left(\gamma^2 B_0^2\right) M_y = 0 \tag{2.25}$$

These are the expressions for the simple harmonic oscillator, and the solutions are

$$M_{xy}(t) = M_{xy,0}e^{i\omega_0 t} \text{ with } \omega_0 = \gamma B_0 \tag{2.26}$$

In general, the solution to the Bloch Equation is independent of the direction of the applied field; the solution is simply a rotation of $\vec{M}$ about the applied $\vec{B}$ field assuming the magnitude of $\vec{B}$ is constant. The component of $\vec{M}$ parallel to $\vec{B}$ remains unchanged.

The modified Bloch equations including relaxation of the transverse components by T_2 and longitudinal component by T_1 is

$$\dot{\vec{M}} = \vec{M} \times \gamma \vec{B} - \frac{1}{T_2} \{M_x \hat{x} + M_y \hat{y}\} - \frac{1}{T_1} \{M_z - M_0)\} \hat{z} \tag{2.27}$$

2.2 NMR Hardware and Signal Detection

The basic NMR system uses multiple coils to control the input $\vec{B}$. A large D.C. coil is utilized to generate polarized spins. Details of the amplitude of this polarization is discussed later. By convention, the coordinate system is chosen so that this field B_0 is along the z axis, and the polarized $\vec{M}$ is along the same axis. An RF coil is used to excite the spins creating a rotation to the x, y plane. The transverse components of $\vec{M}$ are subsequently detected by an additional coil which detects the electro motive force (EMF) induced by the precessing spins. The low-field approximation to the EMF induced in the receiver coil is

$$V \sim \omega_0 \int_{\text{sample}} \vec{B_c} \cdot \vec{M} \, d\tau, \tag{2.28}$$

where $d\tau$ indicates volume integration and $\vec{B_c}$ is the magnetic field produced by driving current through the receiver coil (sometimes called the coil reception profile).

2.3 Magnetic Resonance Imaging.

Magnetic resonance imaging (MRI) is a method utilizing spatially-varying encoding fields to produce a location-dependent Larmor frequency, thus enabling image formation. The

encoding fields, called magnetic field gradients or pulsed field gradients, cause B_z to vary linearly over a certain FOV

$$B_z = B_0 + \vec{G} \cdot \vec{r} \tag{2.29}$$

Solving the total Bloch equation 2.27 after a 90° excitation pulse gives the following expression for the detected receiver signal $s(t)$

$$s(t) = e^{-i\omega_0 t} \int M(\vec{r}) e^{-t/T_2(\vec{r})} e^{-i\gamma \vec{G} \cdot \vec{r}} \, d^3\vec{r} \tag{2.30}$$

Ignoring relaxation, this expression is identical to the spatial Fourier transform of $M(\vec{r})$ with

$$\vec{k}(t) = \frac{\gamma}{2\pi} \int_0^t \vec{G}(\tau) \, d\tau. \tag{2.31}$$

Therefore, the gradients trace out the k space image of M, enabling a simple Fourier transform reconstruction.

2.4 RF pulses

The transverse components of the $\vec{B}$ field are responsible for the resonance phenomenon. When these components are matched in frequency to the amplitude of the longitudinal component, then a rotation of $\vec{M}$ results. When the frequency is not matched, then no rotation occurs, although amplitude modulation of the B_1 field can cause the excited band to be broadened.

2.4.1 Rotating Reference Frame

Virtually all experiments use a constant polarizing field of the form $\vec{B} = B_0 \hat{z}$ which, as shown above, causes a precession of $\vec{M}$ about the z axis with a frequency $\omega_0 = \gamma B_0$. A significant simplification of the problem is achieved by transforming to the reference frame rotating at

$\vec{\omega} = \omega\hat{z}$ [Rabi *et al.*, 1954]. Since this frame is not an inertial frame, the modified derivative operator (sometimes called the gauge-time derivative) must be used:

$$\left(\frac{d}{dt}\right)^* = \frac{d}{dt} + \vec{\omega} \times . \tag{2.32}$$

The Bloch equation now reads

$$\begin{aligned}
\left(\frac{d}{dt}\right)^* \vec{M} &= \dot{\vec{M}} + \vec{\omega} \times \vec{M} \\
&= \vec{M} \times \gamma\vec{B} + \vec{\omega} \times \vec{M} \\
&= \vec{M} \times \left(\gamma\vec{B} - \vec{\omega}\right) \\
&= \vec{M} \times \gamma \left\{ B_x\hat{x} + B_y\hat{y} + \left(B_z - \frac{\omega}{\gamma}\right)\hat{z} \right\}
\end{aligned}$$

This expression has nearly identical form to the lab-frame Bloch equation, but the z component of $\vec{B}$ is reduced by ω/γ. When the reference frame rotates at the Larmor frequency, B_0 is eliminated entirely. Therefore, both B_0-induced precession of $\vec{M}$ can be ignored with rotating frame analysis. Furthermore, the carrier frequency of B_x and B_y can be ignored if these components oscillate at ω_0. Only amplitude modulations and frequency deviations from the Larmor frequency must be accounted for.

2.4.2 Off Resonance Response

Letting $\Delta\omega$ be the deviation from the Larmor resonance frequency in the rotating coordinates, and in the lab frame we have the RF field $\vec{B_1} = B_{1,x}\cos\omega t + B_{1,y}\sin\omega t$, the rotating frame Bloch equation can be written as

$$\dot{\vec{M}} = \begin{pmatrix} 0 & \Delta\omega & -\gamma B_{1,y} \\ -\Delta\omega & 0 & \gamma B_{1,x} \\ \gamma B_{1,y} & -\gamma B_{1,y} & 0 \end{pmatrix} \vec{M} \tag{2.33}$$

Using the substitutions $M_{xy} = M_x + iM_y$, $B_{1,xy} = B_{1,x} + iB_{1,y}$ and assuming that the initial magnetization is aligned with $\hat{z}$, the equation of motion for M_{xy} is

$$\dot{M_{xy}} = -i\Delta\omega M_{xy} + i\gamma B_1 M_z. \tag{2.34}$$

The solution to this first order equation is

$$M_{xy}(t) = i\gamma \int_0^t M_z(\tau) B_1(\tau) e^{i\Delta\omega\tau}\, d\tau. \tag{2.35}$$

This expression is exactly the Fourier transform of the RF envelope $B_1(t)$ when $M_z = M_0 \cos\theta \approx M_0$, or when the flip angle of the RF pulse is small [Pauly *et al.*, 1991b]. This is the linearized version of the Bloch equation. For the case when θ is large, a full simulation of the Bloch equation is necessary to simulate the magnetization response.

2.5 NMR Relaxation

Nuclear magnetic relaxation arises from the large amplitude field fluctuations which occur at the microscopic level. These fluctuations are due to the random rotational tumbling and translational motion of the molecules. The longitudinal relaxation time, also known as "spin lattice" relaxation or T_1, is the time constant of the system to return to thermal equilibrium polarization. The spin-spin relaxation time, also known as transverse relaxation time or T_2, is the time a coherences can be kept alive once it is excited.

The detailed analysis of NMR relaxation starts with the determination of the equations of motion of the density matrix in the rotating frame:

$$\sigma^* = e^{iH_0 t} \sigma e^{-iH_0 t}. \tag{2.36}$$

Here, σ is the density matrix in the lab frame, and H_0 is the Zeeman Hamiltonian arising

from the DC main magnetic field. The master equation in operator form is derived by Abragam [Abragam, 1983]:

$$\frac{d\sigma^*}{dt} = -\frac{1}{2}\sum_{q,p} J_q\left(\omega_p^{(q)}\right)\left[A_p^{-q},\left[A_p^q,\sigma^*\right]\right] \tag{2.37}$$

This formulation is based on the expansion of the random, perturbing hamiltonian

$$H_1(t) = \sum_q F^q(t)A^{(q)},$$

where F^q are random functions of time, and $A^{(q)}$ are the quantum mechanical operators describing the system interactions.

2.5.1 Dipolar Relaxation

By far the most dominant factor in almost all ^{1}H NMR experiments is nuclear-nuclear dipolar coupling. This occurs when the magnetic dipole field produced by one nucleus changes the net field experienced by a neighboring nucleus. With rapidly tumbling molecules, the nuclear field fluctuates, and this change leads to relaxation. The expressions for heteronuclear $(I-S)$ and homonulear $(I-I')$ dipolar relaxation are [Abragam, 1983]

$$\frac{1}{T_{1,II'}} = \frac{1}{10}\left(\frac{\mu_0\hbar\gamma_I^2}{4\pi r^3}\right)^2\left\{J_{II'}(0) + 3J_{II'}(\omega_I) + 6J_{II'}(2\omega_I)\right\} \tag{2.38}$$

$$\frac{1}{T_{2,II'}} = \frac{1}{20}\left(\frac{\mu_0\hbar\gamma_I^2}{4\pi r^3}\right)^2\left\{5J_{II'}(0) + 9J_{II'}(\omega_I) + 6J_{II'}(2\omega_I)\right\} \tag{2.39}$$

$$\frac{1}{T_{1,IS}} = \frac{1}{10}\left(\frac{\mu_0\hbar\gamma_I\gamma_S}{4\pi r^3}\right)^2\left\{3J_{IS}(\omega_I) + J_{IS}(\omega_S-\omega_I) + 6J_{IS}(\omega_S+\omega_I)\right\} \tag{2.40}$$

$$\frac{1}{T_{2,IS}} = \frac{1}{20}\left(\frac{\mu_0 \hbar \gamma_I \gamma_S}{4\pi r^3}\right)^2 \{4J_{IS}(0) + 3J_{IS}(\omega_I) + J_{IS}(\omega_S - \omega_I) + 6J_{IS}(\omega_S + \omega_I)\} \tag{2.41}$$

Distinguishing characteristics of dipolar relaxation are the very strong dependencies on γ and r, the inter-nuclear distance. The r^{-6} dependence implies dipolar interactions over distances of just a few Å can be ignored. In most cases, the strongest dipolar interactions are to neighboring one-bond ^{1}H nuclei. The γ^2 dependence indicates that low-γ nuclei such as ^{15}N will contribute very little to dipolar relaxation even to neighboring nuclei. Furthermore, these low-γ nuclei tend to have very long relaxation times themselves. The high γ of unpaired electrons will cause severe T_1 and T_2 shortening to neighboring nuclei because of this γ^2 scaling.

The spectral density functions $J(\omega)$ describe the time-dependent statistical fluctuation of this dipolar interaction. They are defined as the Fourier transform of the correlation functions $G^{(q)}(\tau)$:

$$J^{(q)}(\omega) = \int_{-\infty}^{\infty} G^{(q)}(\tau) e^{-i\omega\tau}\, d\tau \tag{2.42}$$

and the correlation functions $G^{(q)}(\tau)$ are calculated as

$$\overline{F^{(q)}(t) F^{(q')*}(t+\tau)} = \delta_{q,q'} G^{(q)}(\tau) \tag{2.43}$$

A frequently used approximation is that the correlation functions are exponentially decreasing in time; this leads to Lorentzian spectral densities [Abragam, 1983]:

$$J(\omega) = \frac{2}{5}\frac{\tau_c}{1 + \omega_0^2 \tau_c^2} \tag{2.44}$$

Some qualitative aspects of the spectral density function is shown in Figure 2.1. Since $T_1 \sim 1/J(\omega)$, T_1 tends to be minimum when the Larmor frequency is approximately matched

to $1/\tau$. At very high or very low values of τ (corresponding to solid and liquid states), the dipolar T_1 contribution becomes less efficient and T_1 lengthens. T_2 differs in its dependency on the "D.C." spectral density function $J(0)$ which is just proportional to τ. Therefore, T_2 tends to monotonically decrease with increasing correlation times.

2.5.2 Chemical Shift Anisotropy

Electron shielding of the main magnetic field as seen by the nucleus creates a phenomenon called chemical shift. This results in a very slight ($\sim$ 1 part per million) shifting of the energy levels and, therefore, a shift of the resonance lines. When this interaction is rotationally-invariant, the Zeeman Hamiltonian is

$$H_Z = \gamma\hbar B_0(1-\sigma)I_Z \tag{2.45}$$

where σ represents the amplitude of the shielding. Frequently, this interaction is not rotationally-invariant, and the chemical shift is dependent on the alignment of the molecule with respect to B_0. When the molecule tumbles in solution due to rapid Brownian motion, the chemical shift experienced by the nuclei is constantly changing, and this leads to a relaxation pathway. This pathway is pronounced in nuclei with large chemical shift ranges such as ^{199}Hg, ^{119}Sn, ^{77}Se, and ^{13}C. Mathematically, this anisotropy requires a tensor description of the Zeeman interaction:

$$H_{Z,CSA} = \gamma\hbar\vec{B}\cdot\bar{\bar{\delta}}\cdot\vec{I}, \tag{2.46}$$

where

$$\bar{\bar{\delta}} = \begin{pmatrix} \delta_{xx} & \delta_{xy} & \delta_{xz} \\ \delta_{yx} & \delta_{yy} & \delta_{yz} \\ \delta_{zx} & \delta_{zy} & \delta_{zz} \end{pmatrix} \tag{2.47}$$

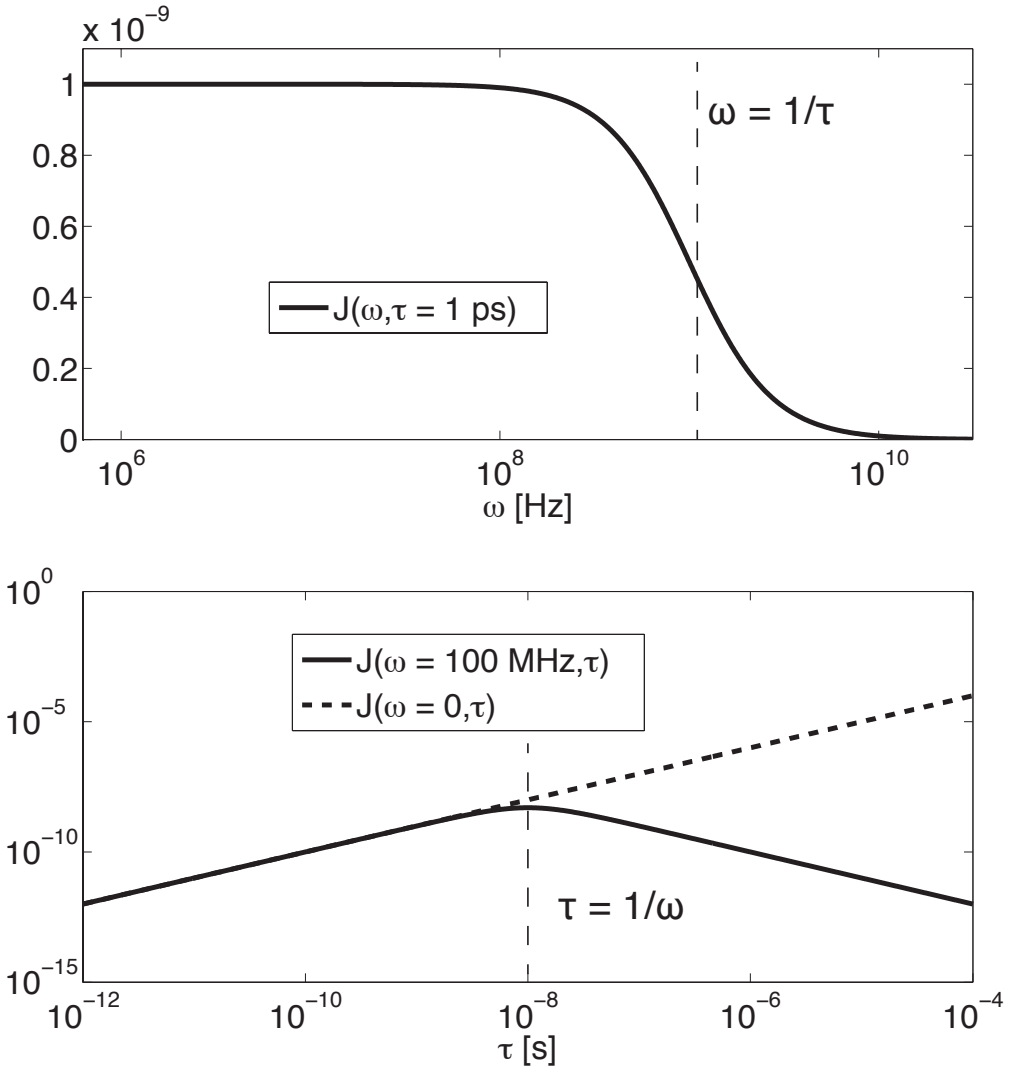

Figure 2.1:
Spectral density functions $J(\omega,\tau) = \tau/(1+\omega^2\tau^2)$ excluding normalization constants. Top: $J(\omega)$ evaluated at $\tau = 1$ ps. Note that $1/\tau$ is effectively a cutoff frequency for the spectral density function. Therefore, at fields corresponding to $\omega_0 \gg 1/\tau$, the spectral density function is diminished, dipolar-mediated T_1 relaxation becomes less efficient, and T_1 increases. Bottom: $J(\omega,\tau)$ and $J(0,\tau)$ as a function of correlation time τ. Since dipolar and CSA mediated T_2 are proportional to $J(0)$, this parameter is useful for visualizing limiting T_2 behavior as a function of τ. $J(\omega,\tau)$ has a maximum at $\omega = \tau$ corresponding to minima in T_1 and T_2. The "D.C." spectral density $J(0,\tau)$ monotonically increases at higher τ. Thus, for restricted rotation environments (corresponding to long τ), T_2 is always a short parameter.

is the chemical shift tensor. The expressions for CSA-mediated relaxation are derived from [Abragam, 1983]

$$\frac{1}{T_1} = \frac{1}{3}\gamma^2 B_0^2 (\Delta\sigma)^2 \left(1 + \frac{\eta^2}{3}\right) \tilde{J}(\omega_0) \tag{2.48}$$

$$\frac{1}{T_2} = \frac{1}{6}\gamma^2 B_0^2 (\Delta\sigma)^2 \left(1 + \frac{\eta^2}{3}\right) \left\{3\tilde{J}(\omega_0) + 4\tilde{J}(0)\right\} \tag{2.49}$$

where

$$\Delta\sigma = \frac{\delta_{xx} + \delta_{yy}}{2} - \delta_{zz} \tag{2.50}$$

is the chemical shift anisotropy, and

$$\eta = \frac{\delta_{yy} - \delta_{xx}}{\delta_{zz} - \delta_{iso}} \tag{2.51}$$

is the asymmetry. The isotropic part of the chemical shift tensor is 1/3 the trace:

$$\delta_{iso} = \frac{\delta_{xx} + \delta_{yy} + \delta_{zz}}{3} \tag{2.52}$$

A characteristic feature of CSA relaxation is the B_0^2 dependency on both R_1 and R_2, which can lead to significant high-field shortening, particularly if the bond is highly anisotropic. In general, CSA is observed with ^{13}C only without attached protons (since the one-bond dipolar effect is often much stronger).

2.5.3 Quadrupolar Relaxation

For nuclei with spin $> 1/2$, the tensor coupling between the nuclear spin and the molecular electric field gradient creates a very strong relaxation mechanism when the atom is not at the center of a tetrahedral or octahedral symmetry. This is due to the fact that quadrupolar nuclei are surrounded by electrons with a non-spherical charge density symmetry. The asymmetric charge density creates a field gradient $\frac{\partial^2 V}{\partial z'^2}$ which exerts torque on the nucleus

(with quadrupolar coupling constant Q). With tetrahedral symmetry, the field gradient vanishes, so this mechanism becomes less important. The relaxation expressions were derived for the $I = 1$ case in [Abragam, 1983]

$$\frac{1}{T_1} = \frac{3}{80}\left(1 + \frac{\eta^2}{3}\right)\left(\frac{eQ}{\hbar}\frac{\partial^2 V}{\partial z'^2}\right)^2 \left\{\tilde{J}(\omega_0) + 4\tilde{J}(2\omega_0)\right\} \tag{2.53}$$

$$\frac{1}{T_2} = \frac{1}{160}\left(1 + \frac{\eta^2}{3}\right)\left(\frac{eQ}{\hbar}\frac{\partial^2 V}{\partial z'^2}\right)^2 \left\{9\tilde{J}(0) + 15\tilde{J}(\omega_0) + 6\tilde{J}(2\omega_0)\right\}. \tag{2.54}$$

For nuclei with a sizable quadrupolar constant Q such as ^{14}N, this mechanism is almost always dominant, and kHz line widths are measured since $T_1 \sim T_2 \sim 1$ ms. Note that in the extreme narrowing case, $\tilde{J}(0) = \tilde{J}(\omega_0) = \tilde{J}(2\omega_0) = 2\tau_c$, and $T_1 = T_2$.

2.5.4 Scalar Coupling

Spin spin coupling of the form $\vec{I} \cdot A \cdot \vec{S}$ can create a pathway for nucleus I if the relaxation rates of nucleus S ($1/\tau_1$ and $1/\tau_2$) are much greater than the coupling constant A.

$$\frac{1}{T_{1,I}} = \frac{2A^2}{3} S(S+1)\left\{\frac{\tau_2}{1 + (\omega_I - \omega_S)^2\tau_2^2}\right\} \tag{2.55}$$

$$\frac{1}{T_{2,I}} = \frac{A^2}{3} S(S+1)\left\{\frac{\tau_2}{1 + (\omega_I - \omega_S)^2\tau_2^2} + \tau_1\right\} \tag{2.56}$$

Note that at low B_0, both $T_{1,I}$ and $T_{2,I}$ are greatly reduced since $\omega_I \sim \omega_S$. At high field, ω_I and ω_S are far apart, so $T_{1,I}$ is not scalar-coupling dominated and decay by other modes (such dipolar and CSA). However, $T_{2,I}$ is still limited by τ_1 even at high field. This pathway is called scalar relaxation of the second kind (SC2). Nuclei I which are J coupled to an exchanging spin S will also undergo shortened relaxation if $1/\tau_e \gg A$, where τ_e is the exchange residence time. This phenomenon is called scalar relaxation of the first kind (SC1). Replacing both

τ_1 and τ_2 with τ_e in the above equations describes the SC1 relaxation.

2.5.5 T_2 Relaxation in Blood

^{1}H NMR transverse relaxation rates (R_2) show strong B_0 and blood oxygenation dependence attributed to the strong paramagnetism of deoxyhemoglobin and the high erythrocyte membrane permeability to water exchange [Thulborn *et al.*, 1982; Meyer *et al.*, 1995; Gomori *et al.*, 1987]. The intracellular protons experience a susceptibility shift which creates effective B_0 gradients for the water exchanging in and out of the cell. This diffusion weighting attenuates R_2 during CPMG spin echo trains. This effect is commonly modeled with the formulation derived by Luz and Meiboom [Luz and Meiboom, 1963]. Under the assumptions that the exchange rate is fast compared to the chemical shift difference (so that only a single resonance is observed) and that the pulse spacing is short enough so that the magnetization is approximately constant between any two echoes, the net transverse relaxation rate is

$$R_2 = R_{2,0} + \left\{1 - \frac{2\tau_e}{\tau}\tanh\left(\frac{\tau}{2\tau_e}\right)\right\}\tau_e \sum_i p_i \delta_i^2 \tag{2.57}$$

where $R_{2,0}$ is the "true" relaxation rate (mediated by dipolar interactions for water protons), τ_e is the exchange time, τ is the pulse repetition rate ($\tau = 2\tau_{CPMG}$), δ_i is the frequency of the ith site, and p_i is the fraction of protons in the ith environment. Determination of the paramagnetic contribution to R_2 has been previously been determined by T_2 relaxation dispersion experiments which measure the R_2 dependence on pulse spacing τ.

2.6 Motion Sensitivity and Diffusion Weighting

In the absence of any transverse applied $\vec{B}$ fields (i.e. in the absence of RF pulses), the Bloch equation for static transverse magnetization $M_+ \equiv M_x + iM_y$ can be written as

$$\frac{dM_+}{dt} = -i\gamma\vec{r}\cdot\vec{G}M_+ - \frac{M_+}{T_2}. \tag{2.58}$$

This model incorporates dephasing from the pulsed field gradients $\vec{G}$ and signal loss from T_2 decay. However, since the gradient-induced phase is dependent on the position vector $\vec{r}$, a moving spin will accumulate phase that is not refocused via a bipolar pulse. This motion is decomposed into 2 parts: one consisting of a laminar flow term of a spin moving at velocity $\vec{v}$, and another term modeling diffusion. A full description of diffusion is incorporated into the diffusion tensor D. The Bloch equation incorporating these effects is

$$\frac{dM_+}{dt} = -i\gamma\vec{r}\cdot\vec{G}M_+ - \frac{M_+}{T_2} + \nabla\cdot D\cdot\nabla M_+ - \nabla\cdot\vec{v}M_+ \tag{2.59}$$

Typically, D contains off-diagonal elements as well as unequal diagonal elements. The case of D diagonal with $D_{xx} = D_{yy} = D_{zz}$ is called isotropic diffusion for which $\nabla\cdot D\cdot\nabla M_+ = D\nabla^2 M_+$. Assuming a solution

$$M_+(t) = \Phi(t)\exp\left(-i2\pi\vec{k}\cdot\vec{r}\right)\exp\left(\frac{-t}{T_2}\right), \tag{2.60}$$

where $\Phi(t)$ is the motion and diffusion induced phase imparted by the gradient pulses, we can see that

$$\begin{aligned}\Phi(t) &= \exp\left[-D\gamma^2\int_0^t\left(\int_0^{t'}\vec{G}(\tau)\,d\tau\right)^2 dt'\right]\exp\left[i\gamma\vec{v}\cdot\int_0^t\left(\int_0^{t'}\vec{G}(\tau)\,d\tau\right)\,dt'\right] \\ &= \exp\left[-4\pi D\int_0^t k(t')^2\,dt'\right]\exp\left[i\gamma\vec{v}\cdot\int_0^t\left(\int_0^{t'}\vec{G}(\tau)\,d\tau\right)\,dt'\right].\end{aligned}$$

The term $4\pi^2\int_0^t|k(t)|^2\,dt$ is typically called the b value and characterizes the diffusion attenuation induced by the gradient pulses. Several characteristics are important for the diffusion weighting of non ^{1}H nuclei. The first is that the actual signal attenuation scales as e^{-bD}. Therefore, highly diffusive compounds will undergo significant attenuation at even modest image resolution (k^2). Typical noble gas diffusivity ranges are 0.06 to 0.14 cm^2/s for ^{129}Xe and 0.86 to 1.8 cm^2/s for ^{3}He [Mugler and Altes, 2013]. By contrast, for pure water in solution, the ^{1}H diffusivity is $\sim 2\times10^{-5}$ cm^2/s. This precludes use of multiple spin echo imaging with SSFP or CPMG sequences due to the strong signal attenuation induced by the imaging gradients [Wild *et al.*, 2006]. At 27°C, ^{13}C diffusivities range from $\sim 0.5\times10^{-5}$ to $\sim 1.5\times10^{-5}$ cm^2/s for molecules with molecular weights of 61 to 390 D in aqueous solution [Koelsch *et al.*, 2013]. The second significant issue for diffusion weighted NMR of non ^{1}H nuclei is that the b value scales as γ^2, so identical gradient pulses played for ^{1}H and ^{13}C will only yield 1/16 the b value for the latter. This can complicate diffusion-weighted NMR for ^{13}C when using gradient-strength-limited systems since the aqueous solution D values as well as γ are comparatively small.

The translational diffusion coefficient depends on temperature T:

$$D = \frac{k_B T}{f}, \tag{2.61}$$

where k_B is Boltzmann's constant, and f is a frictional factor modeled by the Stokes equation $f = 6\pi\eta r$. Combining these expressions gives the Stokes-Einstein relation for translational diffusion

$$D = \frac{k_B T}{6\pi\eta r}, \tag{2.62}$$

where η is the medium viscosity, and r is the molecular radius (modeled here as a sphere). Therefore, D typically increases with higher temperature and decreases with increased molecular weight (which increases r) or solvent viscosity. Of significant note is the factor η depends strongly on temperature [Cheng, 2008; Abragam, 1983] thus complicating the use of D measured at one T to estimate D at a different T.

2.7 Nuclear Polarization

2.7.1 Thermal

The D.C. field B_0 induces a steady-state nuclear magnetic moment M_z parallel to the D. C. field. The magnitude of this moment determines the strength of the acquired signal after excitation and detection. The determination of M_z depend on the energy of the interaction between $\vec{B}$ and the spin magnetic moment:

$$M_z = (\#\text{ nuclei}) \times \left(\frac{\text{magnetic moment}}{\text{single nucleus}}\right) \times (\text{frac aligned with } B_0) \tag{2.63}$$

The magnetic moment of a single nucleus is $\mu = \gamma S = \gamma\hbar/2$ for a spin-1/2. The fraction aligned with B_0 can is determined from thermodynamics. For discrete, multiple energy level system, the probability P_i of finding the system in the i^{th} state is

$$P_i = \frac{e^{-E_i/kT}}{\sum_i e^{-E_i/kT}}, \tag{2.64}$$

where E_i is the energy eigenvalue of corresponding to the i^{th} state. Sometimes the factor $\sum_i e^{-E_i/kT}$ is called Z, the "partition function," which is just a normalization constant. For a single spin-1/2, there are two possible interaction energies:

$$E = \pm\vec{\mu} \cdot \vec{B} = \pm\gamma\hbar B_0/2, \tag{2.65}$$

with the negative energy corresponding to the "spin up" state, and the positive energy corresponding to "spin down." From 2.64, the fraction aligned with B_0 is

$$\text{frac aligned with } B_0 = P_\uparrow - P_\downarrow = \tanh\left(\frac{\hbar\gamma B_0}{2kT}\right). \tag{2.66}$$

At typical lab temperatures ($\sim$ 300 K) and high magnetic fields ($\sim$ 1 T), the quantity $\hbar\gamma B_0/2kT$ is extremely small ($\sim 10^{-6}$). In this regime, $\tanh x \sim x$, so the polarization is proportional to γ, B_0, and inversely proportional to T. Figure 2.2 shows the polarization of ^{1}H, ^{13}C, and electrons as function of temperature in the low-temperature regime.

2.7.2 Dynamic Nuclear Polarization

As Figure 2.2 shows, electronic polarization is a factor of 100 times greater than that of ^{13}C around 1 K. However, using an oscillating field at the appropriate frequency, the $e^- \rightarrow {}^{13}$C transitions can be driven so that the polarizations are nearly equilibrated. This process is called dynamic nuclear polarization, and is an aggregate of several distinct effects, all of which use some coupling between the election and nucleus. This coupling can be isotropic ($H_{iso} = \sum a_{i,j}\vec{I}_i \cdot \vec{S}_j$) or an anisotropic dipolar interaction. The Overhauser effect (OE) was first performed in metals but can be performed in liquids as well. The OE is maximized when the irradiation frequency ω equals ω_e, the EPR resonance frequency. The solid effect (SE) occurs with isolated, non-interacting paramagnetic centers when the anisotropic part of the electron-nuclear interaction Hamiltonian ($\langle H_{aniso}\rangle$) is non-zero averaged over time. The maximal

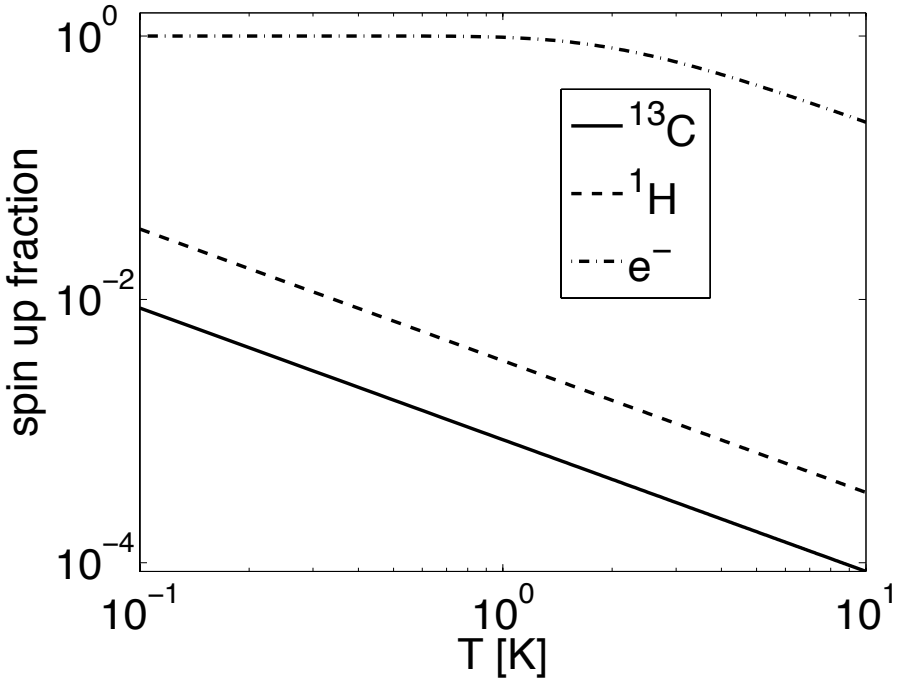

Figure 2.2: Polarization of ^{1}H, ^{13}C, and electrons in the low temperature regime at $B_0 = 3.35$ T. At less than 2 K, electrons are 100% polarized, while ^{1}H and ^{13}C are polarized to $\sim 1\%$.

enhancement is achieved when $\omega = \omega_e \pm \omega_n$, where ω_n is the nuclear Larmor frequency [Wind *et al.*, 1985]. The thermal mixing (TM) effect also requires a non-zero $\langle H_{aniso} \rangle$ and occurs with high radical concentration. In this case, the EPR line is homogeneously broadened. This effect is maximized when $\omega_n \sim \delta$, where δ is the EPR line width, and the optimal irradiation frequency is $\omega_e \pm \delta$ [Wind *et al.*, 1985]. When the electron polarization is sufficiently low so that a linear expansion of the tanh function is valid, rate equations for the electronic and nuclear inverse spin temperatures can be used [Ardenkjær-Larsen *et al.*, 2009; Provotorov, 1962; Wind *et al.*, 1985]. The steady state solution of the Provotorov equation gives an expression for the peak nuclear polarization:

$$\frac{\beta_{eq}}{\beta_L} = \frac{T_{1,n}W(\Delta^2/D'^2)(\alpha_L/\beta_l) + T_{1,e}W + 1}{1 + T_{1,e}W + T_{1,n}W(\Delta^2/D'^2)} \tag{2.67}$$

where $W = \pi\gamma_s^2 B_1^2 g(\Delta)$, $D'^2 = D^2 + (N_I/N_S)I(I+1)/(S(S+1))\omega_I^2$, and $D^2 = \int_{-\infty}^{\infty} \Delta^2 d(\Delta)\, d\Delta$ Here $\alpha, \beta = \hbar/kT$ are the inverse spin temperatures of the electron and nuclei, respectively.

2.7.3 Dissolution Dynamic Nuclear Polarization

The generation of highly polarized nuclear spins in the solid state attained a dramatic increase in possible applications with the development of dissolution systems, in which the polarized sample is rapidly dissolved to liquid state and heated while retaining solid state polarization [Ardenkjær-Larsen *et al.*, 2003]. Provided that the liquid state nuclear T_1 is sufficiently long, the persistent polarization has opened the door to the use of polarized spins as *in vivo* contrast agents.

2.8 Imaging methods for hyperpolarized compounds

2.8.1 Background

In vivo imaging of hyperpolarized nuclei presents several significant challenges for pulse sequence design. Since the Zeeman polarization is many orders of magnitude above thermal equilibrium, hyperpolarized nuclei do not undergo any noticeable M_z recovery from spin lattice relaxation. Instead, the T_1 causes a monotonic polarization decrease over time giving the compound an effective half life. This process can be sped up significantly by RF pulse perturbations. Magnetization steered away from the z axis for signal detection will decay by T_2; if this component is intentionally dephased, then excitation pulses will cause a net shortening of the polarization lifetime leaving only a $\cos\theta$ component along z after each pulse. In addition, during the imaging phase encoding steps, a "steady state" is never achieved due to the lack of T_1 recovery. This will invariably cause a significant windowing of the k space data yielding some point spread blurring from T_1, T_2, or some combination thereof depending on the weighting of the sequence. In general, sequences fall under two main categories: spoiled sequences and those which recycle signal from TR to TR.

2.8.2 Spoiled sequences

A safe strategy for hyperpolarized imaging utilizes a series of small tip angle excitation pulse followed by a signal detection period. The $M_z \rightarrow M_{xy}$ pathway is selected via gradient dephasing (from pulses played at the end of the TR), RF pulse dephasing (from phase advance of the excitation pulses to minimize spin echo and stimulated echo pathways), or both. The simplest implementation if a modification of the gradient echo, sometimes called the SPGR (spoiled gradient echo) or FLASH (fast low angle shot). A diagram of this sequence is shown in Figure 2.3. Typical assumptions are no stimulated or spin echo pathways contaminate the signal, and the M_z remaining at the end of a TR is proportional to $\cos\theta$,

where θ is the flip angle of the excitation. Under these assumptions, the longitudinal and transverse magnetization remaining after N encoding steps is

$$M_{z,N} = E_1^N \prod_{k=1}^{N} \cos\theta_k \tag{2.68}$$

$$M_{xy,N} = E_2 \sin\theta_k M_{z,N-1} \tag{2.69}$$

with

$$E_1 = e^{-TR/T_1}, E_2 = e^{-TE/T_2} \tag{2.70}$$

Although larger θ values can be utilized for increased signal, larger flip angles "burn up" magnetization in early phase encodes, this badly windows the imaging k space data. Novel flip angle ramping strategies have been developed to address the k space windowing, thus creating a flat response for a given number of phase encodes. Ignoring relaxation, it can be shown that the optimal flip angle choice for the kth phase encoding step is [Zhao *et al.*, 1996]

$$\theta_k = \tan^{-1} \frac{1}{\sqrt{N-k}}. \tag{2.71}$$

This sequence, which terminates with $\theta = 90°$, is not only signal optimal, but also yields an ideally flat response over phase encoding steps. When T_1 relaxation is included, there are two possible optimum flip angle strategies [Nagashima, 2008]. One maximizes the total encoded signal

$$\theta_k = \cos^{-1} \sqrt{\frac{E_1^2 - E_1^{2(N-k+1)}}{1 - E_1^{2(N-k+1)}}} \tag{2.72}$$

and another optimizes the flatness of the M_{xy} response:

$$\theta_k = \cos^{-1} \sqrt{\frac{1 - E_1^{2(N-k+1)}}{1 - E_1^{2N-k+1}}} \tag{2.73}$$

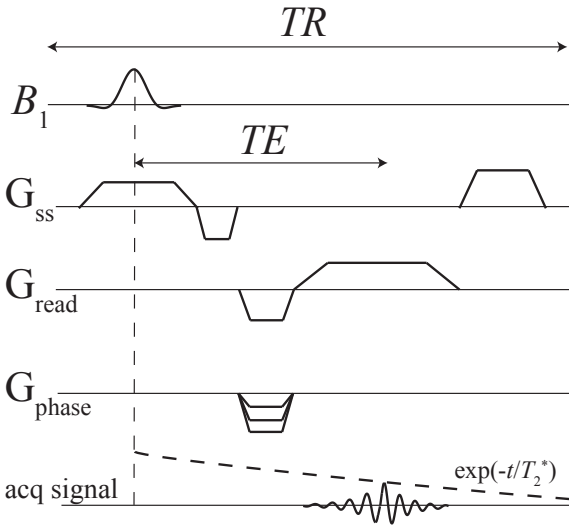

Figure 2.3: A 2D spoiled gradient echo sequence.

Numerous k space readouts have been proposed which efficiently utilize the excited magnetization for image encoding. Among these are multi-echo IDEAL [Reeder *et al.*, 2007], EPI [Cunningham *et al.*, 2008], and spiral [Lau *et al.*, 2010], the latter of which is optimal for echo time minimization. All of these pulse→echo-train-readout sequences strive to maximize the number of k space lines encoded for a given RF pulse. Since they do not rely on refocused recycling of the transverse coherence, the transverse decay time readout is limited

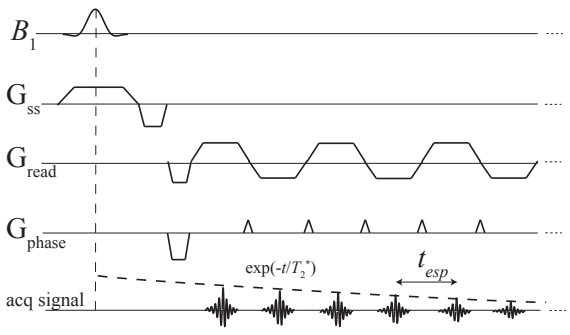

Figure 2.4: A pulse and acquire EPI sequence.

by T_2^*, and the sequence programmer must make an estimate of this parameter in order to match it to the readout duration.

2.8.2.1 RF phase cycling

Note that the above analysis assumed that no stimulated echo or spin echo signal pathways contaminate the detected signal, and only the $M_z \rightarrow M_{xy}$ pathway contributes to the signal. In practice this is never true, particularly for compounds with T_1 or T_2 much larger than TR. This is because over a 3 TR interval, the crusher lobes at the end of the first and second TRs cancel the phase for the middle pulse, which then acts as a spin echo for the third TR. This is the simplest contribution possible from non $M_z \rightarrow M_{xy}$ contributions; over a series of TRs, the number of possible echo contribution pathways increases geometrically. The most commonly used method for the mitigation of spurious pathways is the use of "RF spoiling", which quadratically increments the phase of the nth excitation pulse according to

$$\phi_n = \frac{n(n-1)}{2}c, \tag{2.74}$$

where c is the phase increment. A typically use value of c is 117°, although this parameter is not unique in its ability to suppress spurious echo pathways.

2.8.3 Magnetization-recycled sequences

This class of sequences uses some degree of recycling of transverse signal from TR to TR to achieve large signal to noise ratio benefits. The latter is due to the comparatively long T_2 of ^{13}C compounds *in vivo* [Yen *et al.*, 2010; Reed *et al.*, 2014; Grant *et al.*, 2011; Svensson *et al.*, 2003], which range from $\sim$ 200 milliseconds to many seconds. The steady state free precision (SSFP or TrueFISP) sequence has been utilized for its ease of implementation and tunable T_1 and T_2 weighting. This sequence begins with an RF pulse $\theta/2$ placed $TR/2$ before the first imaging repetition. All subsequent repetitions use flip angle θ spaced TR apart.

Although numerous catalyzation strategies have been proposed for ^{1}H MRI to expedite entry to the steady state, the simple "half angle preparation" works favorable for hyperpolarized compounds, largely due to the fact that a true steady state is never achieved. Instead, hyperpolarized magnetization is imaged entirely on the so-called "transient phase" of the signal response [Scheffler, 2003]. The analytic model derived for an on-resonance spin with an SSFP phase-cycled sequence shows that the signal and the nth phase encoding step is [Svensson *et al.*, 2003]

$$M_{xy,n} = M_{z,0} \sin\frac{\theta}{2}\left[\left(E_1 \cos\frac{\theta}{2}\right)^2 + \left(E_2 \sin\frac{\theta}{2}\right)^2\right]^{n/2}, \tag{2.75}$$

with

$$E_1 = e^{-TR/T_1}, E_2 = e^{-TR/T_2} \tag{2.76}$$

A full model incorporating B_0 dephasing uses state transition matrix multiplications to update the magnetization vector M at half TR intervals. The TR is broken down to 2 sections in order to pick out the transverse components of M in the center of the echo. The combined 2-half TR simulation uses

$$M_{n+1} = AM_n, \tag{2.77}$$

where A is the product of RF rotation (R_x), free precession (R_z), and relaxation decay (E) during the pulse-to-echo period, followed by the echo-to-pulse period:

$$A = R_z\left(\frac{\omega TR}{2}\right) E\left(\frac{TR}{2}\right) R_z\left(\frac{\omega TR}{2}\right) E\left(\frac{TR}{2}\right) R_x(\theta) \tag{2.78}$$

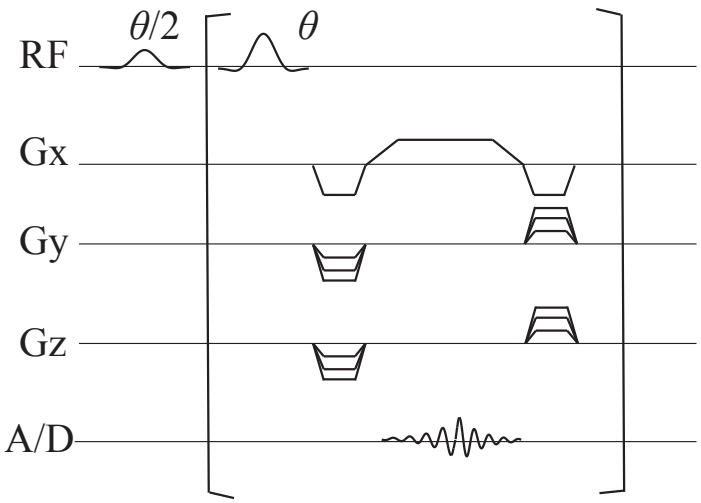

Figure 2.5: An example of a steady state free precession sequence (SSFP). This particular example used 2 dimensional phase encoding and no slice selection.

The x and z rotations are the standard $SO(3)$ matrices:

$$R_x(\theta) = \begin{pmatrix} 1 & 0 & 0 \\ 0 & \cos\theta & \sin\theta \\ 0 & -\sin\theta & \cos\theta \end{pmatrix}$$

$$R_z(\theta) = \begin{pmatrix} \cos\theta & \sin\theta & 0 \\ \sin\theta & \cos\theta & 0 \\ 0 & 0 & 1 \end{pmatrix}$$

and $E(t)$ is a diagonal matrix representing T_1 and T_2 decay

$$E(t) = \begin{pmatrix} e^{-t/T_2} & 0 & 0 \\ 0 & e^{-t/T_2} & 0 \\ 0 & 0 & e^{-t/T_1} \end{pmatrix}$$

Any phase cycling of the RF pulses is incorporated into the sign of θ.

In general the hyperpolarized SSFP sequence has a T_1 and T_2 contrast which is easily tuned with θ. When $\theta = \pi$, the sequence decays via pure T_2 decay, and the sequence behaves as a "fast spin echo" (FSE) or "rapid acquisition with relaxation enhancement" (RARE) sequence [Hennig *et al.*, 1986]. With lower θ, the sequence mixes T_1 contrast. Using $\theta < 180°$ is frequently necessary when the total phase encoding time is long compared to T_2 but not compared to T_1 in order to prevent image blurring and signal loss.

The SNR benefits from SSFP are clear when the limiting case of no relaxation is assumed. In this case, the summed signal from a progressive-flip gradient echo is $\sqrt{N}$, whereas that of the SSFP is N, which represents a $\sqrt{N}$ improvement. One caveat of SSFP is the potential signal loss at $\pm 1/2TR$ off resonance, the well known "banding" artifact. This effect is only observed with lower θ values; $\theta = \pi$ will completely mitigate this effect. The full matrix multiplication model of the off-resonance SSFP behavior is required to model signal banding.

2.8.3.1 RF phase cycling

Alternating the direction (phase) of the B_1 field during magnetization-recycled sequences must be performed so that the signal response is stable when pulse rotation angles are imperfect. The Carr-Purcell-Meiboom-Gill sequence uses a 90° phase advance on all refocusing pulses so that the steady state signal approaches a pure T_2 decay [Carr and Purcell, 1954; Meiboom and Gill, 1958]:

$$\phi_1 = 0,\ \phi_n = \frac{\pi}{2}\ (\forall n > 1)\,. \tag{2.79}$$

This sequence has found widespread use for T_2 weighted clinical imaging [Hennig *et al.*, 1986] when combined with spin echo crushers, slice select, and encoding gradients. These gradient pulses induce longitudinal dephased states which contaminate the pure T_2 weighting to some degree. The steady state free precession (SSFP or TrueFISP) sequence uses alternating polarity with all RF pulses for stabilization:

$$\phi_n = n\pi. \tag{2.80}$$

Chapter 3

High Resolution ^{13}C MRI with Hyperpolarized Urea: In Vivo T_2 Mapping and ^{15}N Labeling Effects

3.1 Abstract

^{13}C steady state free precession (SSFP) magnetic resonance imaging and effective spin-spin relaxation time (T_2) mapping were performed using hyperpolarized [^{13}C] urea and [^{13}C,^{15}N$_2$] urea injected intravenously in rats. ^{15}N labeling gave large T_2 increases both in solution and *in vivo* due to the elimination of a strong scalar relaxation pathway. The T_2 increase was pronounced in the kidney, with [^{13}C,^{15}N$_2$] urea giving T_2 values of 6.3 ± 1.3 s in the cortex and medulla, and 11 ± 2 s in the renal pelvis. The measured T_2 in the aorta was 1.3 ± 0.3 s. [^{13}C] urea showed shortened T_2 values in the kidney of 0.23 ± 0.03 s compared to 0.28 ± 0.03 s measured in the aorta. The enhanced T_2 of [^{13}C,^{15}N$_2$] urea was utilized to generate large signal enhancement by SSFP acquisitions with flip angles approaching the fully refocused regime. Projection images at 0.94 mm in-plane resolution were acquired with both urea

isotopes, with [^{13}C,^{15} N$_2$] urea giving a greater than four-fold increase in SNR over [^{13}C] urea.

3.2 Introduction

Hyperpolarized MR angiography (MRA) and perfusion imaging have interesting properties differentiating them from conventional MRA methods. Unlike ^{1}H MRA which utilizes altered contrast of the water in blood vessels or perfused tissues from radio frequency (RF) preparation pulses, flow-encoding gradients, or the injection of relaxation agents, hyperpolarized ^{13}C magnetic resonance allows for direct imaging of the injected compound. Therefore, this method provides background free signal due to the low ^{13}C natural abundance ($\sim$ 1%) in tissues and the low gyromagnetic ratio (γ) of ^{13}C nucleus. This has enabled several intriguing applications including coronary angiography [Olsson *et al.*, 2006] and perfusion assessment within the brain [Svensson *et al.*, 2003; Johansson *et al.*, 2004a] kidney [Johansson *et al.*, 2004b], and in preclinical cancer models [von Morze *et al.*, 2011a].

Despite the unique advantages of hyperpolarized perfusion imaging, there are several drawbacks. Although the DNP process gives a four order of magnitude gain over Boltzmann polarization, high resolution imaging has been difficult for a number of reasons. First, ignoring the polarization increase, the voltage ϵ induced in the receiver coil by a magnetic moment μ will scale as $\epsilon \sim \mu\omega_0 \sim \gamma^2$. Therefore, the SNR gain from DNP is offset to a great degree by by the inherently low SNR from imaging a low γ nucleus. A second significant challenge is the gradient pulse area requirement for a given resolution, which scales as $1/\gamma$ and necessitates long encoding pulses on clinical MRI systems.

A novel solution to the resolution and SNR limitations is the use of a long T_2 probe used in conjunction with acquisitions employing multiple multiple refocusing pulses [Svensson *et al.*, 2003]. If T_2 is long compared to the imaging time, 180° refocusing RF pulses (preceded by a 90° excitation) are signal-optimal and offer very large SNR improvements.

Previously designed hyperpolarized perfusion probes include (bis-1,1-(hydroxy- methyl)-1-^{13}C-cyclopropane-d_8) (sometimes abbreviated as HMCP or HP001) and tert butanol, both of which have T_2 values in the range of 1.4-4 s *in vivo* [Svensson *et al.*, 2003; Grant *et al.*, 2011]. Since this is greater then the phase encoding time for a single image, projection images can be acquired at 1 mm in-plane resolution with SNR comparable to ^{1}H MRI [Svensson *et al.*, 2003].

Another potential solution to the SNR and resolution limitations is the use of endogenous, non toxic imaging probes such as urea [Golman *et al.*, 2003] which could potentially be injected in very high concentrations. Urea is a normal blood constituent is produced by amino acid metabolism, and is typically found with steady state blood urea of 5.5 ± 2.0 mM (33 ± 12 mg/dL) in healthy humans [Gardner and Scott, 1980] and rats [Anderson *et al.*, 1930]. Urea has been shown to be well-tolerated intravenously in very large doses even in patients with end stage renal failure on dialysis [Johnson *et al.*, 1972].

Although ^{13}C urea is one of the most promising angiographic imaging agents due to its low toxicity, image quality is limited by its comparatively short relaxation times. Scalar coupling of the ^{13}C to the fast-relaxing quadrupolar ^{14}N causes a large T_1 decrease at low fields leading to polarization loss during transport from the polarizer to the imaging magnet [Chiavazza *et al.*, 2013]. Furthermore, the T_2 range measured in this manuscript (0.09 - 0.30 s) is approximately an order-of-magnitude lower than that of typical ^{13}C compounds measured *in vivo* [Svensson *et al.*, 2003; Grant *et al.*, 2011; Yen *et al.*, 2010] and at least two orders-of-magnitude lower than those measured in aqueous solution.

In this study, we found that ^{15}N labeling the amide groups of [^{13}C]urea results in a 250 fold increase in the T_2 in aqueous solution. *In vivo* T_2 mapping experiments showed that [^{13}C,^{15} N_2] urea still had a much longer T_2 than [^{13}C] urea, although the increases were highly spatially heterogeneous. This difference was most apparent in the kidneys, where T_2 values as high 11 ± 2 s were observed with [^{13}C,^{15} N_2] urea. The measured T_2 of [^{13}C]urea was slightly lower in the kidneys than in the blood, with values of 0.23 ± 3 s and 0.28 ± 3 s respectively.

The large T_2 increases associated with ^{15}N labeling were utilized to extract large SNR gains via SSFP imaging with flip angles in the fully refocused regime. [^{13}C,^{15} N$_2$] urea projection images depicted the kidney, aorta, and iliac branches in great detail and gave a factor of 4 SNR improvement over [^{13}C]urea.

3.2.1 SSFP Signal Behavior

The signal behavior of the SSFP sequence applied to hyperpolarized nuclei has been described in detail previously [Svensson *et al.*, 2003; Wild *et al.*, 2006; Golman *et al.*, 2003; Leupold *et al.*, 2009; Bhattacharya *et al.*, 2005; von Morze *et al.*, 2011a]. Typically, a $\theta/2$ preparation RF pulse is placed $TR/2$ before the first imaging repetition, and all pulses have alternating polarity. The flip angle θ tunes the degree of T_1 and T_2 weighing and the total image SNR [Scheffler, 2003; Svensson *et al.*, 2003; Wild *et al.*, 2006], the latter of which is also highly dependent on the relaxation and sequence timing parameters. Assuming a small frequency spread, the analytic model derived by Svensson et al. giving the transverse magnetization at the n^{th} phase encoding step can be used[Svensson *et al.*, 2003]

$$M_{xy,n} = M_{z,0} \sin\frac{\theta}{2}\left[\left(E_1\cos\frac{\theta}{2}\right)^2 + \left(E_2\sin\frac{\theta}{2}\right)^2\right]^{n/2}, \tag{3.1}$$

where $E_1 = \exp(TR/T_1)$, $E_2 = \exp(TR/T_2)$ The image SNR and pixel blurring can be calculated by

$$\text{Signal} = \max|h(x)| \tag{3.2}$$

$$\text{Pixel Width} = \text{FWHM}\,|h(x)| \tag{3.3}$$

with $h(x) = \text{FFT}\{M_{xy}\}$ is the point spread function in the phase encoded direction. The simulated signal and pixel width for [^{13}C] urea and [^{13}C,^{15} N$_2$] urea is shown in Figure 3.1

for various T_2 values measured later in this manuscript.

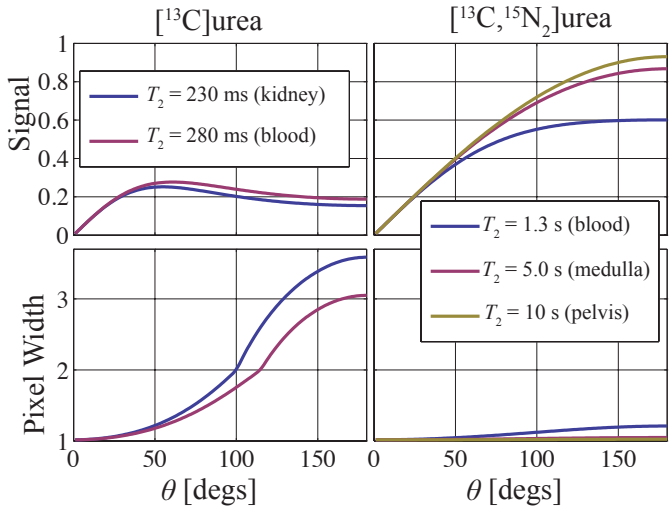

Figure 3.1: The simulated SSFP signal response and pixel width for 96 phase encodes and $TR = 15$ ms, the values used in projection imaging experiments. The data are plotted as a function of SSFP flip angle for both urea isotopes using the estimated T_2 values.

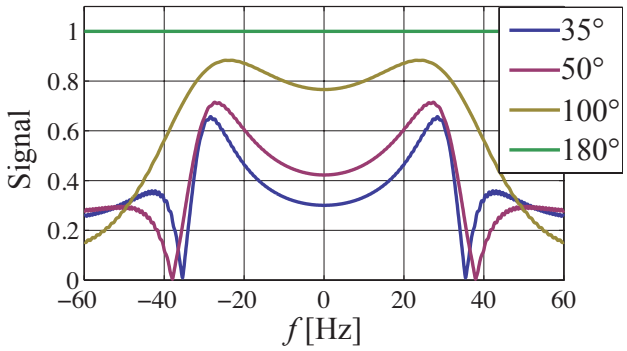

Figure 3.2: Simulated SSFP signal as a function of frequency excluding relaxation and RF selectivity. Due to the small frequency range simulated, RF spectral profile effects were ignored. The signal loss occurring at $\pm 1/2TR$ can be detrimental due to the longer TR required on clinical imaging systems. When T_2 is long compared to the imaging time, the banding can be eliminated with use of larger flip angles.

This model provides a rough estimate of the imaging SNR, since the actual SNR realized will depend also on the k space image and the k space ordering. For N_{PE} phase encodes and

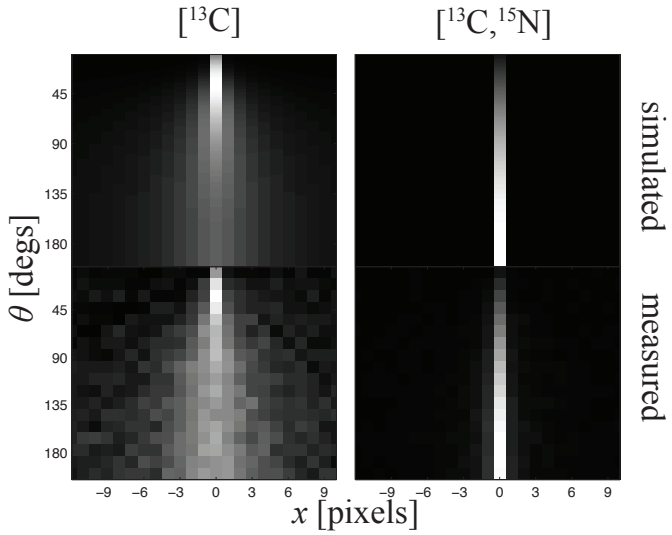

Figure 3.3: The simulated (top) and measured (bottom) point spread functions $h(x)$ as a function of flip angle θ for both urea isotopes.

in the long the limit of $T_1, T_2 \gg N_{PE}TR$, the SSFP signal reduces to $N_{PE}M_0$ when $\theta = 180°$. In this case, the sequence is similar to the CPMG fast spin echo sequence with the signal given by 4.4 giving a pure T_2 decay. With T_2 values less than the imaging time $N_{PE}TR$, a lower value of θ will provide a higher total signal and tighter point spread function. In this regime, signal dropout occurring at $\pm 1/2TR$ off resonance must also be considered. This effect is simulated in Figure 3.2 ignoring relaxation. Clinical MRI systems generally have much stricter requirements on peak gradient amplitude, gradient switching rate, and RF pulse amplitude than high resolution systems designed for animal use. This creates challenges encoding large image matrices with low gyromagnetic ratio (γ) nuclei. Particularly, the TR used for high resolution imaging of low γ nuclei (15 ms for most experiments in this study) was much larger than values used previously for hyperpolarized SSFP on animal systems or for ^{1}H on clinical systems. This creates a significant challenge for imaging short T_2 compounds since at low flip angles and large TR values, the signal-loss banding occurs close to the resonant frequency.

3.2.2 Urea Transverse Relaxation

In solution, the measured ^{13}C transverse relaxation rate $R_2 = 1/T_2$ will be the sum of several pathways of varying strength:

$$R_2 = R_{2,SC} + R_{2,CSA} + \sum_X R_{2,CXdd}. \tag{3.4}$$

$R_{2,CXdd}$ is the dipolar relaxation from nucleus X, which, for the ^{13}C label of urea, will be primarily from the four amide protons. The ^{15}N labeled compound will also have some dipolar contributions from the neighboring nitrogens. $R_{2,CSA}$ is the chemical shift anisotropy contribution which emanates from the variation in Larmor frequency experienced by the carbonyl ^{13}C during molecular tumbling. $R_{2,SC}$ is the pathway which arises from scalar coupling to a fast relaxing (usually quadrupolar) nucleus.

This scalar coupling of the second kind effect was recently shown to attenuate the low-field T_1 of [^{13}C] urea at low B_0 due to the strong ^{13}C-^{14}N scalar coupling constant (14 Hz) and fast ^{14}N relaxation time ($T_{1,N} \sim T_{2.N} \sim 1$ms) [Finer *et al.*, 1972]. This T_1 attenuation becomes negligible at high fields. However, the scalar relaxation pathway affects the T_2 even at high fields [Abragam, 1983]:

$$R_{2,SC} = \frac{4}{3}\pi^2 J^2 S\left(S+1\right)\left(\frac{1}{R_{1,N}} + \frac{R_{2,N}}{R_{2,N}^2 + \Delta\omega^2}\right). \tag{3.5}$$

Here $\Delta\omega = \omega_C - \omega_N$ is the difference in Larmor frequency between the ^{13}C and ^{14}N nuclei, J is the coupling constant in Hz, S is the nuclear spin of ^{14}N. At 3T, the right hand term in equation 3.5 is negligible since $\Delta\omega = 2\pi \times 22$ MHz, and $R_{2,N} \approx 1$ kHz [Chiavazza *et al.*, 2013; Finer *et al.*, 1972]. The left hand term in the parentheses persists at high fields. This interaction has been used to indirectly estimate the relaxation times of halogens and other quadrupolar nuclei whose relaxation times are difficult to measure directly due to

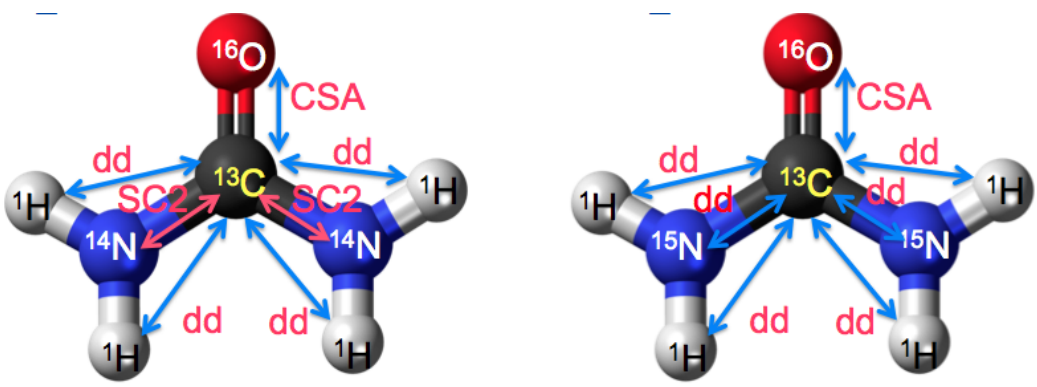

Figure 3.4: [^{13}C] urea and [^{13}C,^{15}N$_2$] urea diagram showing the T_2 relaxation sources.

extremely broad line widths [Sharp and Tolan, 1976; Gryff-Keller and Kubica, 2012]. This is possible since $R_{2,SC}$ scales as $1/T_1$ of the quadrupolar nucleus, so the latter parameter can be estimated if the coupling constant is known. Finer et al. used line broadening due to $R_{2,SC}$ of the amide protons to estimate the rotation correlation time τ of urea in dilute solution [Finer *et al.*, 1972]. In an identical manner, the ^{13}C scalar coupling relaxation can be derived by substituting the nitrogen quadrupolar relaxation term $R_{1,N} = \omega_Q^2\tau$, the ^{14}N nuclear spin $S = 1$, and summing contributions from both nitrogens giving

$$R_{2,SC} = \frac{16\pi^2 J^2}{3\omega_Q^2 \tau}. \tag{3.6}$$

The ^{13}C T_2 due to the scalar coupling effect increases with increasing correlation time τ.

The dipolar and CSA terms can be expressed as

$$R_{2,CSA} + \sum_X R_{2,CXdd} = (\alpha_{CSA} + \alpha_{CHdd} + \alpha_{CNdd})\,\tau \tag{3.7}$$

This model assumes the extreme narrowing limit of the spectral density function $\frac{2}{5}\frac{\tau}{(1+\omega_0^2\tau^2)}$ $\sim (2/5)\tau$. At $B_0 = 3$T and using $\tau = 5$ ps estimated in reference [Finer *et al.*, 1972] for urea in dilute solution at 17° C, the product $\omega_0\tau = 10^{-3}$. The α_{CSA}, α_{CHdd}, and α_{CNdd} terms are the relative strengths of each pathways (in s^{-2}). ^{15}N labeling effectively replaces the $R_{2,SC}$

term in equations 3.4 and 3.6 with a dipolar term $R_{2,CNdd}$ from equation 3.7. The latter pathway is much weaker, and we found the solution aqueous solution T_2 of [^{13}C,^{15}N$_2$] urea (24 ± 4 s) to be at least a factor of 200 greater than that of [^{13}C] urea ($0.090 \pm .014$ s) at 25° C. From equation 3.6, substituting $J = 14$ Hz, $\omega_Q = 2\pi \times 2.24$ MHz [Finer *et al.*, 1972], and $T_{2,SC} = 0.090 \pm .014$ s gives a correlation time $\tau = 4.7 \pm 0.7$ ps, a similar value to that measured using ^{1}H NMR linewidth analysis [Finer *et al.*, 1972].

In vivo T_2 measurements of [^{13}C] urea and [^{13}C,^{15}N$_2$] urea reported in this manuscript differ considerably from those measured in solution. Particularly, the T_2 of [^{13}C,^{15}N$_2$] urea decreases to less than 2 s in blood, while that of [^{13}C] urea increases from 0.09 s in solution to 0.28 s in blood. This can be at least partially explained by the high blood viscosity due to hematocrit which increases τ. The slowed rotation will affect [^{13}C,^{15}N$_2$] urea and [^{13}C] urea in the opposite manner (equations 3.7 and 3.6, respectively). However, there is likely a strong paramagnetic relaxation enhancement due to deoxygenated hemoglobin; this effect has been extensively studied in ^{1}H CPMG experiments. [Thulborn *et al.*, 1982; Gomori *et al.*, 1987; Meyer *et al.*, 1995]. Urea is likely to be nearly as prone to this effect as water due to its high permeability through the red blood cell membrane [Braham, 1983], and the intracellular urea pool has been previously observed by ^{13}C NMR via a small ($\sim$ .2 PPM) frequency shift [Potts *et al.*, 1992].

3.3 Methods

3.3.1 Sample Preparation

Samples of 6.0 M enriched [^{13}C] urea and [^{13}C,^{15}N$_2$] urea (Sigma Aldrich, St. Louis, MO) were prepared in a glycerol solution. This mixture was doped with 15 mM of the trityl radical and and 1.5 mM Gd-DOTA for polarization enhancement.

3.3.2 Hardware

Dynamic nuclear polarization was performed with an Oxford Instruments Hypersense unit (Oxford Instruments, Oxford, UK) operating at 1.3 K and 3.35 T ($\omega_e = 94.1$ GHz). Imaging and phantom experiments were performed using a custom designed ^{13}C/^{1}H transmit/receive birdcage coil placed in the center of the bore of a 3T ($\omega_C = 32.1$ MHz) clinical imaging system (GE Medical Systems, Waukesha, WI). The scanner gradients had a 4 G cm^{-1} peak amplitude, 1.5 G cm^{-1}ms^{-1} peak slew rate.

3.3.3 Phantom Measurements

T_1 and T_2 measurements were performed on hyperpolarized [^{13}C] urea and [^{13}C,^{15}N$_2$] urea in aqueous solution at 37°C, $B_0 = 3$ T. T_2 measurements were performed with a CPMG sequence with $TR = 2\tau_{CPMG} = 10$ ms, 2000 repetitions, 10 A/D samples per repetition, total duration 20 s. T_1 measurements used an adiabatic double spin echo sequence [Cunningham *et al.*, 2007] with a 5° excitation, $TR = 3$s, 64 scans, 192 s total duration. All experiments were repeated three times. Data were fit to a single exponential decay.

T_2 measurements were performed at various bulk viscosity values which were generated by changing ratios of glycerol / water mixtures to approximate the effect of varying the rotation correlation time τ. The viscosity (in cP) was estimated as a function of glycerol fraction and temperature using the empirical relations given by Cheng [Cheng, 2008]. Six 2-mL vials were prepared at differing glycerol concentrations, temperature controlled to 37°C with a water heat bath, mixed with 20 μL hyperpolarized urea solution, and were imaged with the SSFP sequence with $\theta = 180°$. This sequence played the preparation pulse only

once, and during the spin echo train, multiple images were phase encoded:

$$\underbrace{\frac{\pi}{2} - \frac{TR}{2}}_{\text{excitation}} - \underbrace{\left(\underbrace{(\pi \times (-1)^n - TR)^n}_{\text{phase encoding}} \right)^m}_{T_2 \text{ measurement}}. \tag{3.8}$$

Parameters used were $n = 32$ phase encodes per image, $TR = 12$ ms, 384 ms per image, $m = 60$ total images over 23 s. In an identical manner, T_2 measurements of [^{13}C] urea and [^{13}C,^{15}N$_2$] urea in 20%, 40%, and 60% fetal bovine serum were performed.

T_2 measurements were also performed in whole rat blood and plasma. Approximately 2 mL venous blood was drawn from anesthetized rats' lateral tail veins, anticoagulated with K2-EDTA, maintained at 37° C, injected with hyperpolarized urea solution (< 5% total volume), gently mixed, and measured via non-selective CPMG acquisitions. The time between blood draw and NMR measurement was kept less than 10 minutes. This experiment was repeated 5 times for each urea isotope. For an additional 2 cases, the whole blood samples were centrifuged at 1000 RCF for 10 minutes, and the plasma supernatant was gently extracted with a pipette. The T_2 of both urea isotopes were measured in the extracted plasma.

3.3.4 Animal Imaging Experiments

Animal studies were performed under a protocol approved by the UCSF Institutional Animal Care and Utilization Committee (IACUC). Experiments used male Sprague Dawley rats (400 ± 100 g) anesthetized with an isofluorane / oxygen mixture. Anatomic T_2-weighted ^{1}H fast spin echo (FSE) images were acquired in the axial and coronal planes. ^{13}C transmitter calibrations were performed by finding the null of the signal response of a vial containing 1 mL of 8M ^{13}C urea solution placed next to the animal. 107 ± 3 mg samples of urea were polarized for 2.5 hours (approximately 3 buildup-time constants) and then dissolved in 5

mL phosphate buffered saline yielding a final solution of approximately 110 mM. [^{13}C] urea samples were transported to the scanner with a bar magnet to avoid signal loss due to low-field T_1 shortening [Chiavazza *et al.*, 2013]. 3mL (giving approximately 0.3 millimoles ^{13}C) of the hyperpolarized urea solution were injected into a tail vain catheter over 12 s.

3.3.4.1 T_2 Mapping

^{13}C T_2 mapping was performed after infusion of hyperpolarized [^{13}C] urea and [^{13}C,^{15}N$_2$] urea in four different rats. The imaging was initiated 30 s after the beginning of injection (18 s after end of the injection) to ensure a thorough distribution of the contrast agent through the vasculature and kidneys. Furthermore, the long delay time minimized bolus arrival effects during imaging.

As with the phantom experiments, the preparation (excitation) pulse was played only once, and a refocusing pulse train (using SSFP phase cycling) followed in which m dynamic images were acquired (equation 3.8). Due to the greatly varying T_2 values, the TR and resolution were modified for each isotope. [^{13}C,^{15}N$_2$] urea: 64×64 encodes over an 8 cm FOV, $TR = 12$ ms giving 0.768 s per image, $m = 20$ images acquired over 15 s. [^{13}C] urea: 20×20 encodes over an 8 cm FOV, $TR = 10$ ms giving 0.200 s per image, $m = 8$ images acquired over 1.6 s.

In pixels in which the first time point SNR was greater than 30, the time-decay curves after injection of [^{13}C,^{15}N$_2$] urea were fit to the bi-exponential model

$$S(t,x,y) = A_S(x,y)e^{-t/T_{2,S}(x,y)} + A_L(x,y)e^{-t/T_{2,L}(x,y)}. \tag{3.9}$$

$T_{2,S}$, the short T_2 component, was constrained to $[0,2]$ s, and the long component T_2 was constrained to $[2,100]$ s. Fitting was performed in MATLAB using the trust region algorithm (with the function lsqcurvefit). Single labeled [^{13}C]urea was fit to a single exponential decay

$$S(t,x,y) = A(x,y)e^{-t/T_2(x,y)} \tag{3.10}$$

due to the difficulty in bi-exponential fitting with a limited number of data points. As before, fitting was only performed in regions with first time point $SNR > 30$. After fitting, only pixels with $R^2 > .95$ were included in analysis. T_2 values from pixels within the aorta, renal cortex and medulla, and renal pelvis (selected using manually-drawn margins) were fit to a normal distribution to estimate mean and variance. The long T_2 component ($T_{2,L}$) distributions were highly asymmetric and were fit to a type II generalized extreme value (Frechet) distribution

$$\text{PDF}(x) = \frac{1}{s}g(x)^{-1-1/k}\exp\left[-g(x)^{-1/k}\right] \tag{3.11}$$

$$g(x) = 1 + k\frac{(x-\mu)}{s}, \tag{3.12}$$

where μ is the location parameter μ, s is the scale parameter, and k shape parameter. This distribution was chosen since it captures the finite lower limit imposed by constrained bi-exponential fitting, the asymmetry of the distribution, and the long observed tails at high $T_{2,L}$ values. After estimation of s, k, and μ, the means and standard deviations were calculated as $\mu - s/k + (s/k)g_1$ and $(s/k)\sqrt{g_2 - g_1^2}$, respectively, with $g_n = \Gamma(1-nk)$ and $\Gamma(z) = \int_0^\infty t^{z-1}e^{-tz}\,dt$

3.3.4.2 SSFP imaging SNR comparison

To measure the improvement in image quality associated with the longer T_2 of [^{13}C,^{15}N$_2$] urea, repeat *in vivo* hyperpolarized imaging experiments with [^{13}C] urea and [^{13}C,^{15}N$_2$] urea were performed back-to-back in six different animals. All imaging was initiated 20 s after the start of the injection. Similar to previous implementations [Svensson *et al.*, 2003], the

acquisition was aligned in the coronal plane with no slice-select gradients (projection mode) and phase encoding set along the right / left dimension to avoid image aliasing. 96×96 ($n = 4$) and 192×96 ($n = 2$) images were acquired with $TR = 15$ ms, $TE = 7.5$ ms, 4.8 ms data acquisition time per TR. All acquisition had a 208 Hz / pixel receive bandwidth. Since this value is much greater than the 19 Hz J-coupling constant of [^{13}C,^{15} N$_2$] urea, no imaging SNR loss was expected from the AX$_2$ spectral splitting. [^{13}C,^{15} N$_2$] urea acquisitions used $\theta = 180°$, and [^{13}C] urea acquisitions used $\theta = 35°$. These values were picked to maximize the signal using the aqueous solution T_2 values, and as we will show, the latter value was slightly sub-optimal for *in vivo* T_2 values. One experiment in which [^{13}C] urea was imaged with $\theta = 35°, 50°, 70°$ and $180°$ was performed to highlight the need for lower θ values with the short T_2 urea. All experiments used a 3.2 ms time-bandwidth product = 4 windowed sinc pulse which gives a $\theta = 180°$ rotation on resonance at 0.6 G.

Identical to the sequences proposed previously [Svensson *et al.*, 2003], images were acquired dynamically using a "tip back" pulse in order to store magnetization along z during delay periods. This is similar to driven equilibrium sequences which speed T_1 recovery by steering any remaining transverse coherence back to z after signal detection. In practice, the imaging phase encodes must be followed by both a θ and a $\theta/2$ pulse since the inter-pulse delay is $TR/2$:

$$\underbrace{\left(\underbrace{\frac{\theta}{2} \rightarrow \frac{TR}{2}}_{\text{preparation}} \rightarrow \underbrace{(\theta \times (-1)^n \rightarrow TR)^n}_{\text{phase encoding}} \rightarrow \underbrace{(-\theta) \rightarrow \frac{TR}{2} \rightarrow \frac{+\theta}{2}}_{\text{tip back}} \rightarrow \text{delay period}\right)^m}_{\text{dynamic imaging}} . \qquad (3.13)$$

As shown above, SSFP phase cycling is maintained in the last two pulses.

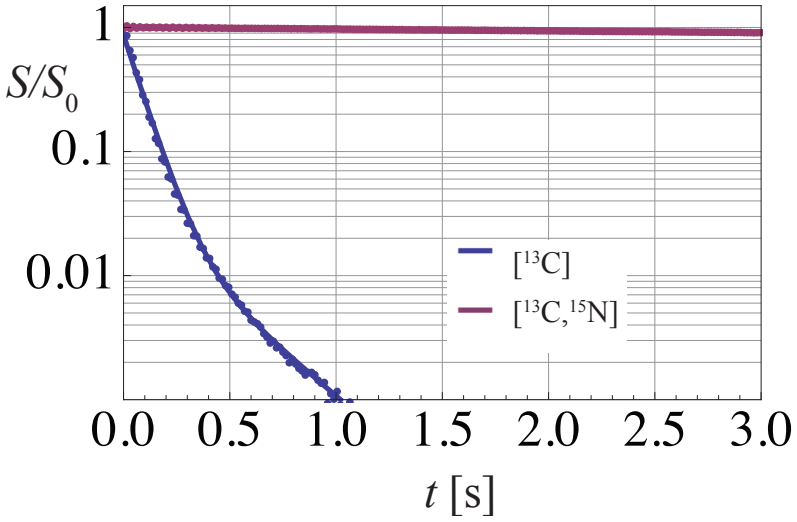

Figure 3.5: $[^{13}C]$ urea and $[^{13}C,^{15}N_2]$ urea CPMG decay curves measured in hyperpolarized samples in aqueous solution. $[^{13}C]$ urea consistently showed a slightly longer T_2 component consisting of $\sim 1\%$ of the total hyperpolarized signal likely arising from the natural abundance ^{15}N (giving rise to a factor of ~ 2 extension of T_2).

3.4 Results

3.4.1 Phantom Measurements

Table 3.1 gives aqueous solution T_1, T_2, and polarization measurements. The T_2 values of $[^{13}C]$ urea and $[^{13}C,^{15}N_2]$ urea differed substantially in solution, with the differences being highest in dilute aqueous solutions. Both compounds showed similar T_1 values. The polarization of $[^{13}C]$ urea was slightly lower and showed more variability from run to run. Even though the sample was transported with a bar magnet, there was likely some residual scalar coupling T_1 relaxation during transport. Figure 3.7 shows the measured T_2 in whole blood, serum, plasma, and water. The blood and plasma values are also listed in Table 3.1. Fetal bovine serum caused some relaxation enhancement of $[^{13}C,^{15}N_2]$ urea, which is likely due to reduced τ or some degree of protein binding. The $[^{13}C,^{15}N_2]$ urea T_2 was greatly reduced between plasma and whole blood indicating a strong relaxivity from red blood cells.

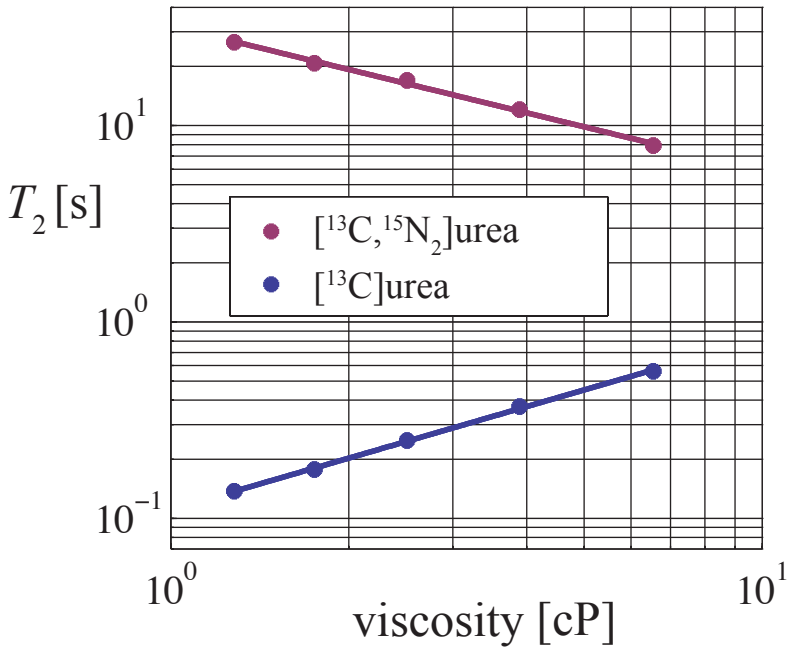

Figure 3.6: Hyperpolarized urea T_2 values as a function of macroscopic viscosity. The removal of the scalar relaxation pathway via ^{15}N labeling gives $[^{13}\mathrm{C},^{15}\mathrm{N}_2]$ urea a much larger T_2 as well as a differing T_2 dependence on correlation time (which should be approximately linear with viscosity).

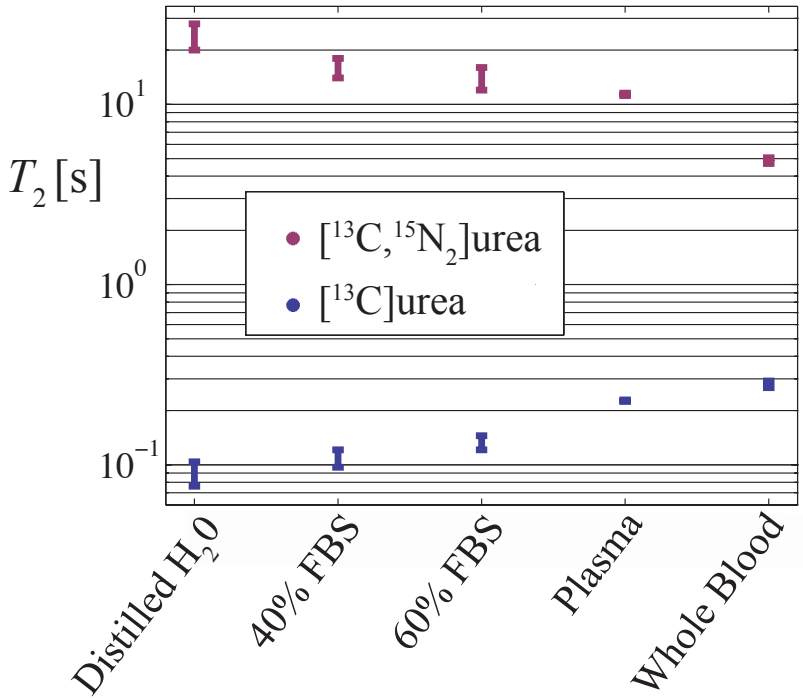

Figure 3.7: Hyperpolarized urea T_2 values in whole blood, serum, plasma, and water. The $[^{13}C,^{15}N_2]$ urea T_2 is greatly reduced in whole blood compared to plasma indicating a strong relaxivity effect from red blood cells.

Figure 3.6 shows the T_2 behavior of both urea isotopes with modulation of the correlation time via changing the bulk solution viscosity. The scalar coupling pathway clearly dominates the $[^{13}C]$ urea T_2. Since the rotational correlation time and viscosity are linearly related for approximately spherical molecules from the Debye-Hückel relation, from equations 3.4, 3.6, and 3.7 the T_2 of $[^{13}C,^{15}N_2]$ urea should scale approximately as η^{-1} and that of $[^{13}C]$ urea should scale as η^{+1}. The actual powers measured from fitting the data in Figure 3.6 were $-0.73 \pm .20$ and $0.87 \pm .05$, respectively. Some deviation of the expected powers of -1 and 1 is expected due to the well known discrepancies between macroscopic and microscopic in solution viscosities [Bloembergen *et al.*, 1948]. Furthermore, $[^{13}C]$ urea will have some weak contribution from dipolar and CSA which will scale as η^{-1}.

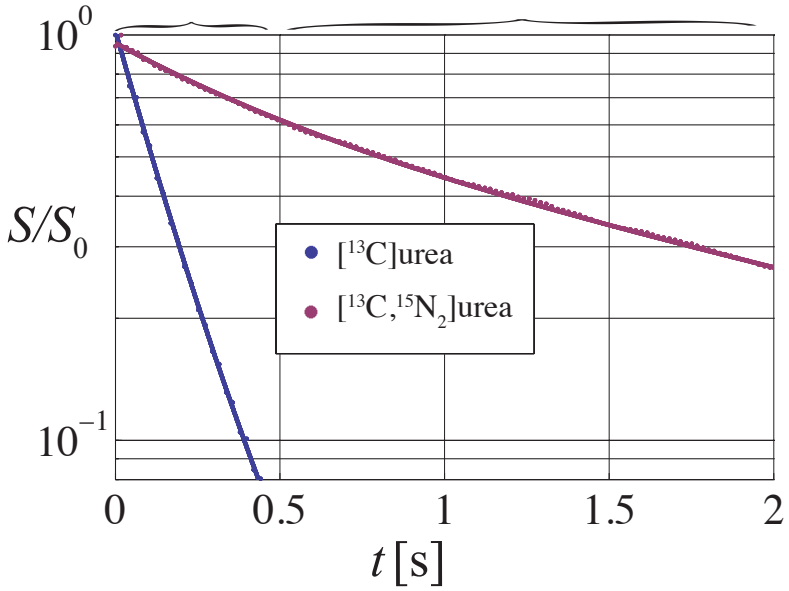

Figure 3.8: *In vivo* non-selective *in vivo* CPMG decay curves measured 10 s after intravenous hyperpolarized injection in Sprague Dawley rats. The $[^{13}\mathrm{C},^{15}\mathrm{N}_2]$ urea isotopes showed a short T_2 component (left brace) which contributed approximately 30% of the total signal. This signal was tentatively assigned to urea within the red blood cells.

Table 3.1: Relaxation and Polarization Measurements in Solution ($B_0 = 3$T, 37°C):

	$[^{13}\mathrm{C}]$ urea	$[^{13}\mathrm{C},^{15}\mathrm{N}_2]$ urea
T_1(aqueous) [s]	46 ± 1	44 ± 1
T_2(aqueous) [s]	$.09 \pm .01$	24 ± 4
T_2 (plasma) [s]	$.23 \pm .01$	11 ± 1
T_2 (whole blood) [s]	$.24 \pm .01$	$4.9 \pm .2$
Polarization at 25 s	$19 \pm 5\%$	$22 \pm 2\%$

3.4.2 In vivo Experiments

3.4.2.1 T_2 mapping

Results from T_2 mapping experiments are shown in Figure 3.10. The $[^{13}\mathrm{C},^{15}\mathrm{N}_2]$ urea experiments showed a largely short scale ~ 1.3 s $T_{2,S}$ decay throughout the animal which is

presumed to be the vascular urea component. Bi-exponential fitting showed the long $T_{2,L}$ component almost completely isolated to the kidneys. The large mean values of these components are given in Table 3.2. While these values are potentially contaminated by collection of the agent into the inner regions of the kidney during the imaging time, the longer T_2 are believable since signal likely represents that from the glomerular filtrate. Since the filtrate is free from red blood cells and plasma proteins some recovery of the solution T_2 can be expected. The filtered urea in the medulla and cortex is primarily in the tubules and medullary interstitium, so some restriction of motion will likely cause a reduced τ and T_2 shortening compared to that dilute solution. However, in the renal pelvis, the large liquid pool will give a reduced τ and virtually all the solution T_2 is recovered. The short T_2 component observed in the kidney likely arises from blood above and below the kidney (due to the projection imaging mode) and possibly also from the renal vasculature. Some long T_2 component was observed in the inferior aorta and femoral branches. This is likely due to RF transmitter drop-off causing some T_1 contamination to the decay curve. However, slower flow could also be a factor.

Due to the much shorter T_2 of [^{13}C] urea, the T_2 mapping images had to be acquired with a much coarser resolution. With the limited number of time samples available, bi-exponential fitting was not possible. However, a slightly shorter mean T_2 within the kidney compared to that measured in the aorta was be observed. This is concordant with solution measurements that show that [^{13}C] urea and [^{13}C,^{15}N$_2$] urea respond to differences in τ in the opposite manner.

Table 3.2 summarizes the histogram fitting of the T_2 mapping experiments. The distributions of [^{13}C,^{15}N$_2$] urea $T_{2,S}$ were approximately normal within the kidney, and the $T_{2,S}$ measured from the medulla and renal pelvis had very similar mean values. $T_{2,S}$ values within the aorta were slightly higher. This is potentially due to the fact that the aorta is fed superiorly from the heart, which in these experiments was at the edge of the transmitter. $T_{2,L}$ distributions within the kidney were highly asymmetric and were fit to a Frechet

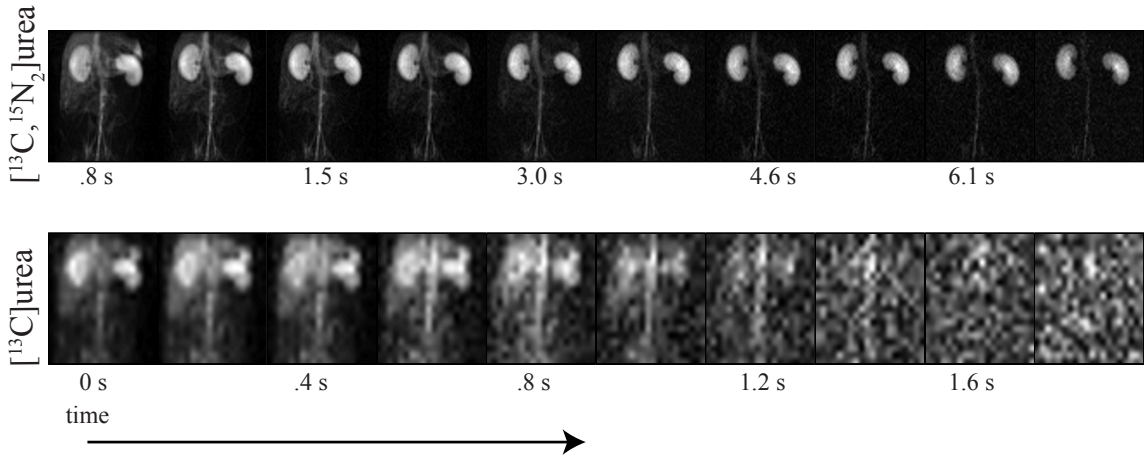

Figure 3.9: $[^{13}\mathrm{C},^{15}\mathrm{N}_2]$ urea and $[^{13}\mathrm{C}]$ urea images during T_2 decay conditions. $[^{13}\mathrm{C},^{15}\mathrm{N}_2]$ urea shows substantial detectable signal in the kidneys at late time points. The kidney is the first organ to attenuate in $[^{13}\mathrm{C}]$ urea images, and only the aorta is visible at later time points. This is indicative of the differing differing τ dependence for each isotope.

distribution. $T_{2,L}$ values had a similar shape parameter k in the medulla and pelvis. Since there was no though-slice localization, it is not possible to determine whether the asymmetry of the distributions represents some geometry factor (stemming from summing all the pixels through the kidney in one dimension), medulla/pelvis partial voluming, or an actual distribution reporting on a physiological parameter. In all likelihood, the decays show more than two characteristic decay times. The reported mean $T_{2,L}$ in the pelvis of 11.0 ± 1.8 s is likely an underestimate since the $T_{2,L}$ parameter also incorporated the faster relaxing medulla immediately above and below the pelvis. Determination of all the characteristic decay times is very difficult, however, due to the ill-conditioned nature of multi-exponential fitting.

3.4.2.2 SSFP Imaging Comparisons

In one rat, hyperpolarized $[^{13}\mathrm{C}]$ urea was imaged with varying θ values. These images are shown in Figure 3.11 along with the SNR values measured in the aorta and kidney. With

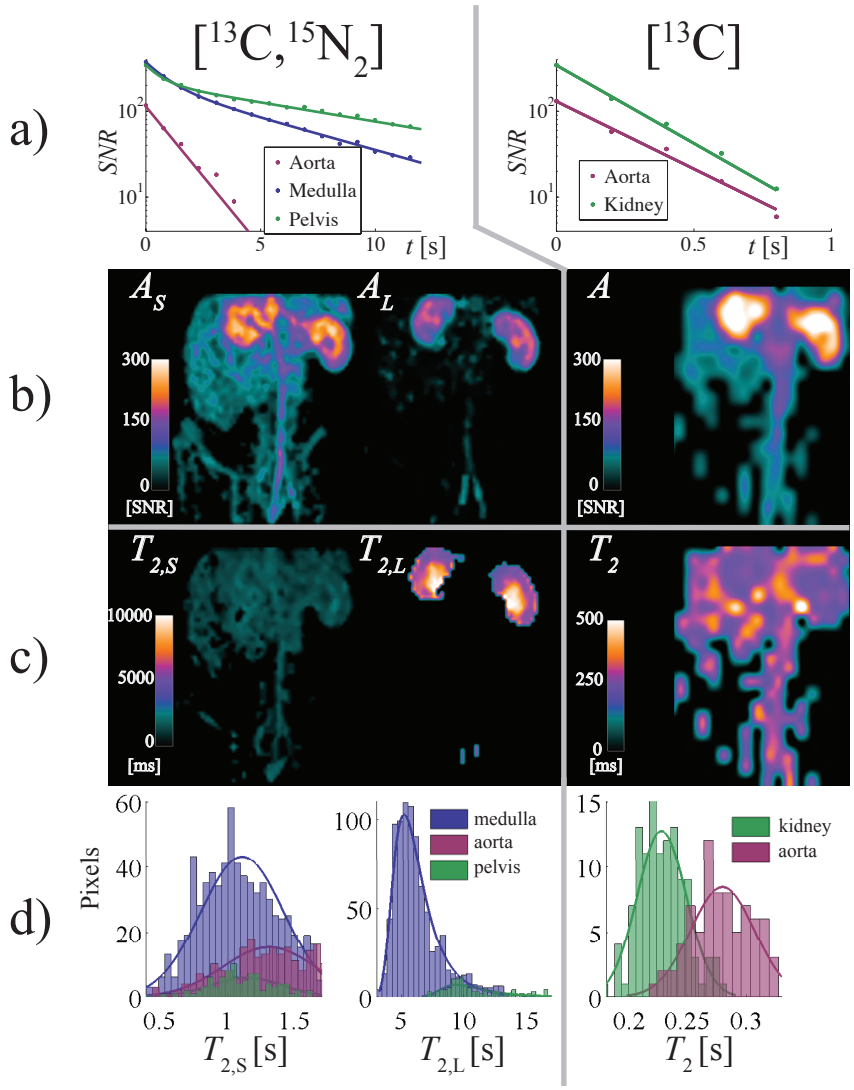

Figure 3.10: a) single pixel T_2 decay curves each both urea isotopes measured in the aorta, medulla, and renal pelvis. The $[^{13}\mathrm{C},^{15}\mathrm{N}_2]$ urea decay shows a bilinear slope, and the fast decay rate is similar to that measured in the aorta. This is likely due to the blood above and below the kidney. Signal within the blood fit well to single exponential decays. b) the fitted amplitudes given by equations 3.9 and 3.10. The long T_2 amplitude A_L is almost completely localized to the kidneys. c) T_2 maps (in ms). The $[^{13}\mathrm{C},^{15}\mathrm{N}_2]$ urea experiments showed extremely long T_2 components in the kidney, with the greatest values measured in the renal pelvis. The $T_{2,L}$ map was thresholded using the A_L values. The cortex and medulla showed similar values. $[^{13}\mathrm{C}]$ urea showed slightly lower T_2 values in the kidneys. d) histograms showing T_2 distributions of all pixels within the medulla, aorta, and renal pelvis for all 4 rats. $T_{2,L}$ values approaching the pure solution T_2 of 20 s were detected in some pixels in the renal pelvis.

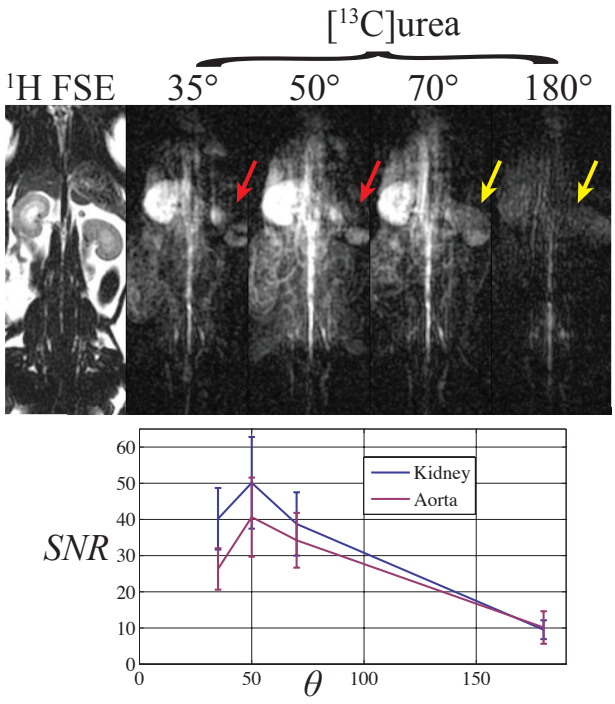

Figure 3.11: Hyperpolarized [^{13}C] urea imaged using an SSFP sequence with multiple θ values (top) highlighting the difficulty in using high flips for the short T_2 urea. Mean SNR values (bottom) are shown with error bars representing standard deviation for the given organ. Only the right kidney SNR values were used due to the banding artifacts (red arrow) in the left kidney. At flip angles sufficiently high to elmininate the banding (yellow arrows), the overall SNR is greatly reduced from a stronger T_2 weighting. The shape of the curves are similar to their simulated counterparts in Figure 3.1, top left.

the lower θ necessary for imaging the short T_2 urea at high resolution, the images were susceptible to signal drop-off from banding artifacts. At flip angles sufficiently high to alleviate the banding, the overall signal is greatly decreased due to T_2. The SNR curve resembles its simulated counterpart in Figure 3.1, top left, indicating an SNR-optimal θ around 50°. Although the $\theta = 35°$ used for imaging comparisons was slightly sub-optimal, only an additional $20 - 30\%$ signal increase can be expected with use of a higher flip. Furthermore, as indicated in Figure 3.1, bottom left, blurring effects will become very problematic in this regime. The image SNR was too low to detect significant blurring, however. A potential solution for yielding favorable signal behavior when the imaging time is much greater than

Table 3.2: T_2 Distributions *in vivo*. † shape parameter of the Frechet Distribution.

	parameter	location	mean$\pm\sigma$ [s]	$k^{\dagger}$
[^{13}C,^{15} N$_2$]	$T_{2,L}$	Pelvis	11.0 ± 1.8	$.13 \pm .09$
	$T_{2,L}$	Medulla	6.28 ± 1.27	$.13 \pm .03$
	$T_{2,S}$	Pelvis	$1.14 \pm .38$	-
	$T_{2,S}$	Medulla	1.15 ± 0.42	-
	$T_{2,S}$	Aorta	1.31 ± 0.34	-
[^{13}C]	T_2	Kidney	0.231 ± 0.026	-
	T_2	Aorta	0.279 ± 0.027	-

T_2 is the use of progressive flip angle SSFP acquisitions. [Deppe and Wild, 2012]. This method would require a good estimate of T_2 for flip angle calculations which may introduce difficulty when multiple, greatly varying T_2 values are present.

Figure 3.13 shows high resolution imaging comparisons of [^{13}C] urea and [^{13}C,^{15} N$_2$] urea for two different comparisons. Resolution was sufficient to discern the aorta, renal, common and external iliac, medial sacral, and femoral arteries in all [^{13}C,^{15} N$_2$] urea images. The kidneys showed a mean SNR of 260 ± 100. [^{13}C] urea images had lower SNR expected from the use of lower flip angles; however, in many cases, the SNR difference between [^{13}C] urea and [^{13}C,^{15} N$_2$] urea images differed substantially more than the factor of ~ 3 expected from simulations (Figure 3.1). There was evidence of banding artifact with the use of lower flip angles; this was significant in the image showen Figure 3.13, bottom right. In the upper right image in Figure 3.13, this artifact is less detrimental but is still present in the region near the iliac branch.

Some differences in contrast are noted in the SSFP images acquired at different flip angles which is expected based on the differing T_2 weighing. SSFP images acquired with lower flip angles tended to have more diffuse background signal; this can be seen in Figure 3.13 comparing the bottom two images. The source of this background is unclear, but may

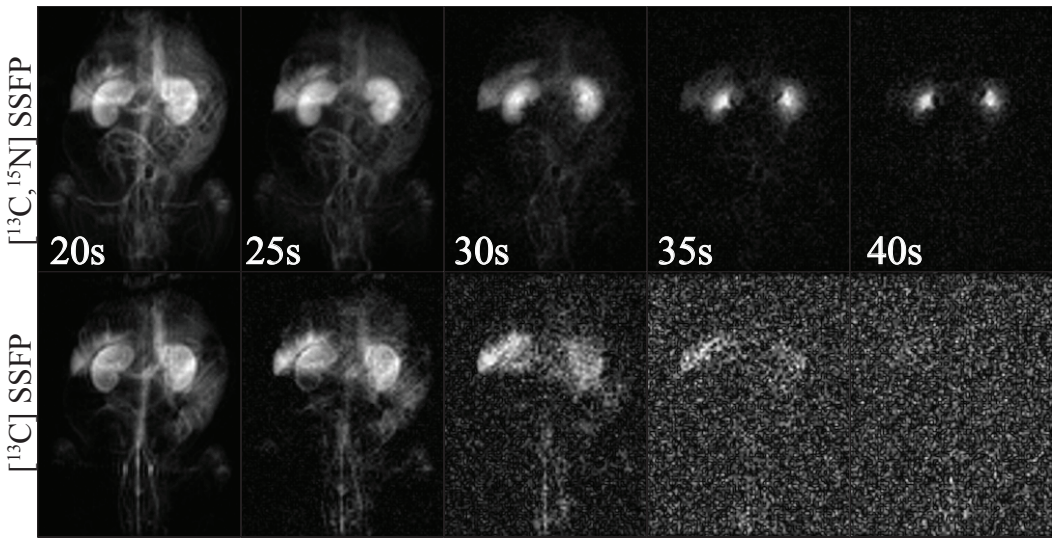

Figure 3.12: SSFP dynamic imaging using the tip back driven equilibrium pulses in order to store polarization along z during the delay periods (equation 3.13). The acquisition time per image was 1.4 s, and a 4 s delay was placed between images. [^{13}C] urea acuisitions used $\theta = 35°$, and [^{13}C,^{15}N$_2$] urea used $\theta = 180°$

it may represent capillary signal with short T_2.

Figure 3.14 shows the mean and standard deviation of SNR values measured in the aorta and kidneys of each imaging comparison. Since the dose was not normalized to the animal mass, there is significant subject-to-subject SNR variability. The lower plots in Figure 3.14 show the ratio of the SNR values measured in each subject which should normalize to the dose variations. Large variations are observed even in the SNR ratios which is inevitable due to some differences in sample transport time, run-to-run polarization levels, and residual scalar coupling relaxation which diminishes [^{13}C] urea polarization. However, all [^{13}C,^{15}N$_2$] urea showed at least a doubling in SNR, with a mean increase of 4.9 ± 0.6 in the kidneys and 4.7 ± 1.0 in the aorta.

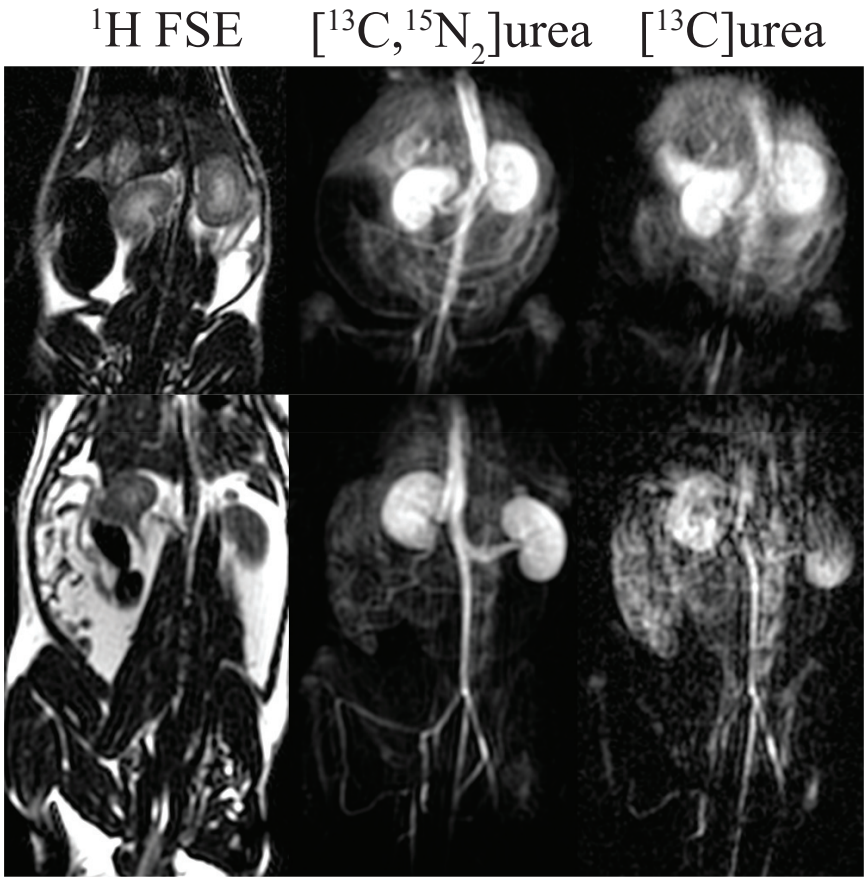

Figure 3.13: Projection imaging at 0.94 mm in-plane resolution. Top: localizer, $[^{13}\mathrm{C}]$ urea, and $[^{13}\mathrm{C},^{15}\mathrm{N}_2]$ urea images acquired with a 9 cm FOV. Higher SNR and reduced blurring is observed in the $[^{13}\mathrm{C},^{15}\mathrm{N}_2]$ urea image. The $[^{13}\mathrm{C}]$ urea shows some signal loss due to banding artifact towards the iliac branch. Bottom: $[^{13}\mathrm{C}]$ urea and $[^{13}\mathrm{C},^{15}\mathrm{N}_2]$ urea images acquired over a 9×18 cm FOV. The kidneys were slightly anterior and posterior of the localizer slice. The $[^{13}\mathrm{C}]$ urea shows much lower SNR also likely due to banding. The $[^{13}\mathrm{C},^{15}\mathrm{N}_2]$ urea image clearly depicts the aorta and its inferior branches. Virtually all $[^{13}\mathrm{C},^{15}\mathrm{N}_2]$ urea images showed signal through the femoral arteries with some enhancement in the knee. Spinal vasculature is also depicted in the bottom center image.

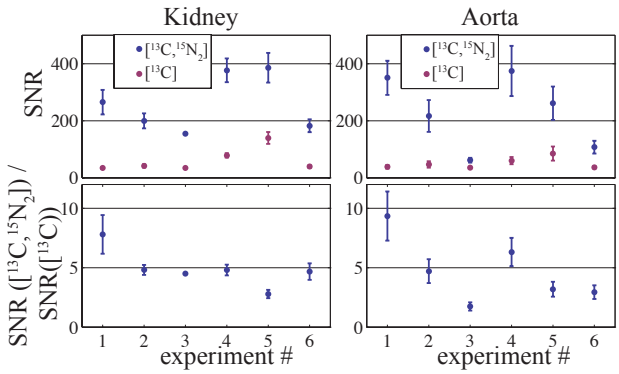

Figure 3.14: mean SNR values in the kidney and aorta for each SSFP imaging experiment with error bars representing the standard deviations. The SNR ratios ($[^{13}\mathrm{C},^{15}\mathrm{N}_2]$ urea to $[^{13}\mathrm{C}]$ urea) are shown on the bottom. Although the SNR ratio ideally should normalize for dose variations, large run-to-run variability is still observed likely due to changes in polarizer/scanner transport time and polarization variations

3.5 Discussion

The high sensitivity of hyperpolarization is offset by the low intrinsic sensitivity of the ^{13}C nucleus, requiring large doses. Therefore, some estimate of the safety of this dose level is warranted to estimate its potential clinical translatability. As mentioned in the introduction, steady state blood urea concentrations of 5.5 ± 2.0 mM (33 ± 12 mg/dL) are typical in healthy humans and rats. For experiments conducted in this study, the estimated blood urea concentration after bolus injection was 12 ± 3 mM (71 ± 20 mg/dL) which was calculated from the 400 ± 100 g mass of the animals used in the study and their estimated blood volumes of 25 ± 6 mL[Lee and Blaufox, 1985]. This value is approximately double the steady state blood urea concentration. The worst-case anticipated safe dose can be inferred from a study by Johnson et al. [Johnson *et al.*, 1972] in which patients with advanced stage renal failure were loaded with urea (added to the dialysate) to maintain steady state blood urea concentrations of 181-600 mg/dL for periods of 7-90 days. Doses of less than 300 mg/dL were well tolerated, while doses from 300-600 mg/dL were associated with malaise, vomiting, and headache [Anderson *et al.*, 1930; ure, 2005]. Based on these results, we expect doses at least

four times higher than those used in this imaging study to be well tolerated in patients with advanced renal failure. This figure is almost certainly an underestimate since the patients from the Johnson et al. study were maintained at high urea doses for multiple days. Subjects with normal kidney function will also certainly tolerate much larger doses.

In order to extract the large SNR increases from increased T_2, long trains of refocusing pulses were used. The SAR of this sequence compared to that used for ^{1}H imaging can be roughly estimated by assuming a uniform sphere with diameter long compared to the wavelength ($\lambda = 9.3$ m for ^{13}C at 3T). Using this model, the power dissipated in the sphere scales as $\omega_0^2 B_1^2$ [Collins and Wang, 2011]. Compared to ^{1}H, ω_0 is reduced by a factor of γ_c/γ_h, the ratio of the gyromagnetic ratios, and the peak B_1 is increased by the same factor for a given flip angle. Therefore, the ^{13}C spin echo trains have similar SAR as the ^{1}H sequence with identical pulse widths, pulse time-bandwidth products, and timing parameters. The large TR values necessary for the larger imaging gradient lobes imply that the SAR is actually lower than that of a typical CPMG imaging sequence for ^{1}H.

Although all imaging in this manuscript was performed in projection mode so that slice profile effects would not contaminate T_2 and SNR measurements, extension to multi slice or 3D imaging should be straight forward. Multi slice imaging was performed in several previous hyperpolarized SSFP implementations [Wild *et al.*, 2006; von Morze *et al.*, 2011a; Olsson *et al.*, 2006; Johansson *et al.*, 2004b]. For isotropic resolution, 3D imaging should also be possible, but due to the larger number of phase encoding steps, a flip angle less than 180° will likely be required.

All T_2 values measured in this manuscript must be considered effective T_2 values due to the numerous factors confounding measurements. Given the SSFP signal response given by equation 4.4, RF transmitter variations will deviate θ from 180° thus adding some T_1 weighting to the signal decay. Over a series of spin echo pulses, the net transverse relaxation

rate can differ significantly from the true R_2. The diffusion attenuation can be expressed as

$$\tilde{R}_2 = R_2 + \frac{b(t)D}{TR} + \frac{1}{12}D\gamma^2\bar{G}^2TR^2 \tag{3.14}$$

where R_2 is the true rate, $\tilde{R}_2$ the observed rate, $b(t) = (2\pi)^2 \int_0^t \left|\vec{k}(t')\right|^2 dt'$ with $\vec{k}(t) = \frac{\gamma}{2\pi}\int_0^t G(t'), dt'$ is the diffusion weighting due to imaging gradients [Wild *et al.*, 2006], and the term $(1/12)D\gamma^2\bar{G}^2TR^2$ represents the diffusion through local B_0 variations (modeled as a constant gradient $\bar{G}$) [Carr and Purcell, 1954]. Although the diffusion term on the left restricts the flip angle choice for hyperpolarized noble gases [Wild *et al.*, 2006] due to D values in the range of 0.1-2 cm^2/s [Mugler and Altes, 2013], the diffusivity of ^{13}C labeled small molecules in solution is between three and five orders of magnitude lower. While this makes liquid state ^{13}C diffusion weighted imaging more difficult on a clinical scanner due to the difficulty in achieving large signal attenuation, this is a favorable characteristic for multiple spin echo imaging since the diffusion weighing will not widen the point spread significantly. The apparent diffusion coefficient for urea was measured to be 1.54×10^{-3} mm^2/s at 27°C [Koelsch *et al.*, 2013]. Given the total b value $b\,(N_{PE}TR) = 6.5$ s/mm^2 integrated over all frequency and phase encoding pulses over 96 repetitions, the diffusion weighting is $\exp\left[b\,(N_{PE}TR)\,D\right] \approx 0.99$. Although the imaging gradient weighting is likely negligible, the microscopic diffusion term likely contaminates T_2 measurements to some degree due to the relatively long (10-15 ms) TR values used and the potentially large gradient $\bar{G}$ experienced by the urea molecule in its transport in and out of the red blood cell. This effect is difficult to quantify *in vivo*; previous studies isolating this effect used T_2 dispersions experiments which measure the dependency of T_2 on $TR = 2\tau_{CPMG}$ [Thulborn *et al.*, 1982; Gomori *et al.*, 1987; Meyer *et al.*, 1995].

Bulk flow parallel to the imaging gradients will induce some phase, and if this phase not coherent within a voxel, this will lead to some signal loss. The frequency encoding gradients in SSFP sequences are first-moment flow compensated, so constant-velocity flow along the

frequency encoded direction is fully rephased. The phase encode gradients had a peak first moment $\int_0^{TR} G(\tau)\tau, d\tau$ of 0.039 s/cm, leading to a $\sim 2^\circ$ phase shift for a 1 cm/s velocity. Although this value is quoted for the outer k space lines, some destructive interference from phase-induced flow over 96 phase encodes (acquired over 1.4 s) could lead to signal loss. This is very likely the source of the large discrepancy of T_2 values measured in whole blood (Table 3.1) and *in vivo* (Table 3.2). In addition to the potential signal attenuation due to flow and diffusion effect, there is likely some lengthening of the measured T_2 in the inner regions of the kidney due to collection during the imaging time.

The extremely long T_2 values measured within the kidney is in itself a potential source of interesting imaging contrast. In this study we were not able to definitively attribute the long T_2 component to urea within the filtration and collecting system. However, this seems very likely given the anatomical distributions of the long T_2 component. Relaxation time gradients between the cortex, medulla, and pelvis are well known from ^{1}H experiments [Kundel *et al.*, 1986], but the direct measurement of urea within the blood and filtered pools could be a powerful tool for assessment of the urea concentrating function of the kidney.

3.6 Conclusion

This study demonstrated a greatly increased imaging SNR of hyperpolarized ^{13}C urea associated with ^{15}N labeling of the amide nitrogens. The SNR increase was due to a very large T_2 increase associated with the elimination of a strong scalar coupling relaxation pathway, and this allowed for SSFP acquisitions with flip angles in the fully refocused regime on a clinical scanner with large minimum TR constraints. Projection images were acquired with in-plane resolution of 1 mm with SNR of 230 ± 120 in the aorta and 260 ± 100 in the kidney. *In vivo* T_2 mapping showed spatially heterogeneous T_2 values, with values of 1.3 s typical in the blood and greater than 10 s observed in the kidney.

3.7 Appendix

Given the short T_2 of [^{13}C] urea, the RF- and gradient-spoiled FLASH sequence was tested as a possible imaging strategy for this compound. This acquisition has found widespread use in hyperpolarized noble gas imaging where the effective T_2 is greatly attenuated due to high molecular diffusivity and strong diffusion attenuation induced by imaging gradients. These factors confound SNR enhancement via transverse coherence recycling from TR to TR. The constant-flip FLASH sequence has been shown to provide inferior SNR behavior with the longer relaxation times found with ^{13}C nuclei [Svensson *et al.*, 2003]. This study tested the FLASH sequence with progressive flip angle ramping [Nagashima, 2008; Zhao *et al.*, 1996] and compared the signal results with SSFP.

The SNR-optimized FLASH sequence for hyperpolarized MRI uses a progressive flip angle schedule which monotonically ramps to a terminating value of 90° [Nagashima, 2008; Zhao *et al.*, 1996]. Transverse magnetization is crushed between repetitions to avoid signal contributions from the spin echo and stimulated echo pathways. For this sequence, the signal of the n^{th} repetition is

$$M_{y,n} = M_{z,0} E_2 \sin\theta_i \prod_{k=1}^{n-1} E_1 \cos\theta_k, \tag{3.15}$$

where the progressive flip angles are chosen iteratively

$$\theta_k = \sqrt{\frac{1 - E_1^{2N-2k-1}}{1 - E_1^{2N-2k+2}}}. \tag{3.16}$$

In the limit of long T_1, this expression simplifies to

$$\theta_k = \tan^{-1}\left(\frac{1}{\sqrt{N_{reps} - k}}\right) \tag{3.17}$$

Since the total scan time for 96 repetitions (1.4 seconds) was much smaller than the estimated *in vivo* T_1 values ($\sim$ 20 seconds), the E_1 factor was ignored for flip angle determinations. In

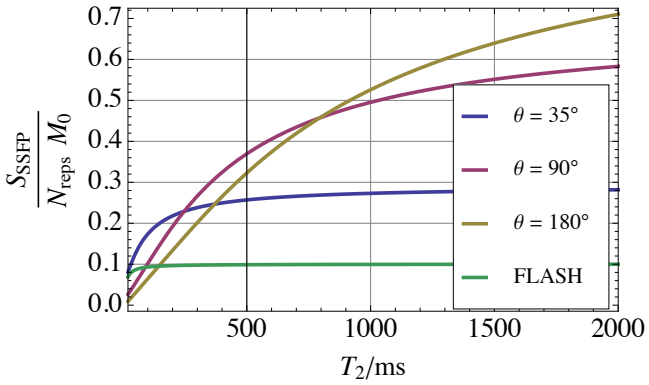

Figure 3.15: The simulated SSFP signal response plotted for various θ values as a function of T_2. For comparison, the FLASH response (equations 3.15, 3.16, and **??**) is also plotted in green. While the FLASH provides high T_2 immunity, the SSFP response yields much higher signal for all but the very low T_2 limit.

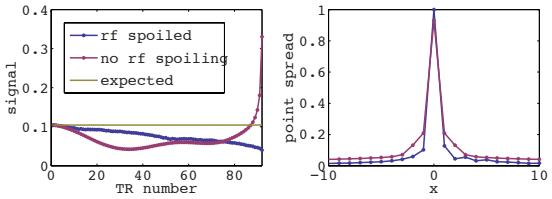

Figure 3.16: The FLASH signal response (left) and point spread (right) with and without RF spoiling using the EPG algorithm for 96 phase encodes, 15 ms TR, and progressive flip angle schedule (eq 3.17).

this case, the flip angle schedule in expression 3.17 gives the flip angle schedule giving both maximized signal and flat response [Nagashima, 2008].

Table 3.3: In Vivo FLASH / SSFP Imaging Comparisons

[^{13}C] method	[^{13}C,^{15} N$_2$] method	SNR gain	Predicted (Fig 3.1)
FLASH	SSFP (180°)	5.1 ± 2.3	6.0

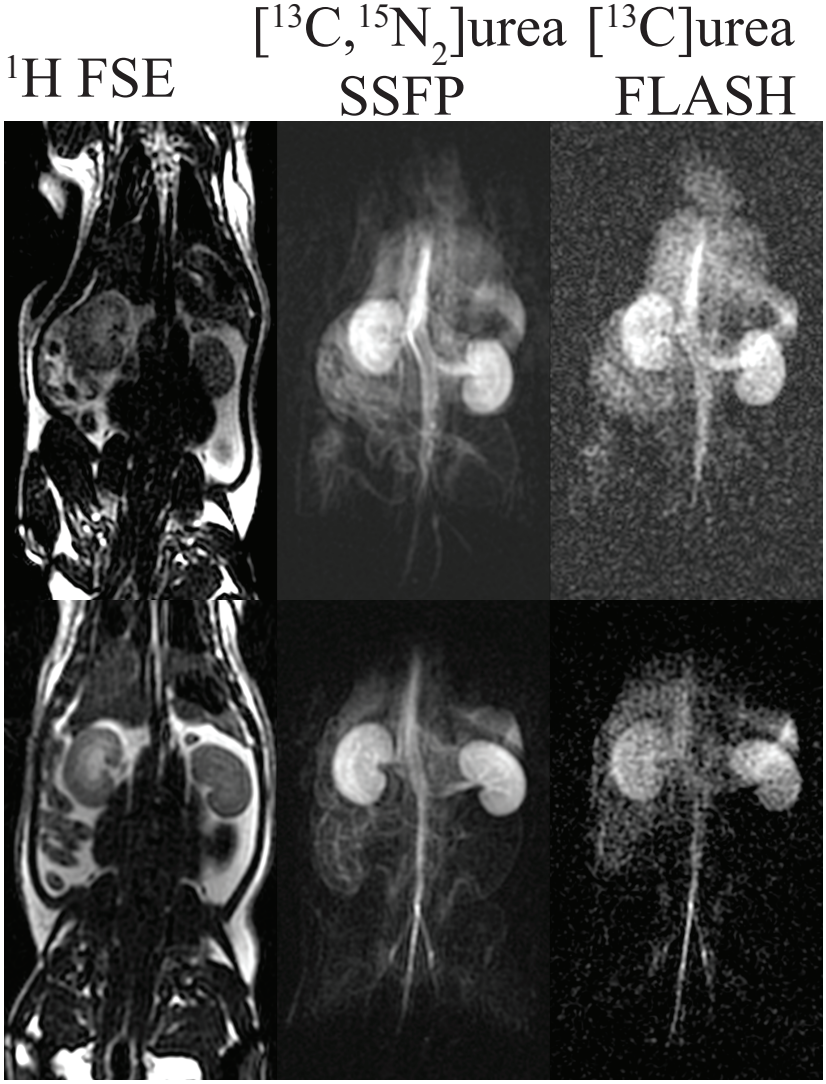

Figure 3.17: First time point $[^{13}\mathrm{C}]$ urea and $[^{13}\mathrm{C},^{15}\mathrm{N}_2]$ urea images acquired with FLASH and SSFP respectively. $[^{13}\mathrm{C},^{15}\mathrm{N}_2]$ urea images show greatly increased SNR. This SNR gain is spatially heterogeneous (high in the kidneys, low in the thoracic region) and is likely due to spatially varying T_2 values.

Chapter 4

High resolution Functional Renography using Hyperpolarized [^{13}C]Urea MRI

4.1 Abstract

This study investigated high resolution, functional renal perfusion imaging using hyperpolairzed urea as a contrast agent. Changes in ^{13}C spin-spin decoherence time (the T_2 relaxation time) of hyperpolarized urea in the rat kidney were observed following glomerular filtration, thus enabling direct differentiation of urea within the vasculature and that within renal filtrate. In one set of experiments, the vascular urea signals were highly attenuated by a chase injection of bovine serum albumin conjugated with DTPA-chelated gadolinium (BSA-GdDTPA), while the long T_2, filtered urea signal remained intact. Furthermore, T_2 mapping experiments revealed urea-specific differences between diuretic and antidiuretic states. Comparison with another hyperpolarized ^{13}C small molecule tracer showed that the T_2 changes were specific to urea and, therefore, reported on renal urea transport. The notably long T_2 relaxation times (between 4 and 15 seconds) of the filtered urea pool enabled high resolution 3D images of intra-renal urea.

4.2 Introduction

Urea is the mammalian end product of nitrogen metabolism, with the human kidneys handling on average 25 to 30 g of urea per day[Guyton, 1956]. Glomerular filtration and subsequent concentration of urea and other small molecule solutes is one of the chief functions of the kidney, and high steady state blood concentration of these solutes accompanies kidney failure. Until the past decade, the *in vivo* measurement of renal solute distribution was only possible by invasive techniques such as micro puncture catheterization [Sonnenberg and Wilson, 1981]. Meril et al demonstrated non-invasive measurement renal sodium gradients non invasively using magnetic resonance imaging (MRI) [Maril *et al.*, 2004]. Although this method requires no intravenous contrast injections, the relatively low *in vivo* ^{23}Na concentration coupled with short dominant ^{23}Na relaxation times (less than 10 ms) [Maril *et al.*, 2006] necessitate prohibitively long scan times ($>$ 15 minutes) to acquire images with modest signal-to-noise ratio (SNR).

Dynamic nuclear polarization (DNP) enhanced [Ardenkjær-Larsen *et al.*, 2003] MRI has recently emerged as a technique for the *in vivo* visualization of injected small molecule organic compounds at the mM concentration level. For the DNP process, the molecule is ^{13}C labeled at a site with a long nuclear magnetic depolarization time (T_1); this compound is then mixed with an organic radical, cooled to solid state at liquid helium temperatures and high magnetic field, and microwave irradiated at the electron / nuclear transition frequencies. In this manner, nuclear magnetic polarizations of 50% are typically observed (a gain of five orders of magnitude gain over the standard thermal polarization obtained at *in vivo* temperature and clinical MRI field strength). Remarkably, rapid dissolution of the polarized, solid state sample preserves the polarization [Ardenkjær-Larsen *et al.*, 2003], producing an injectable MRI contrast agent. This new dissolution DNP technology has enabled numerous chemical and biochemical applications, preclinical disease imaging, and is in the early stages of clinical translation

DNP-enhanced MRI of ^{13}C urea has been applied for contrast angiography using an endogenous compound [Golman *et al.*, 2003], perfusion measurements in preclinical cancer models [von Morze *et al.*, 2011a], and for functional monitoring of renal urea transport [von Morze *et al.*, 2012]. As a highly polar molecule with low lipid bilayer permeability [Finkelstein, 1976], urea is transported into the inner medullary collecting ducts via UT-A in a process critical for the production of concentrated urine [Sands, 1999].

This study demonstrates high resolution imaging of the urea filtering and concentrating function of the rat kidney using hyperpolarized ^{13}C MRI. 1-mm in-plane projection images acquired 40 s after urea injection showed significant accumulation of urea within the inner medulla and renal pelvis. Furthermore, the spin-spin relaxation time (T_2) of uniformly-labeled [^{13}C,^{15} N_2]urea [Reed *et al.*, 2014] is modulated dramatically in response to glomerular filtration, thus enabling for the first time direct non-invasive discrimination of vascular and filtered urea compartments. The long T_2 observed within the kidney can furthermore be exploited for high resolution, 3D imaging of the urea concentrating action of the kidney using a high flip angle, balanced steady state free precession (bSSFP) MRI acquisition.

4.3 Methods

4.3.1 Hardware

Imaging experiments were conducted in a GE 3T clinical MRI (GE Medical Systems, Waukesha, WI) equipped with a rat-sized dual-tuned ^{1}H / ^{13}C transceiver birdcage RF coil (8 cm inner diameter) placed on the patient table at isocenter. This scanner had a peak gradient amplitudes of 4 G/cm and peak slew rate of 15 G/cm/ms. An Oxford Instruments Hypersense polarizer (Oxford Instruments, Oxford, UK) was used for dissolution DNP experiments.

4.3.2 Sample Preparation

Isotopically enriched [^{13}C,^{15} N$_2$]urea and bis-1,1-(hydroxy- methyl)-1-^{13}C-cyclopropane-d$_8$ (abbreviated as HMCP, or HP001) were each doped with the trityl radical OX063 (Oxford Instruments, Abingdon, UK) and Dotarem (Guerbet, Roissy, France) as described previously [von Morze *et al.*, 2011a; Reed *et al.*, 2014]. The supplementary ^{15}N labeling of [^{13}C]urea was utilized for the resulting effects on low-field T_1 and high field T_2, both of which are increased and thereby contribute to improved experimental SNR [Chiavazza *et al.*, 2013; Reed *et al.*, 2014]. Bovine serum albumin (BSA) conjugated with 25 gadolinium / diethylene triamine pentaacetic acid (GdDTPA) chelates per BSA molecule was synthesized in house (molecular weight $\sim$ 85 kDa) using methods described previously [Dafni *et al.*, 2002].

4.3.3 Animal handling

Animal studies were performed under a protocol approved by the UCSF Institutional Animal Care and Utilization Committee (IACUC). In all experiments, Sprague Dawley rats (Charles River Laboratories, Wilmington, MA) were anesthetized with a 2% isofluorane / oxygen mixture under a constant flow rate of 1 liter per minute. Animals were imaged in the supine position inside the birdcage coil and thermally insulated via heat pad. Contrast agents were injected via lateral tail vain catheters.

4.3.4 T_2 mapping and multi-exponential analysis

Effective *in vivo* T_2 mapping was performed using the multiple echo 180° bSSFP imaging sequence beginning with a single 90° catalyzation (excitation) pulse [Reed *et al.*, 2014]. Flip angle calibration was performed by finding transmitter power required produce a signal null of a 1 mL, 8M ^{13}C syringe place on the surface of the animal. Dynamic projection images were acquired in the coronal plane with 1 mm in-plane resolution, 14×7 cm FOV, 13 ms TR, giving a temporal resolution of 910 ms and 18.2 s total acquisition time for all 20 echoes. All

pixels with an-SNR greater than 10 at the first time point were included in the analysis. For multi exponential T_2 decay analysis, the T_2 non-negative least squares (T_2NNLS) algorithm [Whittall and MacKay, 1989] with an L_1-norm regularization penalty for noise-stabilization was applied. Curve fitting was performed by seeking non-negative solutions for s_i, the vector of T_2 component amplitudes that minimize

$$||As - y||^2 + \lambda \sum_i x_i, \tag{4.1}$$

with

$$A_{i,j} = e^{-t_j/T_{2,i}}. \tag{4.2}$$

$T_{2,i}$ is an array of 64 logarithmically-spaced T_2 values ranging from .3 to 20 s, t_j are the echo times (20 regularly spaced from 0.5 to 19 s) , and y_j is the detected pixel SNR values of the jth echo. Fitting scripts used the interior point l1-ls solver [Kim *et al.*, 2007] written in Matlab (The Mathworks, Natick, MA). The regularization parameter λ was chosen to be 1% of λ_{max}, with $\lambda_{max} \equiv ||A^T y||_\infty$ determined at each pixel [Kim *et al.*, 2007]. The logarithmic mean T_2, denoted $\langle T_2 \rangle$, was calculated from the first moment of the T_2 pseudo spectra:

$$\langle T_2 \rangle_{\alpha,\beta} = \exp\left\{ \frac{\int_\alpha^\beta s(T_2) \log T_2 \, dT_2}{\int_\alpha^\beta s(T_2) \, dT_2} \right\}. \tag{4.3}$$

The integration limits α and β were set based on the experiment. In addition to the $\langle T_2 \rangle$ within the α and β limits, the SNR corresponding to this T_2 range was also calculated by integrating $s(T_2)$ from α to β.

The χ^2 goodness-of-fit metric was calculated for each fit [Whittall and MacKay, 1989], and data were included in analysis with $\chi^2/N_{echo} > 0.8$, $\chi^2/N_{echo} < 1.2$, where N_{echo} is the number of echo times. Pixel distributions of $\langle T_2 \rangle$ were characterized using the generalized extreme value (GEV) distribution [Reed *et al.*, 2014] to determine the mean, variance, and

shape parameter k, the latter which quantifies the assymmetry of the distribution.

4.3.5 ^{13}C urea / albumin-Gd relaxometry experiments

The ^{13}C T_1 relaxivity of [^{13}C,^{15}N$_2$]urea with respect to concentration of the high molecular weight (85 kDa) paramagnetic complex BSA-GdDTPA (a complex of bovine serum with gadolinium and chelating agent diethylenetriaminepentacetate) was measured in a 1 mL vial containing 1 M [^{13}C,^{15}N$_2$]urea via saturation recovery experiments at $B_0 = 3$ T, $T = 27°$C.

A variation of the hyperpolarized ^{13}C experiment [Smith *et al.*, 2012] was performed by following the hyperpolarized infusion with a chase bolus of the intravascular relaxation agent in order to depolarize the vascular urea compartment. The chaser used here was a vascular gadolinium agent. Rats ($n = 4$) were injected with 3 mL, 150 mM hyperpolarized [^{13}C,^{15}N$_2$]urea solution over 12 s. The hyperpolarized urea was then allowed to diffuse for 28 s, and the ^{13}C T_2 mapping sequence (see section 4.3.4) was initiated 40 s after the beginning of injection. Two hours later, a second [^{13}C,^{15}N$_2$]urea infusion was performed over 12 s. The hyperbolarized urea was then allowed to diffuse for 20 s, then 1 mL, 0.59 mM BSA-GdDTPA (15 mM GdDTPA) was injected over 1 s. The chase bolus was allowed to diffuse for 7 s, and then the ^{13}C T_2 mapping sequence was initiated again 40 s after the beginning of the urea injection. For 2 rats, ^{1}H-detected, T_1-weighted spoiled gradient echo (SPGR) images (flip angle = 35, $TE/TR = 1.4/7$ ms, 3 averages, .8 mm isotropic resolution) were acquired 5 minutes post infusion of BSA-GdDTPA to ensure that no glomerular filtration or renal perfusion occurred. This was followed by an additional injection of 1 mL, 0.5 mM low molecular weight (940 Da) Gd-DTPA without attached albumin (Magnevist, Bayer Schering, Berlin). A repeat ^{1}H SPGR sequence was used to image this agent 5 minutes after infusion.

The ^{13}C images were analyzed via the multi exponential analysis described in section 4.3.4. The short T_2 signal was defined by the cutoff values $\alpha = 0.3$ s, $\beta = 2.5$ s, and the long T_2 signal used $\alpha = 2.5$ s, $\beta = 20$ s. These values were chosen based on the observation that the

in vivo [^{13}C,^{15}N$_2$]urea T_2 has a bimodal distribution with one peak centered approximately at 1.3 s, and the other greater than 4 s [Reed *et al.*, 2014].

4.3.6 Diuresis / antidiuresis relaxometry experiments

Rats ($n = 3$) were imaged on both diuresis and antidiuresis protocols. For the antidiuresis protocol, the rats were deprived of food and water for an overnight period of 16 hours. For the diuresis protocol, the rats were first deprived of food and water for 16 hours and then allowed free access to aqueous glucose (10% by mass) solution for 9 hours. This protocol has been shown to induce diuresis and produce large increases in urine production [von Morze *et al.*, 2012].

In each experiment, the rat received 2 injections. The first was 3 mL, 150 mM hyperpolarized [^{13}C,^{15}N$_2$]urea solution. The second was 3 mL, 125 mM hyperpolarized HMCP solution performed at least 2 hours after the urea injection. In each hyperpolarized experiment, the T_2 mapping sequence was initiated 40 s after the beginning of injection with identical acquisition parameters.

All images were analyzed by applying the T_2NNLS algorithm. Due to the severe noise amplification observed with isolating similar T_2 signal components of HMCP, α and β were chosen to be the full sampled T_2 domain (.3 s to 20 s), and the net $\langle T_2 \rangle$ over this whole domain was reported for both compounds.

4.3.7 3D urea renography

A specialized high flip angle 3D SSFP pulse sequence was developed similar to prior projection SSFP implementations [Svensson *et al.*, 2003; Reed *et al.*, 2014] but with the addition of a second phase-encoded dimension. The MRI scan used a $(42, 42, 14)$ acquisition matrix over a $(5, 5, 1.7)$ cm FOV in (L-R,S-I,A-P) coordinates yielding a 1.2 mm isotropic pixel size. A total of 588 phase encodes were acquired in a 2D Cartesian raster with $TR = 12$ ms for a

7 s total scan time (3.5 s effective echo time). Frequency encoding was set along the superior/inferior dimension, fast phase encoding along the left/right dimension, and slow phase encoding along anterior / posterior. No slice select gradient pulses were used, and, therefore, the images were sampled below the Nyquist cutoff frequency in both phase-encoded dimensions. Since the sequence used this extremely long effective echo time, the large T_2 difference between vascular and renal urea results in suppression of the vascular signal and a FOV over which phase encoding was necessary. The sequence's relative SNR as a function of flip angle θ and total number of phase encoding steps was simulated for 3 different T_2 values representative of those measured for [^{13}C,^{15} N$_2$]urea in the manuscript (see 4.7.1 for details of this calculation). T_1 weighing was ignored in simulations. One rat was imaged starting at 20 s, 25 s, and 30 s after the beginning of a 12 s injection of 3 mL, 120 mM hyperpolarized [^{13}C,^{15} N$_2$]urea to demonstrate the feasibility of a full 3D acquisition. All images were aligned using OsiriX [Rosset *et al.*, 2004].

4.4 Results

4.4.1 ^{13}C urea / albumin-Gd relaxometry experiments

The T_1 ^{13}C urea relaxivity of the BSA-GdDTPA on [^{13}C,^{15} N$_2$]urea was measured to be 77 ± 10 mM^{-1}s^{-1}, or $3.1 \pm .4$ mM^{-1}s^{-1} per GdDTPA chelate ($R^2 = .97$). Given the net administered dose of 50 mg BSA-GdDTPA, the urea ^{13}C T_1 was 0.55 s for the estimated rat blood volumes of 25 mL [Lee and Blaufox, 1985] assuming uniform the intravascular urea and BSA-GdDTPA were both uniformly mixed. See Figure 4.1 for the T_1 relativity curve.

^{13}C urea images acquired at the first time point, with and without the BSA-GdDTPA chaser are shown in Figure 4.2a and 4.2b, respectively. The background, vascular ^{13}C urea signal was strongly attenuated by the BSA-GdDTPA. Within the kidney, aside from some attenuation observed in the interlobular arteries, the ^{13}C urea signal remained constant.

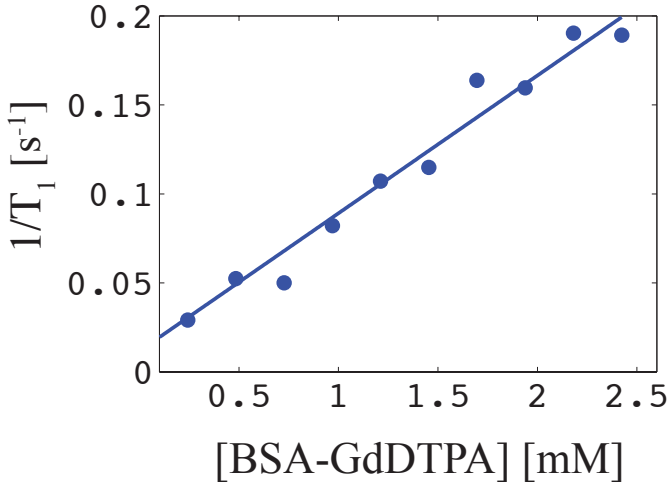

Figure 4.1: Measured ^{13}C urea / BSA-GdDTPA relaxivity curve. The T_1 of the intravascular ^{13}C urea was less than one second assuming uniform ^{13}C urea / BSA-GdDTPA mixing within the vascular compartment. (potential supplementary info plot)

The maximum intensity projection ^{1}H SPGR image acquired 5 minutes after BSA-GdDTPA administration is shown in Figure 4.2c. Distribution through the renal and interlobular arteries is evident, but the high molecular weight prohibits glomerular filtration, and no intra renal signal is detected. The ^{1}H image acquired 5 minutes post-injection of GdDTPA, however, shows renal perfusion and collection in the urinary bladder.

^{13}C images at the first (TE = 0.5 s) and sixth (TE = 6.0 s) echoes are shown in Figure 4.4a. Early echoes show attenuation of the vascular ^{13}C signal after BSA-GdDTPA administration. At later echo times, the images are nearly identical. T_2 maps generated via multi exponential decomposition are shown in Figure 4.4b. Signal with $T_2 > 2.5$ s was essential unaffected by the BSA-GdDTPA chaser, whereas the vascular, short-T_2 signal was strongly attenuated. The mean $\pm$ standard deviation number of pixels per animal with first-echo $SNR > 10$ decreased following the Gd-BSADTPA injection from 2990 ± 1077 (mean $\pm$ s.d.) to 1380 ± 1015. Distributions of pixel SNR as well as the mean SNR of the short and

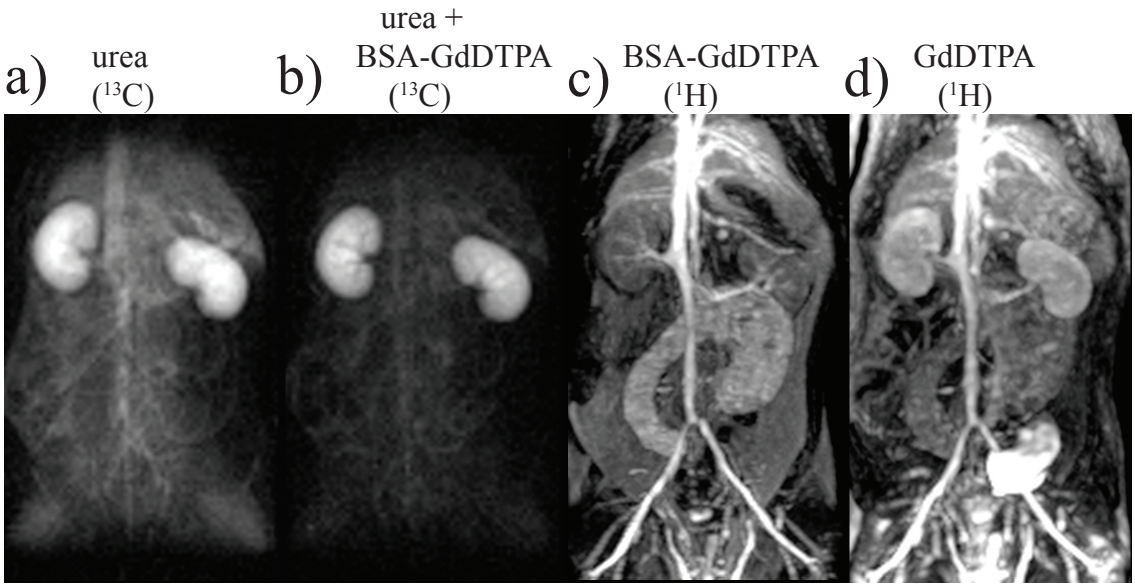

Figure 4.2: a) Coronal projection ^{13}C image of hyperpolarized $[^{13}\mathrm{C},^{15}\mathrm{N}_2]$urea at the first time point (40 seconds after urea injection). b) first time point $[^{13}\mathrm{C},^{15}\mathrm{N}_2]$urea image also acquired 40 seconds after urea injection, and 8 seconds post injection of the BSA-GdDTPA vascular relaxation agent. The Gd agent relaxes the vascular signal strongly but leaves the renal signal intact. c) ^{1}H maximum intensity angiogram (maximum intensity projection) acquired 5 minutes after BSA-GdDTPA infusion shows that no BSA-GdDTPA perfused into the kidneys. Furthermore, the interlobular arteries, which were attenuated in the post-BSA-GdDTPA image attenuated in the post-BSA-GdDTPA image (b), are bright in image (c). d) ^{1}H MR angiogram acquired 5 minutes after infusion of GdDTPA; the lower molecular weight allows glomerular filtration, renal perfusion, and bladder collection.

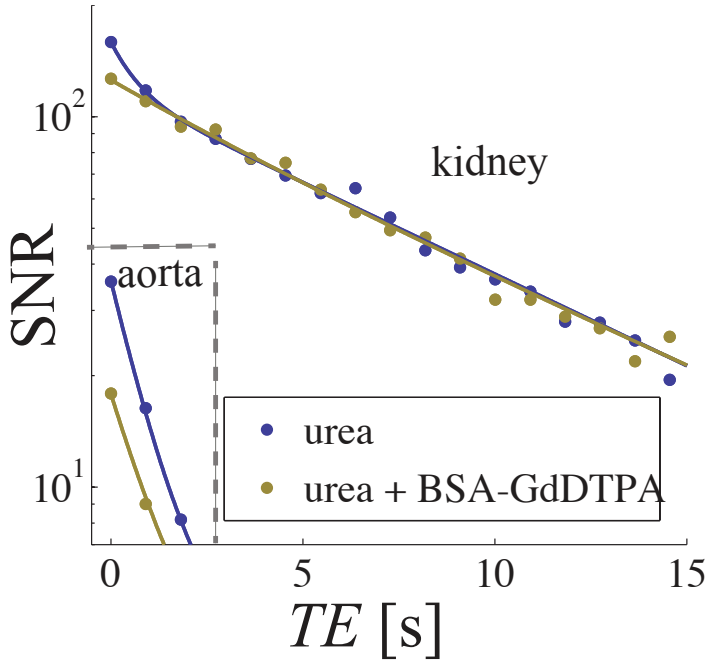

Figure 4.3: Single pixel T_2 decay curves of [^{13}C,^{15} N$_2$]urea in the aorta and kidney with and without the BSA-GdDTPA chaser. The T_2NNLS fits with are also displayed (solid lines). (potential supplementary info plot)

long T_2 components are shown in Figure 4.5. The mean SNR of the short T_2 component was 12.4 ± 2.2 with and 19.6 ± 4.3 without the BSA-GdDTPA chaser, respectively (Figure 4.5b). The paired t-test showed this difference to be statistically significant ($p = .027$). The mean SNR of the long T_2 component was 48 ± 5 and 48 ± 2 without the BSA-GdDTPA chaser, respectively. *In vivo* single pixel ^{13}C urea T_2 decay curves are shown in Figure 4.3.

BSA-GdDTPA caused a small shortening of the apparent vascular T_2 from $1.39 \pm .29$ s to $1.19 \pm .32$ s. The long T_2 component was 5.28 ± 1.58 s and 5.28 ± 2.27 s with and without the BSA-GdDTPA chaser, respectively. Figure 4.4c shows an example of the short and long T_2 maps.

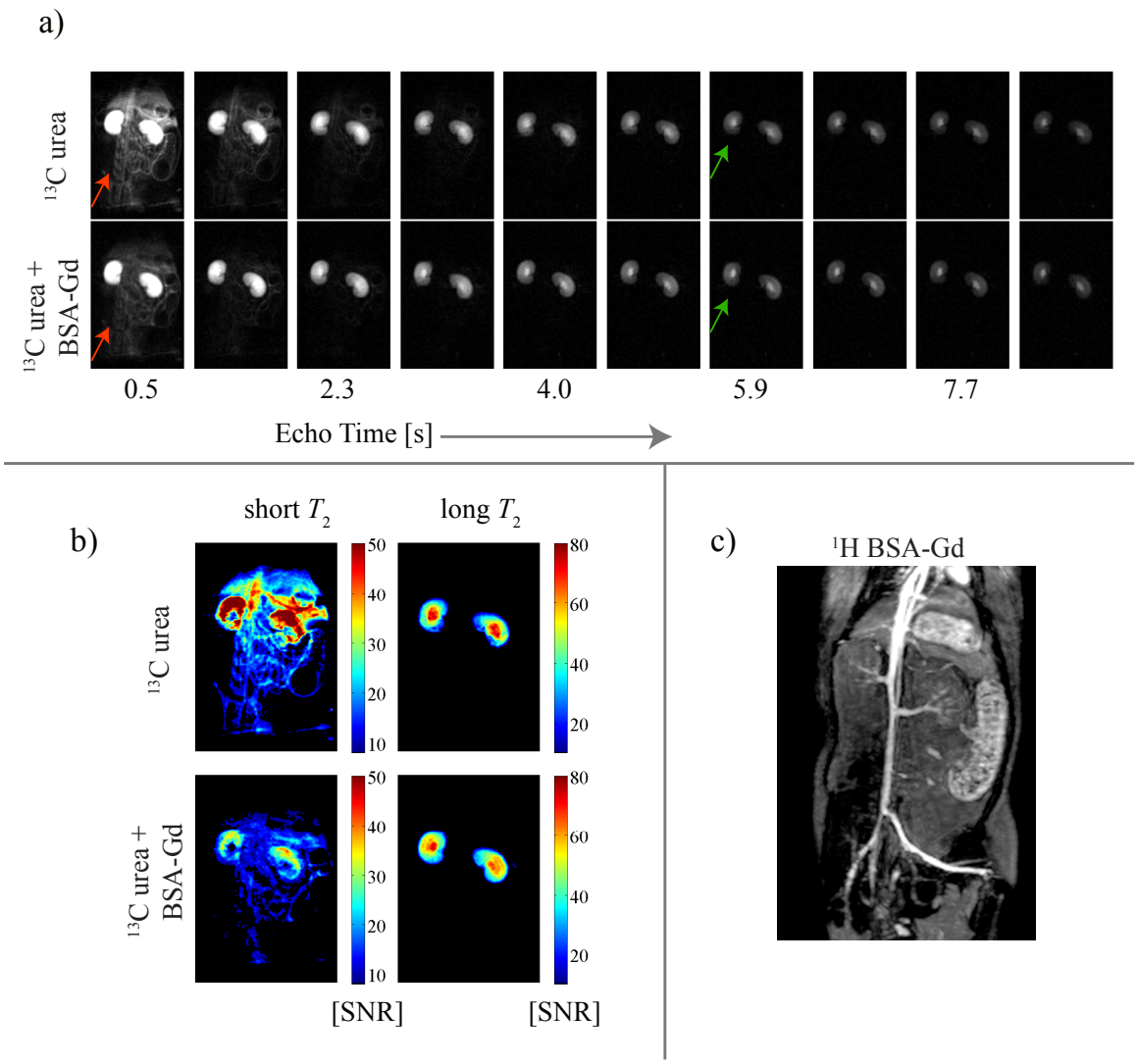

Figure 4.4:
a) coronal projection ^{13}C MRI image of hyperpolarized $[^{13}\mathrm{C},^{15}\mathrm{N}_2]$urea acquired with (top row) and without (bottom row) BSA-GdDTPA injections at early (left) and late (right) echo times. The BSA-GdDTPA agent strongly attenuates the vascular signal in the early echoes (red arrows), but at later echoes the images looks similar (green arrows, images are displayed with identical scaling). b) amplitudes of the short and long T_2 components (in units of SNR). c) coronal ^{1}H angiogram (maximum intensity projection) acquired 5 minutes post BSA-GdDTPA injection.

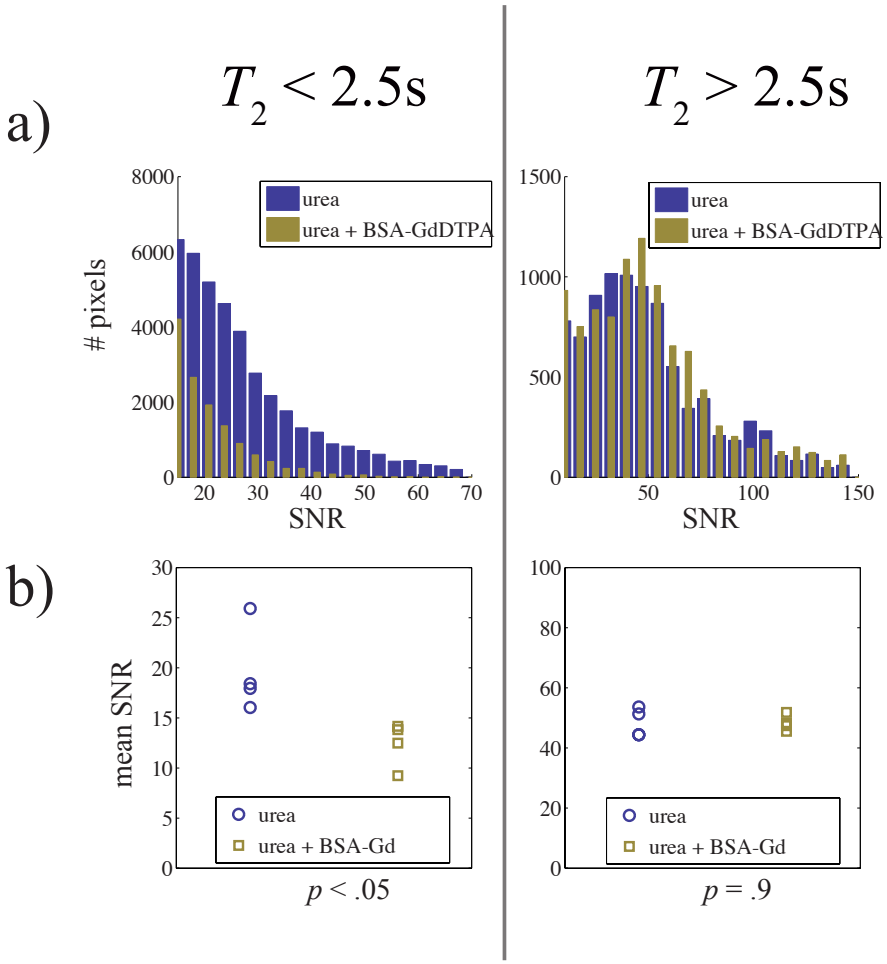

Figure 4.5:
a) image histogram showing short-T_2 (left) and long-T_2 (right) SNR distributions of all ^{13}C urea pixels with $SNR > 10$ at the first echo, grouped over all 4 rats with (gold) and without (blue) BSA-GdDTPA chaser. Bottom: mean values of these components for each rat.

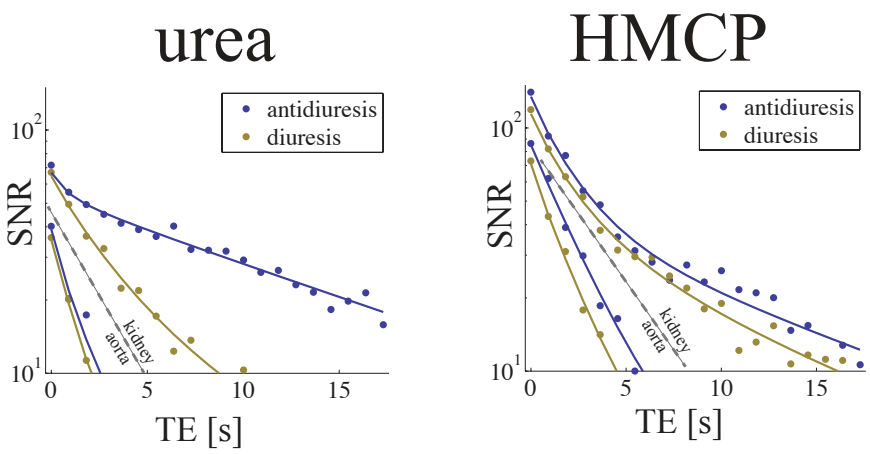

Figure 4.6: Single pixel decay curves of urea (left) and HMCP (right) plotted along with the T_2NNLS fits (solid lines). Both compounds showed long T_2 component within the kidney. (potential supplementary info plot)

4.4.2 Diuresis / antidiuresis relaxometry experiments

The late echo [^{13}C,^{15} N$_2$]urea images depicted in Figure 4.7 highlight the faster inner-medullary urea concentration induced under antidiuresis, consistent with prior findings [von Morze *et al.*, 2012]. The extra-renal signal exhibited diffuse, short $\langle T_2 \rangle$ signal for both compounds (Figure 4.7, right). This $\langle T_2 \rangle$ was uniformly higher for HMCP (3.33 ± 1.02) than for urea ($2.45 \pm .32$ s).

Both compounds showed some increase in $\langle T_2 \rangle$ within the kidney. The pixel distributions of the intra renal $\langle T_2 \rangle$ values are shown in Figure 4.8a. HMCP had a mean $\langle T_2 \rangle$ within the kidney of $3.03 \pm .40$ s and $3.16 \pm .52$ s under antidiuresis and diuresis, respectively.

Urea specifically showed greatly differing $\langle T_2 \rangle$ distributions within the kidney between states. Although the mean values of $\langle T_2 \rangle$ were similar between antidiuresis (4.08 ± 2.53) and diuresis (4.08 ± 0.40), the distributions had different asymmetries ($k = .24 \pm .02$ and $-0.33 \pm .01$, respectively). Figure 4.8a, left shows these changes. The high $\langle T_2 \rangle$ observed in antidiuresis was focused on the inner medulla and renal pelvis (Figure 4.7, top right).

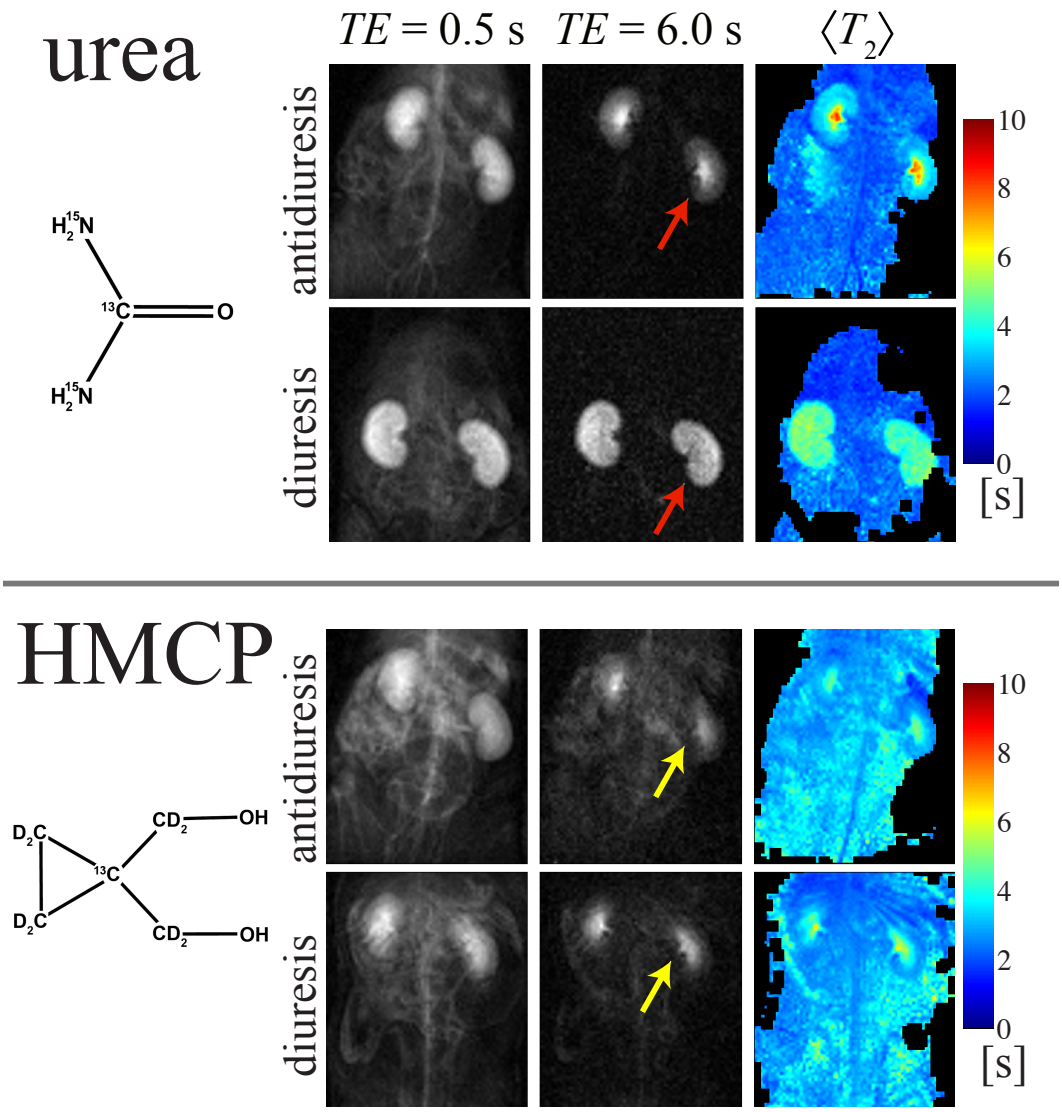

Figure 4.7: Early (left) and late (center) echo coronal projection ^{13}C images of [^{13}C,^{15}N$_2$]urea and [^{13}C]HMCP in rats with induced diuresis and antidiuresis. $\langle T_2 \rangle$ maps are shown in the right column. The effects of diuresis and antidiuresis on urea images are most evident at later echo times (red arrows) after the short T_2 vascular signal had disappeared. HMCP shows similar late-echo renal concentration independent of physiologic state (yellow arrows). $\langle T_2 \rangle$ mapping provided a quantification of this effect, and clearly resolved the cortical, medullary, and pelvic regions of the kidney in antidiuresis urea images (top right).

In order to select for the regions of the inner medulla and renal pelvis regions, the mean of the top 90th percentile of $\langle T_2 \rangle$ within the kidney (denoted $\langle T_2 \rangle_{90}$) was computed for each compound in each animal within the kidney. Figure 4.8b shows the mean $\langle T_2 \rangle_{90}$ for each animal. The mean urea $\langle T_2 \rangle_{90}$ was $7.40 \pm .80$ s for the antidiuresis rats and $4.80 \pm .39$ s for the diuresis rats. A paired t-test showed the urea changes between diuretic states to be significant ($p < .01$). The mean HMCP $\langle T_2 \rangle_{90}$ was $4.62 \pm .18$ s for the antidiuresis rats and $4.33 \pm .63$ s for the diuresis rats. The insensitivity of HMCP to diuretic state can be seen on the $\langle T_2 \rangle$ maps in Figure 4.7, right.

4.4.3 3D urea renography

The SSFP signal behavior as a function of resolution and flip angle is shown in Figure 4.9. With the sequence parameters used, the relative signal response of urea in the blood, medulla, and renal pelvis is .28, .60, and .78. respectively. Full 3D images sets acquired acquired at after 3 different delay times are shown in Figure 4.10. At 20 s and 25 s delay periods, cortical and outer medullary urea signals are dominant ($SNR = 25$). At the 25 s delay, the outer stripe of the outer medulla can be resolved in both coronal and axial images. Signal from the aorta and vena cava are detectable as well with $SNR = 25$. No significant blurring was observed in the major vessels. The 30 s time point image shows urea collection in the inner medulla and renal pelvis, with SNR of 35 and 65 in these regions, respectively.

4.5 Discussion

The strong attenuation of the short T_2 ^{13}C urea signal and the corresponding preservation of the long T_2 signal following the BSA-GdDTPA chase injection strongly support the hypothesis that the long T_2 component reports directly on glomerular filtration. The large T_2 differences between vascular and filtered urea demonstrate that hyperpolarized ^{13}C urea

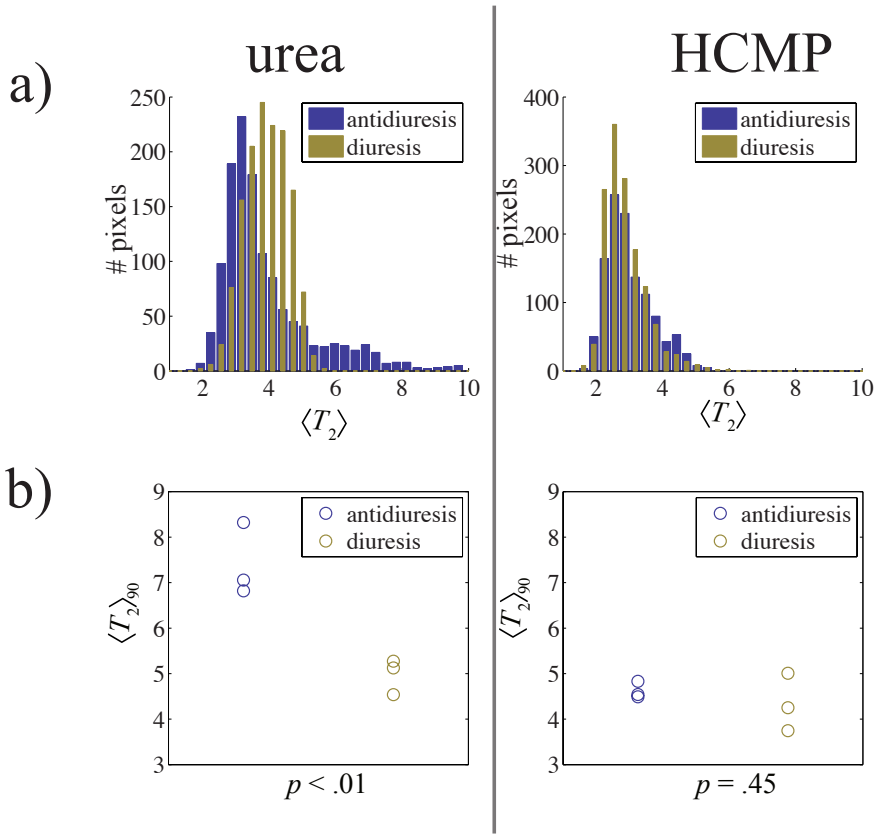

Figure 4.8: a) $\langle T_2 \rangle$ distributions for all kidney pixels in all animals. The differing urea distribution $\langle T_2 \rangle$ shapes (left) between diuresis and antidiuresis are quantified in the shape parameter k, which was $.24 \pm .02$ and $-0.33 \pm .01$, respectively. The HMCP $\langle T_2 \rangle_{90}$ gave shape parameters of k of $.026 \pm .024$ and $.050 \pm .018$ for antidiuresis and diuresis rats, respectively. b) the mean of the upper 90th percentile of $\langle T_2 \rangle$ values in the kidney. Higher $\langle T_2 \rangle_{90}$ noted with urea in the antidiuresis state signifies faster urea collection to the inner medulla and renal pelvis.

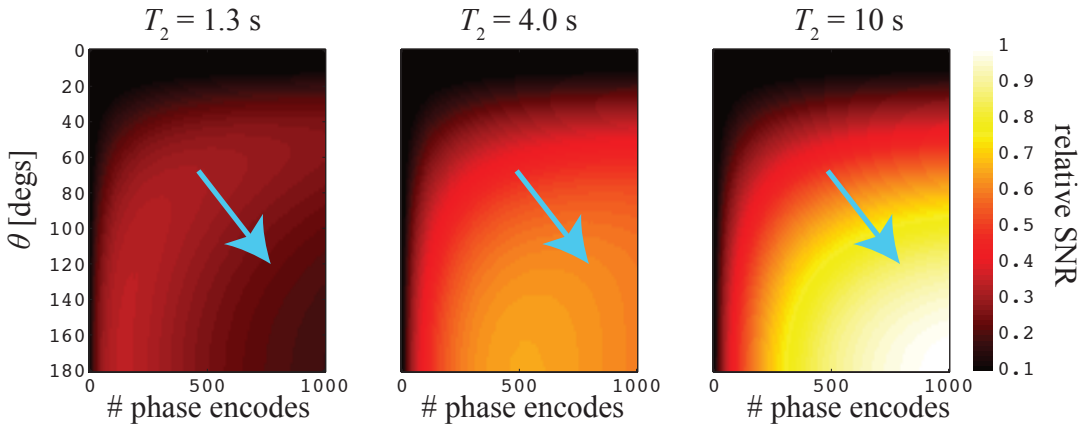

Figure 4.9: Simulated urea SNR as a function of flip angle θ and number of phase encodes plotted for $T_2 = 1.3$ s (the vascular pool), $T_2 = 4$ s (urea within the cortical and medullary tubules), and $T_2 = 10$ s (urea within the collecting system).

MRI can directly differentiate these two pools and thereby directly monitor the process of glomerular filtration in vivo in a highly localized manner, thus representing a unique and potentially powerful new capability, especially considering the exceptional safety profile of urea as a potential contrast agent [Johnson *et al.*, 1972].

The observed T_2 differences are likely due to urea's high erythrocyte membrane permeability [Potts *et al.*, 1992] which creates a strong T_2 shortening from intracellular paramagnetic hemoglobin. A recent study noted greatly reduced intracellular T_1 values of urea [Páges *et al.*, 2013]. Although direct measurements in whole blood report T_2 values in the range of 4 to 5 s [Reed *et al.*, 2014], these values differ by a factor > 2 from *in vivo* measurements. As in ^{1}H MRI, within the liquid compartments, T_2 approaches the same value as T_1. For carbonyl ^{13}C spins, this value is exceptionally long, and T_2 values in excess of 20 s are observed for most hyperpolarized ^{13}C probes in aqueous solution [Reed *et al.*, 2014; Svensson *et al.*, 2003; Grant *et al.*, 2011]. Flow attenuation from imaging gradients is possible, but non-localized *in vivo* CPMG T_2 measurements of urea acquired 10 s post injection still gave T_2 values

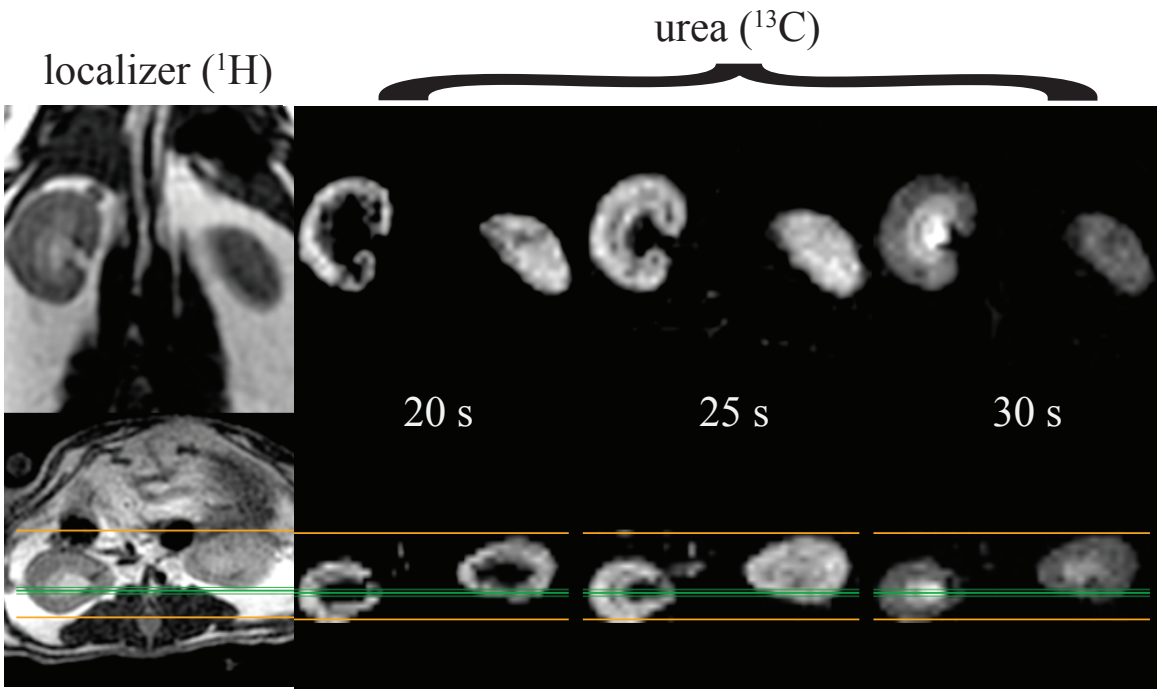

Figure 4.10: Full 3D images (1.2 mm^3 isotropic resolution) of hyperpolarized [^{13}C,^{15}N$_2$]urea in multi-planar format (top row = coronal, bottom row = axial) at delay times of 20 - 30 s after the beginning of injection. Late time point images (right) show the concentration to the inner medullary collecting ducts; hyper intensity of this region is due to the long T_2 and strong T_2 weighting. The yellow margins indicate the phase-encoded FOV in the slow phase encoded dimension. The green line indicates slice position of the displayed coronal images.

less than 2 s even in the absence of applied B_0 gradients (see supplementary info). This possibly indicates differing rotational correlation times of blood urea in *ex vivo* and *in vivo* conditions, or intrinsic diffusion weighting induced due to flow through infomogeneous B_0 fields *in vivo*.

Despite the fact that the urea T_1 should have been much less that 1 s if the BSA-GdDTPA was completely diffused though out the blood pool, significant vascular SNR was still observed after the chaser, which was allowed to diffuse 7 s before imaging. This could suggest partial extravasation of the injected urea within voxels that been assumed to be strictly vascular, or that the chaser had not fully diffused by the first time point. However, late echo ^{13}C images were acquired more than 20 s after chaser infusion, and these showed no detectable SNR attenuation.

The use of $\langle T_2 \rangle$ for quantification provide an indirect measurement of contrast agent localization in the diuresis experiments since it is a weighted average of all T_2 components. As seen in Figure 4.4c, the long T_2 component of urea shows a large increase from the cortex / outer medulla to the inner medulla and renal pelvis. Therefore, antidiuresis changes observed weighted the $\langle T_2 \rangle$ measurements more strongly to the long T_2 pools, thus increasing the net $\langle T_2 \rangle$ values. The measured HMCP insensitivity of $\langle T_2 \rangle$ to diuresis and antidiuresis could potentially arise from the higher vascular signal due to the longer T_1 of this agent and the relatively long injection-to-imaging delay times, thereby concealing any renal T_2 changes. However, the later echo HMCP images reveal similar signal distribution in the kidney independent of physiological state.

Despite the fact that the intra renal HMCP pixels showed clear multi exponential behavior (Figure 4.6), resolution of HMCP into short and long T_2 components showed large noise amplification, likely do to the similarity of the T_2 values of this compound. Urinary bladder collection was observed using HCMP at 2 to 3 minutes post injection. Ureter flow was also observed in one diuresis T_2 mapping experiment (see supplementary materials for images). No ureter or urinary bladder collection of urea was observed, likely due to the

shorter aqueous T_1 of this compound.

T_2 measurements *in vivo* must be considered effective T_2 measurements since flow attenuation from the imaging gradients, diffusion, and flip angle errors all cause deviations in the signal decay. In 4.7.2, the effect of transmitter miscalibration on the measured T_2 is quantified, and is shown to depend only to second order on flip angle error. The relatively coarse (910 ms) temporal sampling of the signal will lead to errors in detecting T_2 values below the sampling rate. Non-selective CPMG measurements acquired *in vivo* with 10 ms sampling rate show a short, 300 ms decay component of [^{13}C,^{15} N$_2$]urea which consists of $\sim 30\%$ of the signal.

The use of urea as a medical imaging contrast agent is intriguing due to its well known low toxicity. Planar scintigraphy using chelated ^{99m}Tc and contrast-enhanced MRI using chelated Gd - the current gold standards for radiographic renal function evaluation -use either ionizing radiation or potentially nephrotoxic compounds. ^{13}C MRI requires no ionizing radiation, and its lack of toxicity has been shown even in patients with end stage renal failure [Johnson *et al.*, 1972].

4.6 Conclusion

This study demonstrated functional renography using hyperpolarized ^{13}C urea. [^{13}C,^{15} N$_2$]urea undergoes a large T_2 shift with glomerular filtration enabling for the first time direct separation of the vascular and filtered components. The urea signal within the kidney showed high T_2 sensitivity to diuresis and antidiuresis states. Finally, a method for encoding high resolution 3D renographic images by exploiting the long T_2s of the urea within the renal tubules was presented.

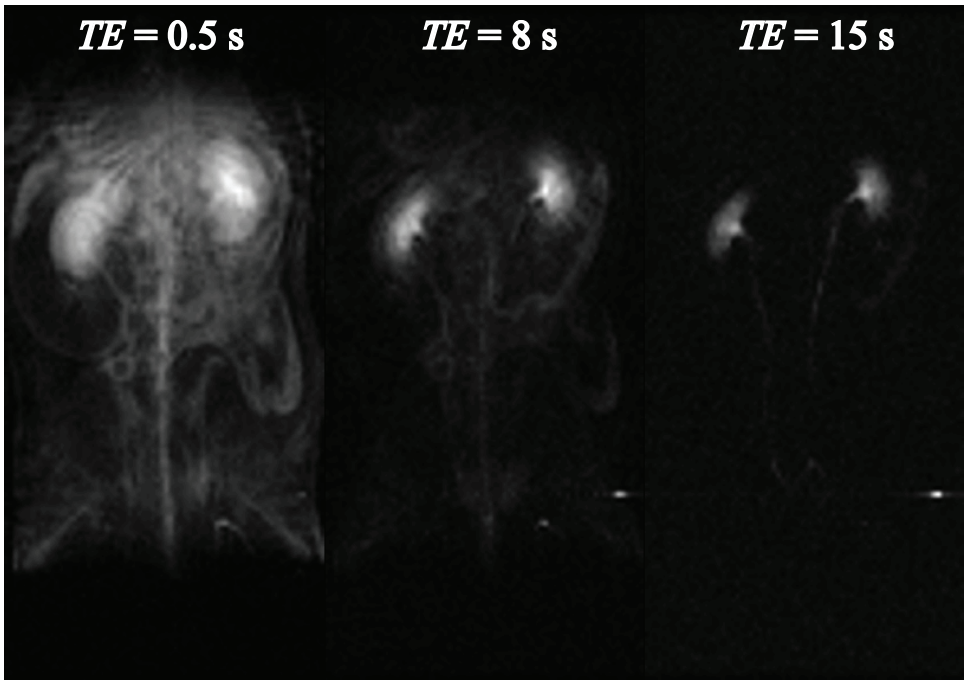

Figure 4.11:
^{13}C HMCP imaging of ureter flow during diuresis.

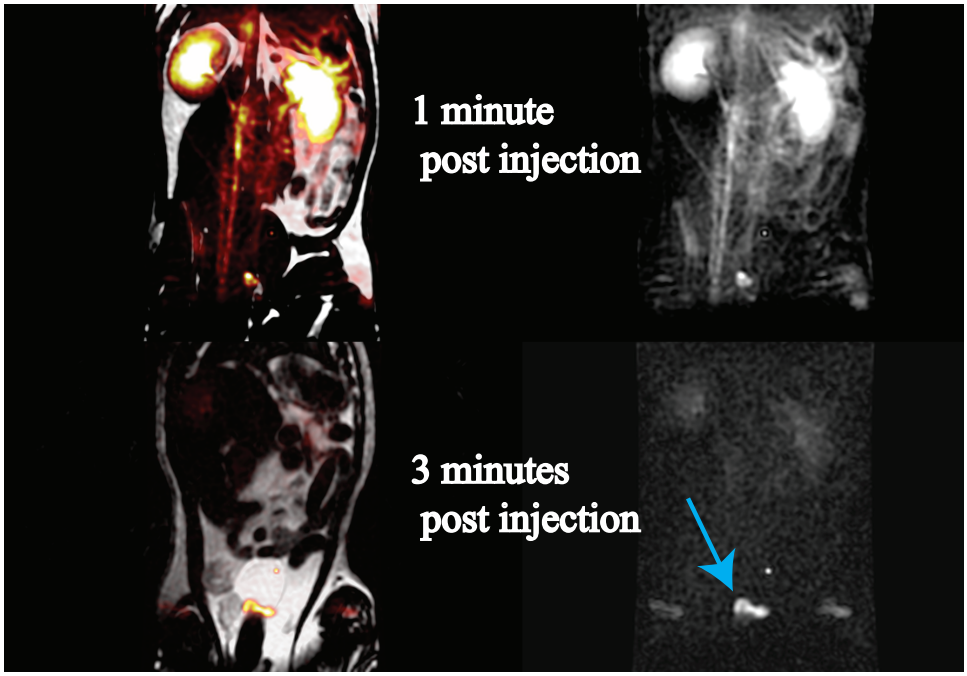

Figure 4.12:
^{13}C HMCP collection in the urinary bladder 3 minutes post injection (blue arrow). The ghost images $1/4$ FOV off-center are steady state-artifacts occurring from transient oscillations during phase encoding.

4.7 Appendix

4.7.1 SSFP SNR simulations

The SSFP SNR as a function of θ and N was simulated using previously derived signal models [Svensson *et al.*, 2003] and assuming normally-distributed noise which scales as $\sqrt{N}$, where N is the number of phase encoding steps:

$$SNR = \frac{1}{\sqrt{N}} \sum_{n=1}^{N} \sin\frac{\theta}{2} \left[\left(E_1 \cos\frac{\theta}{2} \right)^2 + \left(E_2 \sin\frac{\theta}{2} \right)^2 \right]^{n/2}, \tag{4.4}$$

4.7.2 T_2 measurement errors from transmitter offsets

Ignoring flow and off-resonance, the flip angle θ mixes the T_1 and T_2 weighting so that the net SSFP signal decay time T is [Grant *et al.*, 2011] [Scheffler, 2003]

$$\frac{1}{T} = \frac{1}{T_1} \cos^2\left(\frac{\theta}{2}\right) + \frac{1}{T_2} \sin^2\left(\frac{\theta}{2}\right) \tag{4.5}$$

All T_2 mapping measurements in this study assume $\theta = \pi$, for which the decay time $T = T_2$. Assuming the true flip angle is $\pi + \delta\theta$, expanding $1/T$ gives

$$\frac{1}{T} = \frac{1}{T_2} + \left(\frac{1}{4T_1} - \frac{1}{4T_2} \right) \delta\theta^2 + O\left(\delta\theta^4\right) \tag{4.6}$$

Non-ideal π pulses will cause some apparent lengthening of the measured T_2 and will introduce some T_1 weighting. However, these errors show up only as second order or higher terms of $\delta\theta$. Assuming $T_2 = 1.5$ s, $T_1 = 20$ s, flip angle errors $\delta\theta/\theta$ up to 20% cause T to differ from T_2 by less than 10%.

Chapter 5

A Method for Simultaneous Echo Planar Imaging of Hyperpolarized ^{13}C Pyruvate and ^{13}C Lactate

5.1 Abstract

A rapid echo planar imaging sequence for dynamic imaging of [1-^{13}C] lactate and [1-^{13}C] pyruvate simultaneously was developed. Frequency-based separation of these metabolites was achieved by spatial shifting in the phase-encoded direction with the appropriate choice of echo spacing. Suppression of the pyruvate-hydrate and alanine resonances is achieved through an optimized spectral-spatial RF waveform. Signal sampling efficiency as a function of pyruvate and lactate excitation angle was simulated using two site exchange models. Dynamic imaging is demonstrated in a transgenic mouse model, and phantom validations of the RF pulse frequency selectivity were performed.

5.2 Introduction

Recent studies have shown the great potential of hyperpolarized ^{13}C pyruvate for the in vivo monitoring of cellular metabolism and the characterization of disease [Kurhanewicz *et al.*, 2011; Golman *et al.*, 2003; Golman *et al.*, 2006b; Golman *et al.*, 2006a; Park *et al.*, 2010; Chen *et al.*, 2007; Albers *et al.*, 2008; Merritt *et al.*, 2007; Kettunen *et al.*, 2010; Schroeder *et al.*, 2008; Brindle *et al.*, 2011]. Dynamic nuclear polarization (DNP) of ^{13}C labeled pyruvate followed by rapid dissolution generates an injectable contrast agent with a four order-of-magnitude signal enhancement [Ardenkjær-Larsen *et al.*, 2003] enabling the measurement of the spatial distribution of pyruvate and its conversion to lactate, alanine, and bicarbonate. The conversion of pyruvate to lactate catalyzed by the enzyme lactate dehydrogenase is of particular interest, as the kinetics of this process have been shown to be sensitive to the presence and severity of disease in preclinical models [Kurhanewicz *et al.*, 2011; Golman *et al.*, 2003; Golman *et al.*, 2006b; Golman *et al.*, 2006a; Park *et al.*, 2010; Chen *et al.*, 2007; Albers *et al.*, 2008; Merritt *et al.*, 2007; Lupo *et al.*, 2010; Zierhut *et al.*, 2010; Witney *et al.*, 2011].

Acquiring hyperpolarized ^{13}C images presents numerous challenges. Typically, multiple frequency components must be imaged in a time period short compared with the spin-lattice relaxation time T_1 of the label. Spatially and temporally resolved dynamic imaging of substrate conversion requires even faster acquisition speeds. The low gyromagnetic ratio of carbon-13 ($\approx$ 1070 Hz / G) requires imaging gradient lobes to have roughly four times the area to achieve the same field of view and resolution compared to proton. This limits the maximum achievable velocity through k space given the peak gradient amplitude and slew rate constraints on clinical imaging systems.

Several novel techniques have been developed to rapidly acquire ^{13}C images. A small-angle band-selective excitation radio frequency (RF) pulse [Lau *et al.*, 2011; Larson *et al.*, 2008] followed by a train of rapid imaging gradient pulses such as echo planar imaging (EPI)

[Cunningham *et al.*, 2008] or spiral readouts [Lau *et al.*, 2010] allows for rapid imaging of single frequencies. The transmitter frequency is offset periodically for each temporal phase, and dynamic images of multiple frequency components can be acquired in an interleaved manner. Gradient echo images acquired at multiple echo times can also be used to resolve multiple frequency components via least squares inversion of the image phase [Reeder *et al.*, 2007; Levin *et al.*, 2007; Leupold *et al.*, 2009]. Although the long scan time from three dimensional phase encoding typically precludes three dimensional spatially-resolved dynamic spectroscopic imaging, echo planar spectroscopic imaging (EPSI) readouts [Larson *et al.*, 2010] and compressive sensing acquisitions [Hu *et al.*, 2008; Larson *et al.*, 2011] can sufficiently increase acquisition speed to enable dynamic imaging.

In this study, we developed an echo planar imaging sequence for dynamic imaging of [1-^{13}C] lactate and [1-^{13}C] pyruvate. Frequency separation was achieved by spatial misregistration in the phase-encoded direction by the appropriate choice of echo spacing. Suppression of the pyruvate-hydrate and alanine resonances is achieved through an optimized spectral-spatial RF waveform. The signal dynamics were simulated using two site exchange models for the pyruvate-to-lactate conversion. These models highlight the benefit of applying differential flip angles to pyruvate and lactate, and optimal combination of these angles was studied along with the signal tradeoffs. Dynamic imaging was demonstrated in a transgenic mouse model, and phantom validations of the RF pulse and imaging gradient frequency selectivity were performed. Given that this method separates frequencies using the low effective bandwidth in the phase-encoded EPI direction, imaging of resonances with small frequency separations would be challenging. This is due to the fact that echoes must be spaced far apart to generate an adequate spatial shift. However, this technique is more readily applicable to imaging two compounds with large chemical shift dispersions since the phase-encoded dimension can be aliased multiple times while still generating a small image-domain shift. The only limitation is that the frequency-encoded field of view must large enough to encode the shifts in the frequency-encoded dimension.

5.3 Theory

5.3.1 Frequency Separation

Two noninteracting spins that are encoded by an echo-planar readout will be spatially shifted based on their difference in chemical shift. The spins have Larmor frequencies ω_1 and ω_2 with a chemical shift dispersion $\Delta\omega = \omega_2 - \omega_1$. The signal is spatially encoded after RF excitation using an flyback EPI gradient waveform with N_{int} interleaves and N_{etl} equally spaced echoes (with spacing t_{esp}). For $N_{int} > 1$, the echo train is shifted in subsequent repetitions by t_{esp}/N_{int} to mitigate ghosting errors [Feinberg and Oshio, 1994]. With the transmitter and receiver set at the mean of the two frequencies and phase encoding along the y dimension, the two-dimensional k space image is

$$F(k_x, k_y) = F_1(k_x, k_y)e^{-i\phi(k_y)}e^{-i\Delta\omega TE_1/2} + F_2(k_x, k_y)e^{+i\phi(k_y)}e^{+i\Delta\omega TE_1/2} \tag{5.1}$$

where $F_1(k_x, k_y)$ and $F_2(k_x, k_y)$ are the images of ω_1 and ω_2, and

$$\phi\left(k_y\right) = \frac{t_{esp}\Delta\omega k_y}{2N_{int}\Delta k_y}. \tag{5.2}$$

Here, $\Delta k_y = 1/FOV_y$ is the spacing of k_y lines. TE_1 is the distance from the midpoint of the RF excitation to the midpoint of the first gradient readout lobe. The phase factors $\exp(\pm i\Delta\omega TE_1/2)$ are independent of k_y and can be excluded from further analysis. The Fourier transformed image is

$$f(x, y) = f_1\left(x, y - y_s\right) + f_2\left(x, y + y_s\right), \tag{5.3}$$

where

$$y_s = \frac{\phi(k_y)}{2\pi k_y} = \frac{t_{esp}\Delta\omega FOV_y}{4\pi N_{int}}. \tag{5.4}$$

We define the quantity $\Phi = y_s/FOV_y$, the fraction of the field of view the image is shifted. Since y is a phase-encoded dimension, this shift is periodic ($\Phi + N_{alias} = \Phi$, with N_{alias} an integer). Substituting into (5.4), this relation gives a compact form for the echo spacing in terms of the other imaging factors:

$$t_{esp} = \frac{4\pi(\Phi + N_{alias})N_{int}}{\Delta\omega}. \tag{5.5}$$

If the transmitter is at the true mean frequency, then the shift of each image will be equal and in opposite directions as shown by (5.3). If the resonance frequency if shifted, the images will be shifted asymmetrically about the center, but their relative shift with respect to each other will be the same.

With the appropriate choice of echo spacing, we can resolve two frequencies spatially in the phase-encoded direction. With $\Phi = 1/4$ and FOV_y set to at least twice the object's extent in y, equations (5.4) and (5.5) imply that images of ω_1 and ω_2 are generated side by side in y. N_{alias} can be treated as a design parameter: for large $\Delta\omega$, we can let $N_{alias} > 0$ to maintain a reasonably short t_{esp} while still generating side by side images. For pyruvate and lactate at 3T, $\Delta\omega \approx 2\pi \times 392$ Hz, so allowing for aliasing is not necessary.

Although the acquisition bandwidth of the frequency-encoded direction is much greater than that of the phase-encoded dimension, these shifts can be corrected for since the images of the two frequencies are not spatially overlapping. For larger echo spacings, the readout bandwidth is lowered to increase the sampling duty cycle and SNR [Yen *et al.*, 2009], so characterization of the shift in the frequency direction is important. With the transmitter set at the mean of the two frequencies and the frequency encoding along x, the shift is

$$\Delta x = \frac{\Delta\omega FOV_x}{4\pi BW_{read}} \tag{5.6}$$

where FOV_x and BW_{read} are the field of view and the readout bandwidth in the x dimension

respectively. Since a filter is applied in this dimension to eliminate aliasing, the field of view must be large enough to account for the shifts. If L_x is the spatial extent of the object in x, then

$$FOV_X \geq L_x + 2\Delta x. \tag{5.7}$$

Provided this condition is met, the frequency-encoded shift can be accounted for by shifting the images by $\pm\Delta x$ from (5.6) similar to the technique used in [von Morze *et al.*, 2011b].

This simultaneous encoding method differs from scanning individual frequencies one at a time in several important respects. Since FOV_y must be twice the object's spatial extent, the minimum number of EPI phase encodes per scan is doubled from acquiring a single frequency. The total scan time, however, is roughly constant since the minimum number of scans is halved. The number of RF excitations applied at each frequency is doubled with simultaneous acquisition suggesting an analysis of the effects of depolarization from RF saturation and cumulative signal encoded as a function of excitation angle imparted to each frequency.

5.3.2 Simulation of Excitation Angle Effects on Exchanging Hyperpolarized Spins

The sequence implemented uses a spectral spatial RF pulse [Meyer *et al.*, 1990] to suppress the alanine and pyruvate-hydrate signal while allowing for different excitation angles imparted to pyruvate and lactate. Qualitatively, a small flip angle on pyruvate is expected to yield a larger cumulative signal on lactate since depolarization is reduced; this effect is shown empirically in [Larson *et al.*, 2008]. To quantify the tradeoffs in applying differential flip angles to lactate and pyruvate, a simulation was developed to study the depolarization effects from RF saturation as well as the net signal encoded as a function of flip angle. The simulation was based on a two-site exchange model for pyruvate and lactate after infusion into the animal [Lupo *et al.*, 2010; Zierhut *et al.*, 2010; Kettunen *et al.*, 2010;

Brindle *et al.*, 2011]. This model is determined by k_{PL} which characterizes the conversion rate from pyruvate to lactate, k_{LP} which determines the rate in the reverse direction, and $\rho_P = 1/T_{1,P}$ and $\rho_L = 1/T_{1,L}$, the spin lattice relaxation rates for pyruvate and lactate respectively. θ_P and θ_L are the flip angles for pyruvate and lactate, and their effect on the longitudinal polarization is accounted for by a quasi-continuous approximation to the actual discrete effect. Unlike the methods presented in [Nagashima, 2008; Zhao *et al.*, 1996; Peterson *et al.*, 2011] where an optimal flip angle schedule is derived to maximize the integrated signal intensity of hyperpolarized spins, we only analyze the time-independent flip angle scenario. This is due to the fact that a time-dependent signal weighting could preclude quantitative analysis of kinetic data.

Let $M_{z,P}(t)$ and $M_{z,L}(t)$ be the longitudinal magnetization components of lactate and pyruvate respectively. The state vector $M_z(t)$ is defined as

$$M_z(t) = \begin{pmatrix} M_{z,P} \\ M_{z,L} \end{pmatrix}. \tag{5.8}$$

Combining with a continuous model for RF saturation and T_1 decay with the chemical dynamics, the state space model can be represented as

$$\frac{d}{dt} M_z(t) = A M_z(t), \tag{5.9}$$

with

$$A = \begin{pmatrix} -\rho_P - k_{PL} + \frac{1}{TR}(\cos\theta_P - 1) & k_{LP} \\ k_{PL} & -\rho_L - k_{LP} + \frac{1}{TR}(\cos\theta_L - 1) \end{pmatrix}, \tag{5.10}$$

where TR is the repetition time. The solution to (5.9) is a matrix exponential that can be

calculated using inverse Laplace transforms:

$$\begin{aligned} M_z(t) &= e^{At} M_z(0) \\ &= \mathcal{L}^{-1} \left[sI - A \right]^{-1} M_z(0). \end{aligned} \tag{5.11}$$

Here, s is the complex frequency variable, I is the 2×2 identity matrix, and

$$M_z(0) = \begin{pmatrix} 1 \\ 0 \end{pmatrix} \tag{5.12}$$

The cumulative signal for pyruvate and lactate can be modeled as

$$S_P = \sum_{k=1}^{N_{acqs}} \sin\theta_P \cdot M_{z,P}(k \cdot TR) \tag{5.13}$$

$$S_L = \sum_{k=1}^{N_{acqs}} \sin\theta_L \cdot M_{z,L}(k \cdot TR). \tag{5.14}$$

The initial conditions represented by equation (5.12) imply that the pulse sequence begins immediately after substrate infusion, and the function describing the time dependence of the substrate delivery is ignored. This could be accounted for as in [Zierhut *et al.*, 2010] but was not performed here since we are only concerned with getting an estimate of signal intensity as a function of flip angle.

5.4 Methods

5.4.1 Simulations

The signal of the hyperpolarized pyruvate and lactate as acquired with this sequence were simulated in Mathematica (Wolfram Research, Champaign, Il, USA). The solution (5.11)

to equation (5.9) and the signal intensities (5.14) and (5.13) were computed as functions of both θ_P and θ_L at k_{PL} = .01 s^{-1}, .05 s^{-1}, and .09 s^{-1}. These values of the forward rate constant represent the range of previously measured kinetic parameters for transgenic mice [Zierhut *et al.*, 2010]. Backward conversion from lactate to pyruvate was assumed to be negligible ($k_{LP} = 0$). Relaxation times of $T_{1,P} = T_{1,L}$= 25 s were used for the simulations in Figure 5.2. These values were chosen as rough estimates and are similar to the previously quoted values of $T_{1,L}$ =21 s and $T_{1,P}$ =32 s measured from slices encompassing the tumors of TRAMP mice [Zierhut *et al.*, 2010] and $T_{1,L} = T_{1,P}$ =33 s measured from spatially-resolved saturation transfer data in a mouse [Kettunen *et al.*, 2010].

Since the $T_{1,L}$ and $T_{1,P}$ values are widely variable and cannot be measured beforehand, the non-optimality of the integrated signal as a function of flip angle and relaxation time was also simulated. The ratio of the integrated signal S_L acquired using a $\theta_L = 15°$ flip angle to that acquired using the T_1-optimal flip angle was simulated in Figure 5.3a. The optimal flip angle is shown in Figure 5.3b.

The mean repetition time was used in simulations:

$$TR = \frac{N_{int} TR_{act} + t_{delay}}{N_{int}}, \tag{5.15}$$

where TR_{act} is the actual repetition time used in the scan and t_{delay} is the delay period between dynamic acquisitions. N_{acqs} was set to $N_{int} \times N_{phases} = 4 \times 20$, where N_{phases} is the number of dynamic acquisitions.

5.4.2 Radio Frequency Excitation

A spectral-spatial pulse giving a nominal excitation flip angle of 7.5° to pyruvate, 15° to lactate, and 0° to both alanine and pyruvate hydrate was designed for this sequence (Figure 5.4). This choice of flip angles was based on the simulation results of the cumulative lactate signal as a function of both θ_P and θ_L given the repetition time for the sequence (see Figure

5.2). The spectral filter was designed using a spectral factorization / convex optimization for reduced peak B_1 and minimum sampling rate [Larson *et al.*, 2008; Kerr *et al.*, 2008]. Spatially-selective sublobe samples were played using a 0.5 VERSE fraction [Conolly *et al.*, 1988], and the irregular $t - k_z$ sampling was corrected for using the least-squares algorithm presented in [Cunningham *et al.*, 2008]. The selectivity of the RF pulse was verified in a proton phantom using body coil for excitation (Figure 5.4).

5.4.3 Acquisition Parameters

This sequence was demonstrated in a single slice in the coronal plane. The phase encoding was set along the left/right dimension, and frequency was set along superior/inferior. The phase field-of-view FOV_y was set to at least twice the extent of the object. For mouse imaging, this was always possible using $FOV_y = FOV_x = 10$ cm. The transmitter resonance was set at the mean of the *in vivo* resonant frequencies of [1-^{13}C] pyruvate and [1-^{13}C] lactate, corresponding to $\omega/2\pi = 32.1315$ MHz on the 3T scanner. The echo spacing was set for a $\pm FOV_y/4$ shift ($\Phi = 1/4$) so that the sequence would generate pyruvate and lactate images side by side in y. The pyruvate/lactate frequency separation at 3T is $\Delta\omega/2\pi = 384$ Hz. A 32×32 grid was acquired in plane using $N_{etl} = 8$, $N_{int} = 4$, so from equation (5.5), $t_{esp} = 5.19$ ms. The readout bandwidth was then reduced to ± 5 kHz increase the sampling duty cycle and SNR. With the given resolution and readout bandwidth, a shift of 0.6 times the pixel size is expected in the readout (S/I) direction. This effect was neglected, but could be compensated for with an image domain shift in S/I. The total repetition time $TR = 80$ ms giving a single slice scan time of $N_{int}TR = 240$ ms. See Figure 5.1 for a diagram explaining the timing parameters.

5.4.4 Animal Experiments

Experiments were performed on a GE 3T Signa MRI system (GE Healthcare, Waukesha, WI, USA). A custom dual-tuned ^{1}H / ^{13}C, transmit / receive mouse coil was used for carbon and proton imaging. Prior to infusion of the hyperpolarized contrast, the transmitter attenuation was calibrated by obtaining images at multiple attenuation settings from a syringe containing 0.7 mL of 8 M ^{13}C-urea placed next to the animal. 24 uL of 99 % [1-^{13}C] pyruvate was mixed with the OX063 radical (GE Healthcare, Oslo, Norway) and polarized in an Oxford Instruments Hyperpsense polarizer (Oxford Instruments Biotools, Oxford, UK) operating at 3.35 T and 1.2 K. After approximately one hour of 94.114 GHz microwave irradiation, the sample was rapidly dissolved in 4.25 mL of a heated TRIS / NaOH solution giving a final concentration of 80 mM. A transgenic prostate tumor bearing mouse [Greenberg *et al.*, 1995] was injected with 350 μL of the hyperpolarized solution over 8 seconds. Imaging was started 20 seconds after the beginning of injection. A 3 second delay period is inserted between slices giving a temporal resolution of $t_{delay} + N_{int}TR = 3.2$ seconds.

5.4.5 Reconstruction

The pulse sequence produces the pyruvate and lactate images side by side in the left/right dimension. The image was shifted by $+FOV_y/4$ and multiplied by an ideal filter with width $FOV_y/2$ to generate a pyruvate image with proper spatial localization. The same process was repeated for lactate images, but the shift was in the opposite direction.

5.5 Results and Discussion

Figure 5.2 shows plots summarizing the simulation results. The integrated lactate signal intensity from Figure 5.2a has a maximum at approximately $\theta_L \approx 15^\circ$ and is approximately independent of k_{PL} for the range of values simulated. As a function of θ_P, S_L is a mono-

tonically decreasing function (Figures 5.2b, 5.2d) as expected since we assumed one-way conversion. Since the pyruvate signal is generally much stronger than lactate, θ_P was set to 7.5°. According to the model, this would sacrifice roughly 30% of S_P (2.5/3.5) versus encoding with the θ_P optimizing S_P ($\approx$ 15° as shown in Figure 5.2c). However, S_L is expected to increase 30% (1.8/1.4) from encoding using $\theta_P = 7.5°$ instead of 15° (Figure 5.2b). Figure 5.3 shows the simulated signal acquired if θ_L was set based on a $T_{1,L}$ differing from the actual value. The relative S_L is within 10% of the maximum for $T_{1,L}$ values down to 9 seconds and is even more stable for $T_{1,L} > 25$ s. Variations in $T_{1,P}$ had less then a 5% influence on the relative signal for the range of $T_{1,P}$ (5 s-50 s) simulated. Variations in k_{PL} did not strongly influence the non-optimality of the integrated signal nor the optimal θ_L for different relaxation values.

Figures 5.5, 5.6, and 5.7 show preliminary data acquired from infusion of hyperpolarized pyruvate into a TRAMP mouse. Figure 5.5 shows the coronal spin echo localizer (left) and a representative pyruvate / lactate image (right). Figure 5.6 shows anoverlay of the color-mapped SNR values of the hyperpolarized images. For ease of viewing, only every other dynamic repetition is displayed. Figure 5.7 shows the average SNR of all the pixels within two ROIs drawn around the prostate tumor and the thorax of the mouse. This figure highlights how multiband excitation with the EPI sequence generates comparable SNR for lactate and pyruvate ($\approx$ 25 in the prostate tumor and $\approx$ 9 in the thorax).

Some limitations of the pulse sequence presented are discussed. Ghosting artifacts stemming from interleaving strongly degrades the images in this simultaneous encoding strategy since these artifacts appear along the same dimension in which the different frequencies are resolved. Although this effect was largely mitigated by the echo shifting strategy, some persistent ghosts were visible in early time points. This was likely due to the fact that in the early time points, the contrast is largely concentrated in the vasculature, and the echo shifting cannot fully correct the phase errors from flowing spins. Setting t_{esp} to a value larger than the minimum does make the sequence more susceptible to geometric distortion from B_0

homogeneity. However, the value used (5.2 ms) is on the order of the minimum achievable spacing by the clinical scanner using whole-body gradients ($\approx$ 3 ms) for the same field-of-view and resolution. Combined with the low gyromagnetic ratio of carbon, we do not expect geometric distortions to be detrimental, and they could be compensated for using a B_0 field map and the methods presented in [Jezzard and Balaban, 1995]. The transverse dynamics of this sequence including T_2^* effects were not investigated, and some signal loss by the long TE_1 due to the spectral-spatial RF pulse is to be expected. While using spectral-spatial excitation is necessary for encoding lactate and pyruvate, this pulse sequence should show the greatest advantage for encoding only two frequencies. In this case, a short pulse with a broad excitation band could be used for excitation, and TE_1 could be made extremely short, allowing for a longer echo train and signal enhancement with reduced T_2^* loss.

5.6 Conclusion

Simultaneous encoding of pyruvate and lactate using a flyback echo planar sequence is demonstrated. This method spatially resolves the two frequencies by deliberate chemical shift misregistration based on proper selection of the echo spacing. Robust performance of the pulse sequence was observed in phantom and in vivo hyperpolarized experiments. Simulations of the combined exchange, excitation, saturation, and relaxation effects of hyperpolarized compounds were implemented. These simulations show promise in determining optimum flip angle for the metabolic product as well as elucidating the tradeoff in product signal encoded versus substrate flip angle. Possible drawbacks of the pulse sequence presented as well as some interesting extensions are discussed.

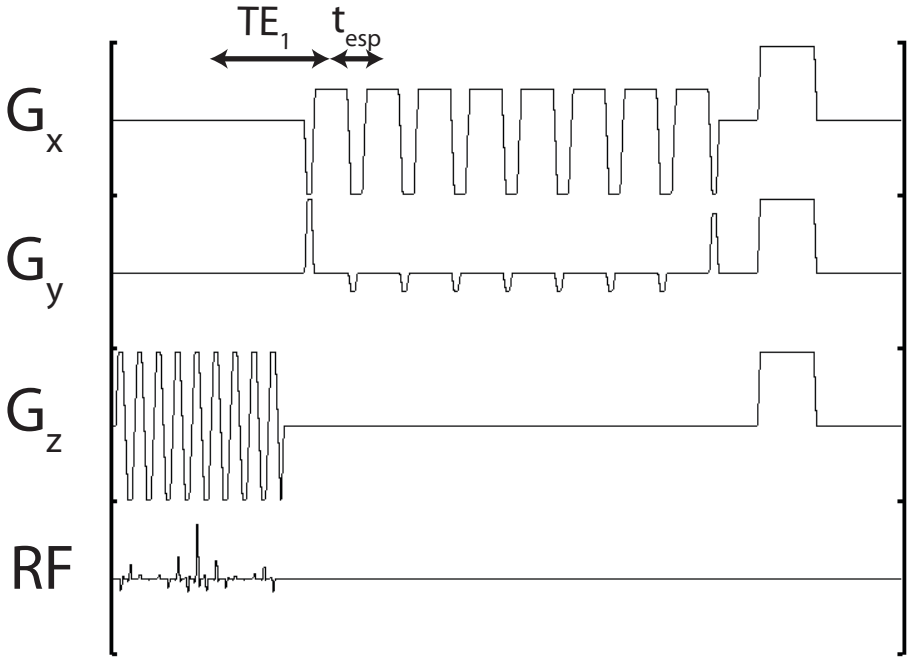

Figure 5.1: RF and gradient waveforms in a single repetition. $t_{esp} = 5.2ms$, $TE_1 = 13.5$ ms, $TR = 80$ ms. To increase the sampling duty cycle, the readout bandwidth was lowered to ± 5 kHz corresponding to a readout gradient strength of 1 G/cm.

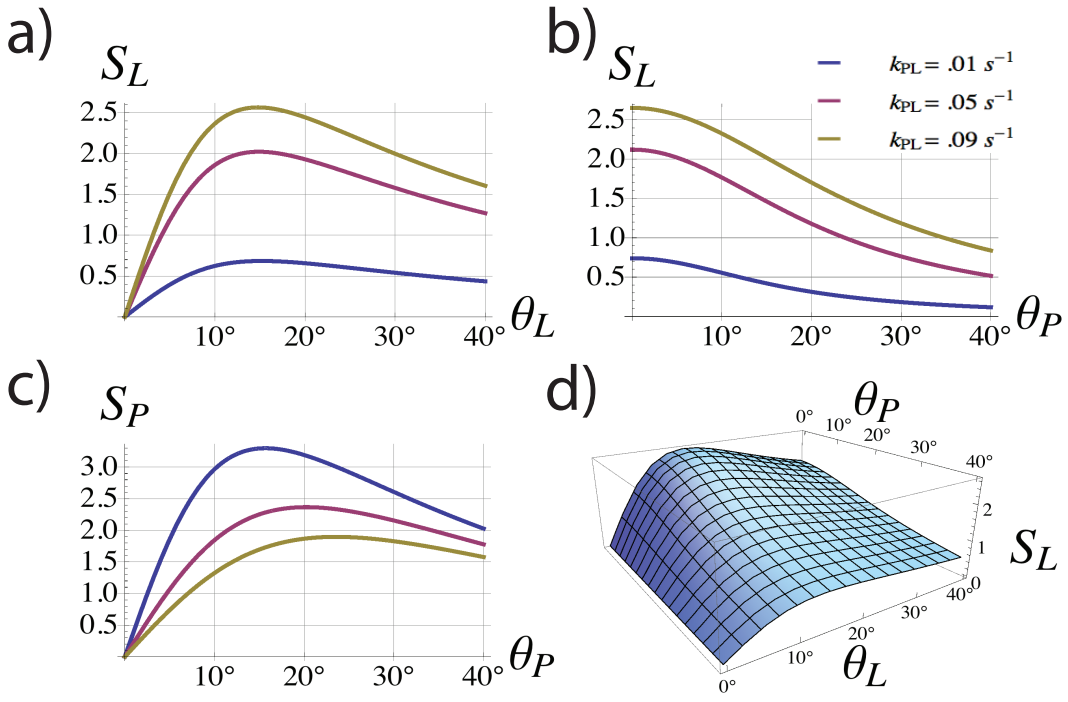

Figure 5.2: p
yruvate and [1-^{13}C]lactate signal as a function of differential flip angle on each metabolite] Total encoded signal of pyruvate (S_P) and lactate (S_L) given by equations (5.13) and (5.14) respectively. Simulations were computed assuming $T_{1,L} = T_{1,P} = 25$s. S_L and S_P both show maxima as functions of θ_L and θ_P, respectively (a,c). However, the lactate signal S_L decreases monotonically with increasing the pyruvate flip angle θ_P (b,d) suggesting the use of a small θ_P value as to not diminish S_L. For the given repetition times and assumed relaxation rates, the optimal θ_L was approximately 15° and was largely independent on the conversion times (a).

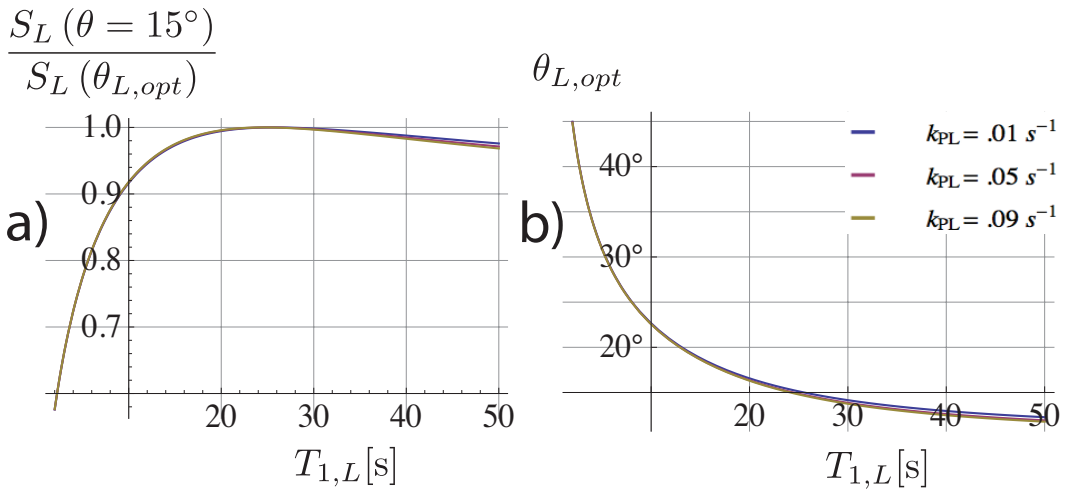

Figure 5.3: a) the ratio of S_L calculated for a lactate flip angle of $\theta_L = 15°$ to the S_L value computed with the optimal angle for the given lactate relaxation time $T_{1,L}$. The optimal flip angle is shown in b). Both plots assume $T_{1,P} = 25$ s. The acquired S_L using a 15° flip is within 10% of the optimum value for $T_{1,L}$ values down to 9 seconds.

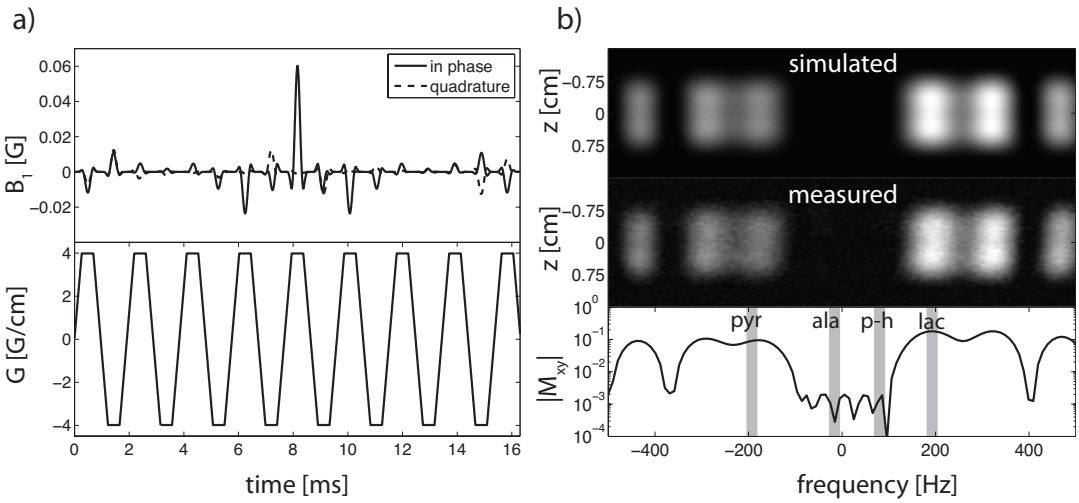

Figure 5.4: (a) RF waveform (top) and slice select gradient (bottom). The total waveform duration is 16.9 ms. (b) spectral / spatial excitation profile from Bloch simulation (top), measured excitation profile from a proton phantom (center), and simulated spectral profile at $z = 0$ shown on a semilog scale (bottom). The spectral locations of pyruvate, alanine, pyruvate-hydrate, and lactate are denoted. The minimum full width half max of the spatial profile is 1.5 cm.

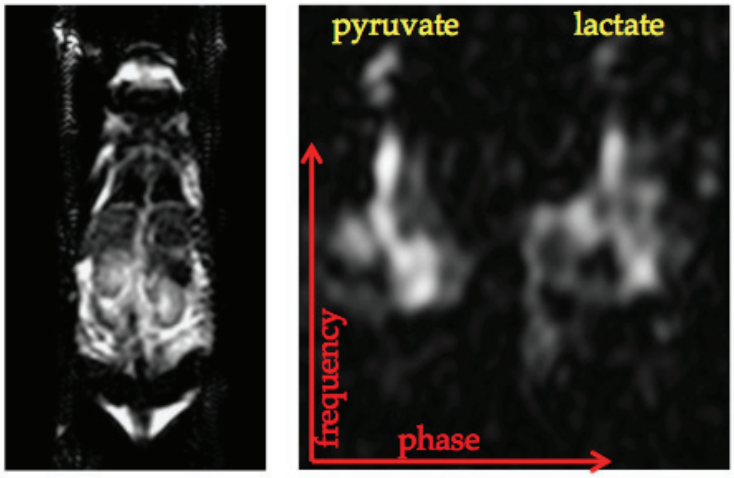

Figure 5.5: Coronal FSE localizer (left) and a representative image produced by the pulse sequence (right).

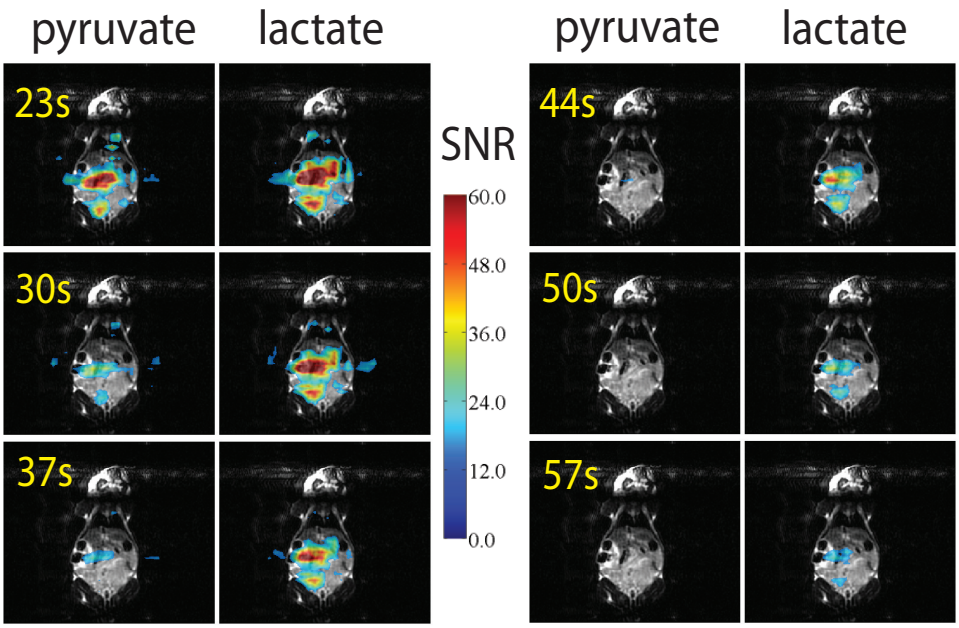

Figure 5.6: Every other dynamic repetition overlaid on a coronal FSE localizer. Pyruvate and lactate SNR values represented as overlays. Concordant with prior studies in the TRAMP model, the tumor shows persistent lactate signal at the later time points.

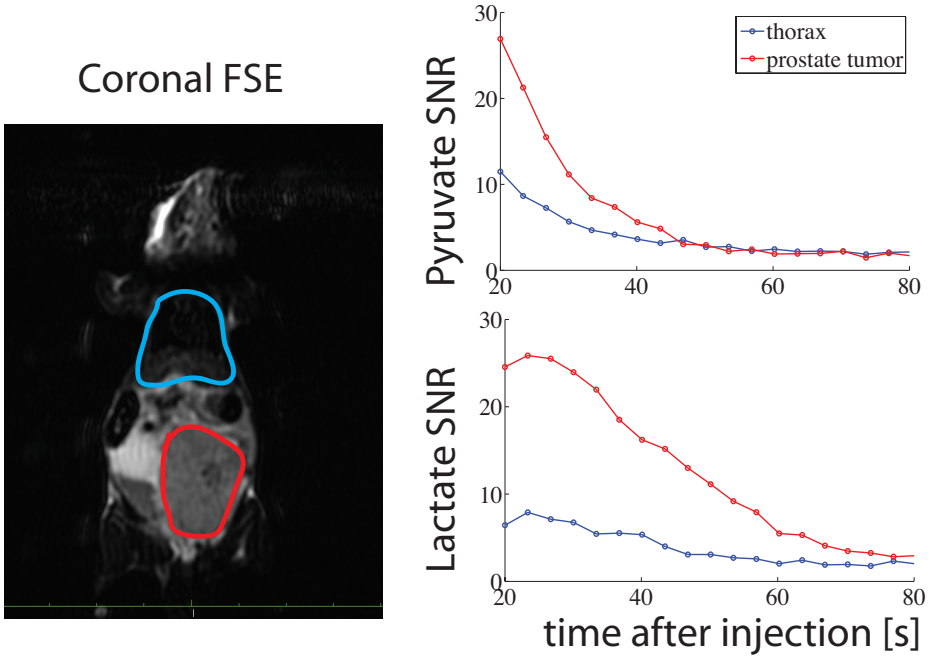

Figure 5.7: Coronal FSE localizer on the left shows the locations of the two ROIs. The mean SNR of all the pixels within each ROI is plotted at each repetition on the right. The comparable SNR values between pyruvate and lactate in the early time points highlight the benefit of the multiband excitation pulses.

Chapter 6

Spin Echo EPI for Hyperpolarized ^{13}C Imaging on a Clinical MRI System: Diffusion Weighting and Low Power Refocusing Pulses

6.1 Abstract

This study demonstrated the feasibility of hyperpolarized ^{13}C spin echo EPI on a clinical MRI system. Two chief challenges were addressed. The first was the need for low power transmit-B_1-insensitive refocusing pulses that cover the frequency range of the metabolites of interest. The second was a method for generation of high b values (> 800 mm^2/s) within a single repetition time (TR) and within an echo time (TE) much shorter than previously reported T_2 values.

6.2 Introduction

Discrimination of intra- and extra-cellular components of the ^{13}C signal, suppression of blood flow, and an increase in tumor contrast-to-noise ratio (CNR) are the chief motivations for many recent studies using diffusion weighted acquisitions [Koelsch *et al.*, 2013; Kettunen *et al.*, 2013; Schilling *et al.*, 2013; Larson *et al.*, 2012] with hyperpolarized ^{13}C MRI [Ardenkjær-Larsen *et al.*, 2003; Golman *et al.*, 2006b]. Clinical translation of these techniques will be extremely challenging due to clinical MRI scanner peak RF and gradient amplitude limitations. All prior hyperpolarized ^{13}C diffusion-weighted acquisitions using the pulsed gradient spin echo sequence (PGSE) [Koelsch *et al.*, 2013; Kettunen *et al.*, 2013; Schilling *et al.*, 2013] used narrow bore spectrometers or small animal imaging systems with peak gradient strengths hundreds of times larger than those of clinical MRI scanners. Stimulated echo techniques have been proposed to overcome this challenge [Larson *et al.*, 2012], but they suffer from a 50% signal reduction. Furthermore, the use of adiabatic RF spin echo pulses with ^{13}C nuclei [Cunningham *et al.*, 2007; Kettunen *et al.*, 2013] requires prohibitive peak RF strength to maintain the adiabatic condition and, therefore, to enable reliable spin refocusing over a large field of view (FOV).

In this study we designed and tested a modification of the twice refocused spin echo sequence [Reese *et al.*, 2003] using low power, reduced bandwidth adiabatic 180° refocusing pulses. The high diffusion weighting of the twice refocused spin echo sequence coupled with a flyback echo planar imaging (EPI) readout provides a single shot imaging acquisition with b values of > 1000 s/mm^2, echo times less than one fourth the measured *in vivo* T_2 values of [1-^{13}C]lactate, and peak RF and gradient strengths within the limits of current commercially available MRI gradient and ^{13}C RF transmitter hardware. The effective refocusing FOV of the transmitter was estimated based on the simulated transmitter profile and its measured peak output at isocenter. The sequence was tested with hyperpolarized ^{13}C phantoms and demonstrated for *in vivo* use with Spraque Dawley rats and TRAMP mice.

6.3 Methods

6.3.1 Sequence design

Similar to prior ^{13}C spin echo acquisitions [Cunningham *et al.*, 2007; Josan *et al.*, 2011; Kettunen *et al.*, 2013; Koelsch *et al.*, 2013], the sequence consisted of a slice-selective excitation followed by two adiabatic refocusing pulses. A symmetric-frequency response, 'true null" spectral spatial pulse [Meyer *et al.*, 1990] was designed similar to those used in prior hyperpolarized ^{13}C studies to excite a single metabolite [Lau *et al.*, 2010; Schulte *et al.*, 2013]. This excitation had a 60 Hz FWHM spectral bandwidth, 13 mm minimum slice thickness, 400 Hz stopband, and was designed to alternatively excite [1-^{13}C]lactate and [1-^{13}C]pyruvate (which have a 390 Hz chemical shift separation at 3T).

The diffusion weighting was generated via spin echo crusher gradient pulses played with opposing polarity [Reese *et al.*, 2003] on either side of each spin echo pulse (Figure 6.1). This sequence achieves large b values by leaving the magnetization dephased during the delay period between spin echoes. The diffusion weighting was calculated with the well known relations $b(t) = (2\pi)^2 \int_0^t \left|\vec{k}(t')\right|^2 dt'$ with $\vec{k}(t) = \frac{\gamma}{2\pi}\int_0^t G(t'), dt'$. For a fixed echo time, the b values of both the symmetric and opposed crusher lobe sequences was computed and plotted (Figure 6.1b) for 22 ms crusher pulses, 15 ms rf pulses, 87.5 ms inter-pulse spacing, corresponding to a 175 ms echo time. As evident in Figure 6.1b, part 1, the diffusion weighting of the slice select gradient was negligible ($< .007$ s/mm^2 at minimum slice thickness) and was ignored in b values calculations.

6.3.2 Adiabatic 180° pulse design

The transmitter-strength immunity afforded by adiabatic refocusing pulses have proven utility for hyperpolarized ^{13}C imaging [Cunningham *et al.*, 2007; Kettunen *et al.*, 2013; Josan *et al.*, 2011; Koelsch *et al.*, 2013] for the generation of whole-echo, phased spectra

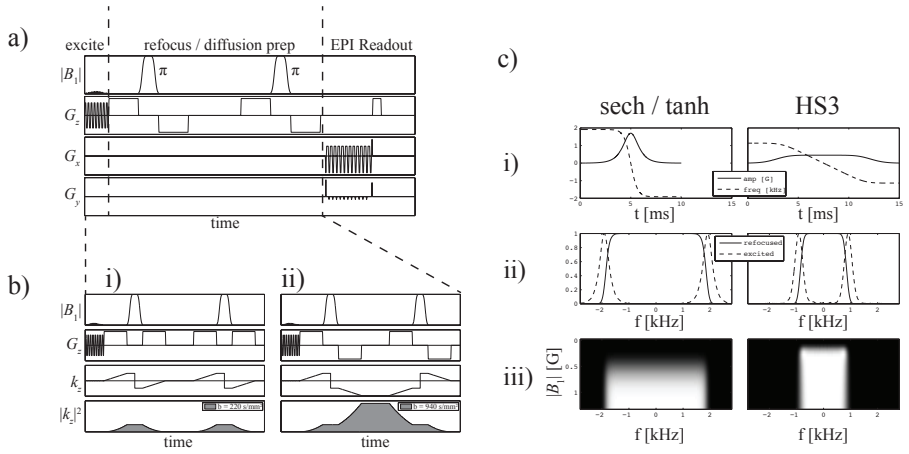

Figure 6.1: a) Sequence schematic showing the small-tip spectral spatial excitation, the twice refocused diffusion preparation, and the flyback EPI readout. b) Diffusion attenuation of the twice refocused sequences with unipolar (i) and bipolar (ii) spin echo crusher gradient pulses. The bipolar preparation leaves the magnetization dephased during the inter-pulse interval creating a large b value enhancement. c) Comparison of the hyperbolic secant spin echo pulse (left) and the HS3 pulse (right). The amplitude (i) is reduced by a factor of > 3 with the HS3 pulse. This is achieved at the expense of reduced bandwidth (ii). However, at the reduced bandwidth, the adiabatic threshold is achievable at 0.4 G (iii, right) which is well within the limits of the clamshell transmitter.

and for dynamic imaging requiring M_z preservation over multiple repetitions. Additionally, when $T_2 \gg TE$, spin echo preparations offer large signal-to-noise (SNR) benefits for fully-sampled EPI readouts since the data acquisition time is effectively doubled and the echo can be centered on the DC k space samples. The ^{13}C transmitter used for the recent clinical trial [Nelson *et al.*, 2013] has a peak output of 0.6 at isocenter. This limitation prohibits the use of the high bandwidth sech / tanh waveforms described previously [Cunningham *et al.*, 2007] which have a nominal B_1 of 1.6 G and adiabatic threshold of $\sim$ 1.4 G.

To address the peak B_1 limitation, a stretched hyperbolic secant (HSn) waveform was utilized [Park *et al.*, 2006; Tannus and Garwood, 1996; Hu *et al.*, 2009]. This analytic waveform uses a stretching parameter n to flatten the amplitude modulation function thus decreasing the peak B_1. As $n \rightarrow \infty$, the pulse approaches a chirp pulse with a square amplitude modulation and linear frequency sweep. The expression for the amplitude is

$$|B_1(t)| = B_{1,max}\ \mathrm{sech}\left(\beta t^n\right) \tag{6.1}$$

and frequency sweep is

$$\omega(t) = AB \int_0^t \mathrm{sech}^2\left(\beta \tau^n\right)\, d\tau \tag{6.2}$$

$$A = \mu B \tag{6.3}$$

$$B = \left(\int_0^1 \mathrm{sech}^2\left(\beta \tau^n\right)\, d\tau \right)^{-1}. \tag{6.4}$$

Parameters used were $n = 3$, $\mu = 8$, $\beta = 4.725$, and a total duration of 15 ms. The refocusing and excitation profile of these pulses compared to the hyperpbolic secant pulses (corresponding to $n = 1$ for the HSn waveform) with the parameters given by Cunningham et al are shown in Figure 6.1c. A significant peak amplitude reduction was achieved at the expense of pulse width (15 ms versus 10 ms) and refocused bandwidth (600 Hz verus 2000

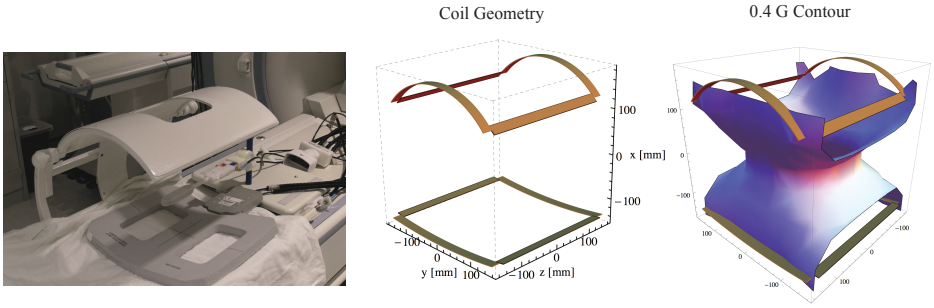

Figure 6.2: Photograph (left) and schematic (center) of the clinical ^{13}C transmitter. The right image shows the 0.4 G contour when sufficient current is applied for a 0.6 G peak B_1 at isocenter.

Hz). Despite this reduction, the bandwidth still easily handles the spectral separation of [1-^{13}C]lactate and [1-^{13}C]pyruvate at 3T (390 Hz).

6.3.3 Hardware

All data acquisition was performed on a General Electric Signa MRI scanner operating at $B_0 = 3$T ($\omega_0 = 32.131$ MHz for ^{13}C) with 4 G/cm peak gradient amplitude and 15 G/cm/ms peak slew rate. Experiments used three different RF coils for signal excitation and reception including two dual-tuned ^{13}C / ^{1}H transmit / receive birdcage resonators: one with 25 mm inner diameter, 140 mm length (intended for mouse imaging), and one with 80 mm inner diameter, 200 mm length (intended for rat imaging). Additionally, a 30 cm diameter conformal clamshell-shaped clinical Helmoholtz transmitter was utilized [Tropp *et al.*, 2011]. This coil is shown in figure 6.2 along with a magneto static simulation of its field profile [Chubar *et al.*, 1998].

6.3.4 Hyperpolarization and sample preparation

An Oxford Instruments Hypersense unit was used for dissolution DNP experiments. [1-^{13}C]pyruvate acid was mixed with 15 mM trityl radical and 1.5 mM dotarem, polarized for 1.5

hours, and dissolved in an NaOH / Tris buffer yielding a final concentration of 80 mM.

For hyperpolarized phantom experiments, 1 mL of the dissolved hyperpolarized solution was drawn in a 60 mL syringe containing 60 mL distilled H_2O yielding a final concentration of 1.3 mM [1-^{13}C]pyruvate. The final solution temperature of 27°C was verified via laser thermometry. After withdrawing into the syringe, the solution was placed in the center of the coil and allowed to settle 30 s before imaging.

6.3.5 Adiabatic 180° validation

Hyperpolarized pyruvate phantoms were prepared as described in section 6.3.4. After a 30 second delay for sample settling, the dynamic spin echo EPI imaging was initiated. The spin echo crusher durations were set to 3 ms with identical polarity so that diffusion weighting could be ignored. Single shot, single slab (60 mm thickness) coronal images were acquired dynamically with a 24×12 acquisition matrix, $TR/TE = 5$s / 100 ms, 5° flip angle. Data with a first-time-point-$SNR > 20$ were fit to a single exponential decay. This was performed twice on the 8 cm I.D. birdcage coil; one acquisition used the HS3 pulse, and one used the sech / tanh wave. Additionally, one phantom was imaged with the clamshell using an 8 channel phased array for signal reception. In all cases, depolarization from the small-tip RF excitation pulses was ignored.

This same comparison was performed *in vivo* with acquisition beginning 15 s after the beginning of a 12 s injection of hyperpolarized [1-^{13}C]pyruvate. Additionally, the spin echo EPI sequence was validated using the same acquisition parameters using the clamshell exciter and an 8 channel parallel array for reception. See Figure 2 of reference [Ohliger *et al.*, 2013] for the rat setup in the clamshell transmitter and receive array.

6.3.6 Diffusion weighting validation

The diffusion attenuation of the adiabatic twice refocused spin echo sequence was tested on hyperpolarized [1-^{13}C]pyruvate phantoms prepared as described in section 6.3.4. The sequence used the high b value configuration as shown in Figure 6.1. All 4 spin echo crusher pulses had a 22 ms plateau duration, 376 μs rise time, and 4 G/cm peak amplitude. At a TE of 175 ms, spacing between the center of the spin echo pulses was $TE/2 = 87.5$ ms, and the inter-pulse delay between the second and third spin echo crusher pulses was 22.752 ms. This corresponded to a b value of 940 s/mm^2. The sequence was imaged in hyperpolarized phantoms with a 5 s TR, 5° flip, and the crusher gradient amplitudes were incremented at each time point to 100%, 55.9%, and 10 % of their peak value (4 G/cm) corresponding to b values of 940, 274, and 9 s/mm^2, respectively. This sequence of 3 b values was repeated 10 times. All pixels with high b value $SNR > 10$ were included in analysis. After SNR thresholding, the ratio of the pixel intensities of the $b = 940$ to $b = 9$, and $b = 274$ to $b = 9$ images were calculated. These ratios were binned into histograms and plotted versus the expected attenuation from the given b values and the previously measured ADC of 1.12×10^{-3} mm^2/s of [1-^{13}C]pyruvate in aqueous solution at 27°C. Depolarization from the small-tip RF excitation pulses was ignored.

The diffusion attenuation was also tested in vivo in a TRAMP mouse model of prostate cancer [Greenberg *et al.*, 1995]. 3 [1-^{13}C]pyruvate and 3 [1-^{13}C]lactate images were acquired 30 s post injection of hyperpolarized [1-^{13}C]pyruvate. Similar to the phantom tests, each compound was imaged with b values of 940, 274, and 9 s/mm^2. A 30° flip angle and 250 ms TR was used in this acquisition for a total scan time of 1.5 s.

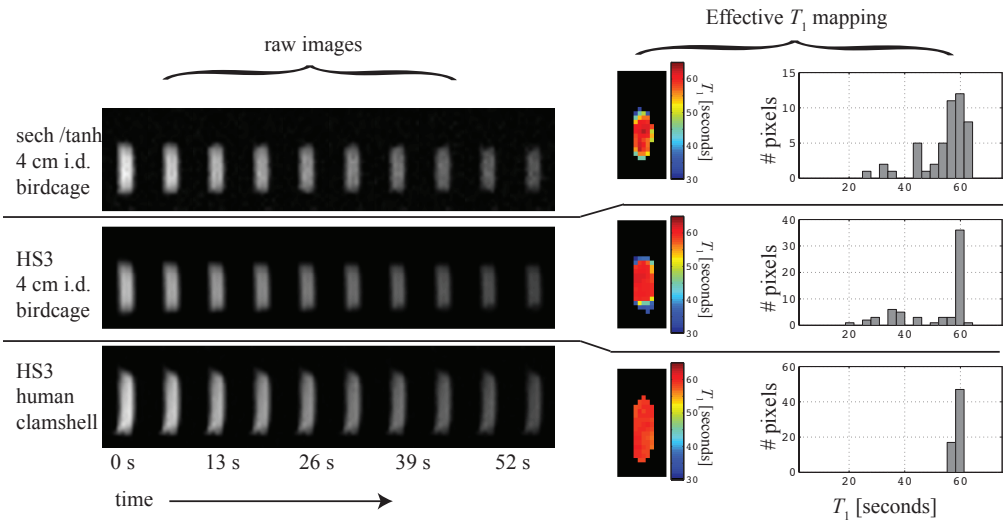

Figure 6.3: The dynamic raw images are shown on left for both pulses. The bottom series shows images from the clamshell transmit / 8 channel paddle receive array using the HS3 pulse. The effective T_1 maps are shown center; maps were calculated ignoring signal loss from excitation pulses. Pixel histograms of effective

6.4 Results

6.4.1 Adiabatic 180° validation

The hyperpolarized phantom experiments using both spin echo pulses are shown in Figure 6.3a. With the birdcage coil, both pulses showed some saturation of the hyperpolarized magnetization at the coil edges. This is easily visualized in the effective coil T_1 maps (Figure 6.3b). The proportion of pixels with an effective T_1 within 10% of the expected 59 s value was 73% for the phantom imaged with the sech / tanh pulse and 67% with the HS3 pulse. For the phantom imaged in the clamshell, all pixels above the SNR threshold had effective T_1 values within 10% of the expected value.

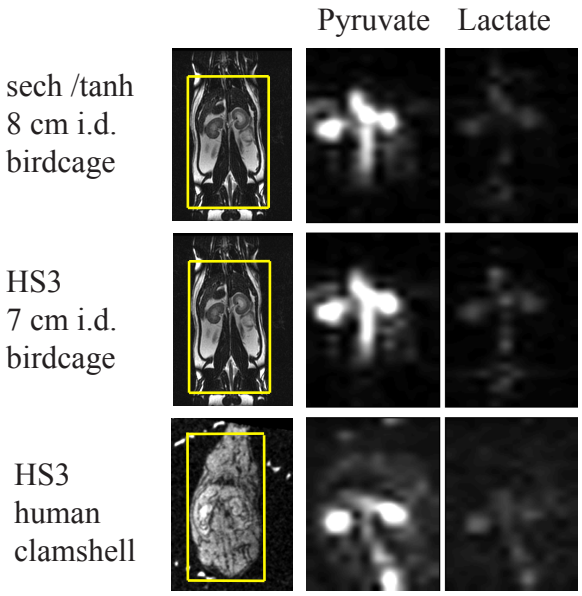

Figure 6.4: [1-^{13}C]pyruvate and 3 [1-^{13}C]lactate images acquired 10 s post injection of hyperpolarized [1-^{13}C]pyruvate in a Sprague Dawley rat. Pyruvate / lactate ratios are comparable for all experiments. Dynamic data was not compared as in phantom experiments due to use of a progressive flip angle acquisition.

6.4.2 Diffusion weighting validation

Hyperpolarized syringe images acquired at multiple b values are shown in Figure 6.5a. The distribution of the pixel signal ratios of images acquired at 2 different pairs of b values is shown in Figure 6.5b along with the expected attenuation e^{-bD} of 0.72 ($b = 305/b = 10$) and 0.34 ($b = 976/b = 10$) assuming the previously reported diffusivity $D = 1.12 \times 10^{-3}$ mm^2/s [Koelsch *et al.*, 2013] and ignoring depolarization from RF excitation. Figure 6.5c shows the [1-^{13}C]lactate image acquired 30 post injection of hyperpolarized [1-^{13}C]pyruvate.

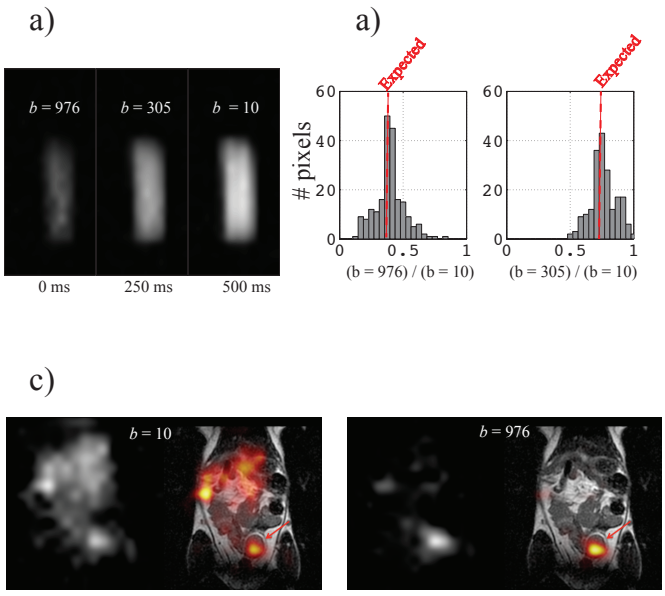

Figure 6.5:
a) validation of the diffusion weighting in a hyperpolarized phantom. b) histograms of relative signal attenuation are shown on right along with the expected attenuation with diffusion coefficients given by Koelsch et al. c) [1-^{13}C]lactate images acquired 30 s post injection of hyperpolarized [1-^{13}C]pyruvate in a transgenic mouse prostate cancer model.

6.5 Discussion

The *in vivo* diffusion weighted images shown in Figure 6.5c are concordant with prior studies which showed that diffusion weighting can increase tumor contrast to noise ratio for [1-^{13}C]lactate after [1-^{13}C]pyruvate injection. This fact could be value for such an acquisition in a clinical setting

The hyperpolarized spin echo tests on phantoms shown in Figure 6.3 show the efficacy of adiabatic refocusing even on the clinical transmitter. This figure also highlights the caveat of using 180° pulses with hyperpolarized nuclei; when the sample extends past the transmitter edges, saturation of polarization is a necessary consequence. Spin echo imaging of clinical subjects would only likely be a reasonable strategy after hyperpolarized bolus arrival to the region of interest since potential arterial inflow from regions outside the coil would very likely be saturated in the fringe fields. This would preclude the monitoring of bolus arrival and kinetic rate constant fitting. However, single, or a combination of a few images with differing diffusion contrast would likely be adequate as a diagnostic tool.

In two experiments not shown, imaging with the sample below the adiabatic threshold result in virtually no encoded SNR, even on the first time point. In a clinical setting, this fact means that great care must be taken to ensure the region within the coil is above the adiabatic threshold since, this results in no detected signal even in the first TR.

6.6 Conclusion

The low power adiabatic 180° pulses used in conjunction with the bipolar spin echo crusher gradient pulses provide a rapid ^{13}C diffusion preparation strategy which was validated on clinical hardware. This sequence provided high diffusion attenuation with scan times much less than 1 s. An acquisition such as this could enable diffusion weighted imaging in a clinical setting.

Chapter 7

Clinical Translation

7.1 Abstract

This first-in-man imaging study evaluated the safety and feasibility of hyperpolarized [1-^{13}C]pyruvate as an agent for noninvasively characterizing alterations in tumor metabolism for patients with prostate cancer. Imaging living systems with hyperpolarized agents can result in more than 10,000-fold enhancement in signal relative to conventional magnetic resonance (MR) imaging. When combined with the rapid acquisition of in vivo ^{13}C MR data, it is possible to evaluate the distribution of agents such as [1-^{13}C]pyruvate and its metabolic products lactate, alanine, and bicarbonate in a matter of seconds. Preclinical studies in cancer models have detected elevated levels of hyperpolarized [1-^{13}C]lactate in tumor, with the ratio of [1-^{13}C]lactate/[1-^{13}C]pyruvate being increased in high-grade tumors and decreased after successful treatment. Translation of this technology into humans was achieved by modifying the instrument that generates the hyperpolarized agent, constructing specialized radio frequency coils to detect ^{13}C nuclei, and developing new pulse sequences to efficiently capture the signal. The study population comprised patients with biopsy-proven prostate cancer, with 31 subjects being injected with hyperpolarized [1-^{13}C]pyruvate.

The median time to deliver the agent was 66 s, and uptake was observed about 20 s after injection. No dose-limiting toxicities were observed, and the highest dose (0.43 ml/kg of 230 mM agent) gave the best signal-to-noise ratio for hyperpolarized [1-^{13}C]pyruvate. The results were extremely promising in not only confirming the safety of the agent but also showing elevated [1-^{13}C]lactate/[1-^{13}C]pyruvate in regions of biopsy-proven cancer. These findings will be valuable for noninvasive cancer diagnosis and treatment monitoring in future clinical trials.

7.2 Introduction

Prostate cancer is one of the most common cancers, with more than 200,000 new cases being reported annually in the United States [Siegel *et al.*, 2012]. Owing to increased screening using serum prostate-specific antigen (PSA) and extended-template transrectal ultrasound (TRUS)-guided biopsies, patients with prostate cancer are being identified at an earlier and potentially more treatable stage [Han *et al.*, 2003]. Once detected, the decision on how to manage prostate cancer poses a dilemma because there is a tremendous range in biologic diversity. They are treated with a broad spectrum of approaches from "active surveillance" to more aggressive surgical, radiation-based, and other focal therapies [Mcneal *et al.*, 1986; Cooperberg *et al.*, 2011]. Such therapies have trade-offs because, no matter how well they are delivered, there can be changes in health-related quality of life [Wei *et al.*, 2002]. In practice, many prostate cancers follow an indolent course that would not threaten the duration or quality of lives for the affected men, but the natural history of individual tumors is difficult to predict using currently available prognostic data [Johansson *et al.*, 2004c; Bill-Axelson *et al.*, 2008]. Conversely, between 22 and 35% of men presenting with clinically advanced prostate cancer, who are treated with what was thought to be definitive radiation or surgery, suffer a posttreatment biochemical recurrence [Mehta *et al.*, 2004]. The ability to predict outcome for individual patients and thereby select the most appropriate treatment is a

critically important, but so far unmet, clinical need.

Although noninvasive imaging is used to assess prostate cancer, conventional techniques have limited value for assessing prognosis, and there is no widely accepted modality that provides information about aggressiveness and response to therapy. Proton magnetic resonance spectroscopic imaging (^{1}H MRSI) has been applied to assess the metabolic properties of localized prostate cancer and, although it has shown clear advantages over anatomic imaging alone [Kurhanewicz and Vigneron, 2008], is limited by its relatively low spatial resolution and acquisition time, which is in the range of 10 to 20 min [Weinreb *et al.*, 2009]. ^{18}F-Fluorodeoxyglucose positron emission tomography provides information about increased glucose uptake and phosphorylation, but has been shown to in- adequately evaluate the presence and aggressiveness of prostate cancer because of both its relatively low uptake and collection in the bladder [Beauregard *et al.*, 2010].

Hyperpolarized ^{13}C MRI is a new molecular imaging technique with an unprecedented gain in signal intensity of 10,000- to 100,000-fold [Ardenkjær-Larsen *et al.*, 2003] that can be used to monitor uptake and metabolism of endogenous biomolecules [Golman *et al.*, 2003]. The magnitude of the increase in sensitivity depends on the degree of polarization that is achieved, the T_1 relaxation time of the ^{13}C agent, the delivery time, and the MR methods applied. Hyperpolarized agents are generated by mixing ^{13}C-labeled compounds with an electron paramagnetic agent (EPA), placing them in a 3.35-T magnetic field, cooling to $\sim$1 K, and using microwaves to transfer polarization from the electron spin of the EPA to the ^{13}C nuclei of the biomolecule (13). Once the polarization has reached the required level, the sample is rapidly dissolved with hot, sterile water and neutralized to physiological pH, temperature, and osmolarity. Intravenous injection of the hyperpolarized solution and observation using ^{13}C MR allow its delivery and metabolic products to be monitored [Golman *et al.*, 2006b]. The data must be obtained as rapidly as possible after dissolution because the enhancement decays at a rate determined by the T_1 relaxation time of the agent, which is about 60 s for [1-^{13}C]pyruvate at 3 T. Translation of hyperpolarized technology into human

subjects has been challenging because it requires specialized instrumentation to prepare the agent in a sterile environment, filter out the EPA, perform quality control (QC), and rapidly deliver samples to the patient.

The acquisition of ^{13}C data can be achieved using commercially available MR scanners in conjunction with specialized pulse sequences [Chen *et al.*, 2007] and radio frequency coils designed to transmit and receive at the appropriate frequency. Increased signal from hyperpolarized [1-^{13}C]lactate has been observed in preclinical models of prostate cancer relative to normal tissues, owing to both increased uptake of [1-^{13}C]pyruvate via monocarboxylate transporters 1 and 4 (MCT1 and MCT4) and increased expression of LDH-A and activity of lactate dehydrogenase (LDH) [Keshari *et al.*, 2013]. Levels of hyperpolarized [1-^{13}C]lactate and the flux of [1-^{13}C]pyruvate to [1-^{13}C]lactate increase with cancer progression (pathologic grade) [Albers *et al.*, 2008] and reduce after therapy [Dafni *et al.*, 2010].

The primary goal of this first-in-human study was to demonstrate the safety and feasibility of hyperpolarized [1-^{13}C]pyruvate injections in men with prostate cancer. After establishing the maximum of three dose levels that could be safely delivered, the secondary aims were to evaluate the kinetics of delivery to the prostate and assess differences in [1-^{13}C]lactate/[1-^{13}C]pyruvate for regions of cancer versus other tissues. Successfully demonstrating that the technology can be applied to humans provides the opportunity to use it for detecting and staging cancer, as well as detecting tumor progression and monitoring response to therapy.

7.3 Results

7.3.1 Study design: Doses delivered and data acquisition

There were 31 patients with untreated, biopsy-proven localized prostate cancer who received an injection of hyperpolarized [1-^{13}C]pyruvate. Their median age was 63 years (range, 45 to 75), median PSA was 5.9 ng/ml (range, 1.88 to 20.2), and median LDH was 141 IU/liter

(range, 109 to 261). Twenty-three of them had a diagnosis of Gleason grade 6 tumor, 6 had Gleason grade 7 tumor, and 2 had Gleason grade 8 tumor. The initial (phase 1) component of the study used a standard dose escalation design (Table 1), with six subjects being evaluated at each of three ascending doses. Dose levels were chosen on the basis of the range that had been shown to be safe in previous studies that did not include imaging but did inject nonlabeled pyruvate at the same concentrations, pH, and delivery rate (Supplementary Methods). At each dose, three patients were scanned with a dynamic ^{13}C sequence that provided localization to one-dimensional (1D) slices through the prostate, and three patients were scanned with a ^{13}C sequence that provided 2D or 3D spatial localization at a single time point. An additional 13 subjects were evaluated at the highest dose level in phase 2 with a mixture of dynamic and single-time point ^{13}C MR sequences. The specialized ^{13}C volume transmit coil and dual ^{1}H/^{13}C endorectal coil that were designed and built for this study are shown in Figure 7.1, A to C. These functioned well and allowed ^{1}H images and ^{13}C spectral data to be acquired from all subjects.

7.3.2 Hyperpolarized pyruvate polarization and delivery

For the 31 samples injected into patients, the average polarization was 17.8% (range, 15.9 to 21.1), pH was 7.6 (range, 7.3 to 8.0), temperature was 32.4°C (range, 28.8 to 36.4), and volume was 51.9 ml (range, 31.9 to 53.5). QC criteria were defined as follows: polarization to be not less than 15%, pH in the range of 6.7 to 8.0, sample temperature in the range of 25° to 37°C, and residual EPA concentration no higher than 3.0 mg. The mean times for getting the sample to the patient are seen schematically in Fig. 7.1D: the dissolution took an average of 17.8 s (range, 5 to 30), the QC process 13.1 s (range, 10 to 19), delivery through the hatch into the scan room 21.8 s (range, 11 to 30), and injection 14.9 s (range, 6 to 28). Overall, this gave an average of 67.6 s (range, 43 to 88) to deliver the agent to the subject. The parameters for individual patients are given in table S1. The mean injection volumes

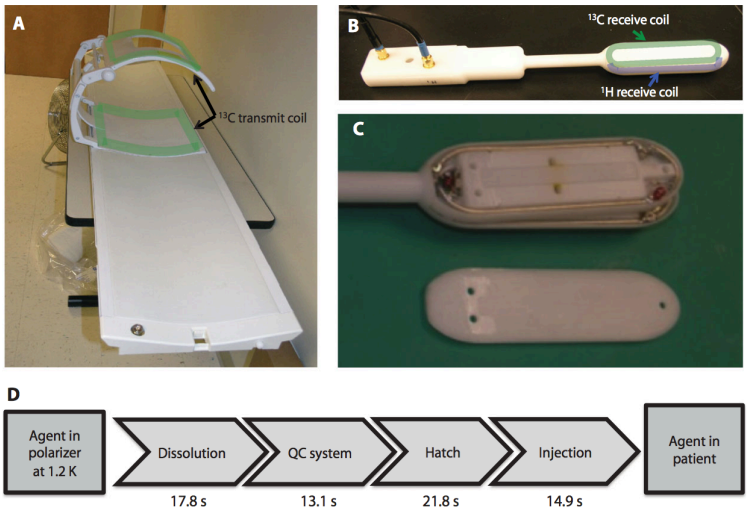

Figure 7.1: ^{13}C coil setup and the schematic steps for the delivery of hyperpolarized [1-^{13}C]pyruvate. (A to C) ^{13}C transmit coil (A) and endorectal ^{1}H/^{13}C receiver coil (B) used for acquiring data. The location of the coils is outlined on (A) and (B), with the layers inside the endorectal coil being seen in (C). The dimensions of the elements in the endorectal coil were 4 inches $\times$ 1 inches, with the total length of the coil being 12 inches. (D) Steps involved in transferring the hyperpolarized agent from the polarizer to the patient, and mean times required for each of them.

for the patients studied at each dose were 11.8 ml (range, 10 to 14), 26.8 ml (range, 22 to 33), and 34.5 ml (range, 29 to 46), with mean injection times of 8.5 s (range, 6 to 10), 14.8 s (range, 10 to 27), and 12.5 s (range, 1 to 28), respectively. Variation in injection times reflected differences in the volume delivered, as well as in the time for drawing the material from the drug product vessel into a syringe and performing the manual injection.

7.3.3 Patient toxicities

Vital signs were monitored before and immediately after the imaging examination, with subsequent telephone follow-ups over a period of 7 days to check for evidence of adverse events. In phase 1 of the study, there were a total of 10 adverse events in eight patients (table S2). These were all considered mild events and were classified as grade 1 by Common

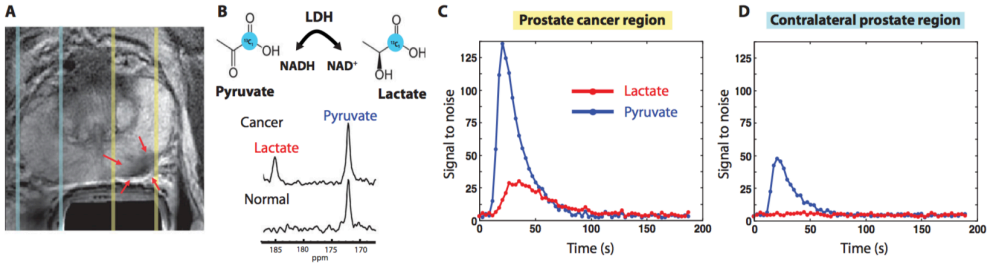

Figure 7.2: 1D ^{13}C dynamic MRSI data. Images are from a representative patient with a current PSA of 12.2 ng/ml, a small volume of biopsy-proven Gleason grade 4 + 3 prostate cancer in the left midgland, and who re- ceived the lowest dose (0.14 ml/kg) of hyperpolarized [1-^{13}C]pyruvate. (A) Axial T2-weighted image showing slices (dashed lines) obtained from 1D spectral localization. The slice that overlaps the left prostatic peripheral zone (right side of image) contained a small focus of reduced T2 signal intensity corresponding to the region of biopsy-proven cancer (red arrows). The slice overlapping the right peripheral zone (left side of image) contains only normal prostate tissue. (B) Flux of [1-^{13}C]pyruvate to [1-^{13}C]lactate catalyzed by LDH (top). Dynamic ^{13}C spectra were obtained from the same patient in (A) at 36 s after injection of hyperpolarized [1-^{13}C]pyruvate (bottom). The cancer spectrum demonstrated a lactate SNR of 25 owing to a high flux of hyperpolarized [1-^{13}C]pyruvate to [1-^{13}C]lactate. (C) Plot of 1D localized dynamic hyperpolarized pyruvate and lactate data from the slice that overlapped the region of prostate cancer. (D) Plot of 1D localized dynamic hyperpolarized pyruvate and lactate data from the slice that overlapped a contralateral region of the prostate.

Terminology Criteria for Adverse Events (CTCAE) v4.0.criteria (21). The highest dose of [1-^{13}C]pyruvate (0.43 ml/kg) was selected for further study on the basis of the higher signal-to-noise ratio (SNR) of hyperpolarized [1-^{13}C]pyruvate that was observed. In phase 2, there were an additional 10 events observed in five patients, but, again, none of them were considered to be dose-limiting toxicities (DLTs). The single episode of dizziness that was seen in one patient during phase 2 was attributed to extra dosing of atenolol, which was used by the subject to reduce anxiety rather than the hyperpolarized agent. There was one episode of grade 2 diarrhea reported in the phase 2 component, which was attributed to an enema that the patient received.

7.3.4 1D dynamic MRSI

The purpose of the 1D spatially localized dynamic data was to establish the time course of delivery of the agent. The acquisition provided spectra from an axial slab that covered the prostate and surrounding tissues and applied echo planar encoding from slices in the right-left direction at a 3-s time resolution. These dynamic data demonstrated reproducible delivery of hyperpolarized [1-^{13}C]pyruvate to the prostate and its conversion to hyperpolarized [1-^{13}C]lactate. Figure 7.2A shows a representative scan from a patient with PSA of 12.2 ng/ml, who had a small volume of biopsy-proven prostate cancer (Gleason grade 4 + 3) in the left midgland and received the lowest dose of 0.14 ml/kg. Representative ^{13}C spectra from the same patient taken from a slice including the tumor 36 s after injection demonstrated peaks corresponding to [1-^{13}C]pyruvate [173 parts per million (ppm)] and [1-^{13}C]lactate (185 ppm) (Fig. 7.2B). Spectra from the contralateral side of the prostate demonstrated only [1-^{13}C]pyruvate. A plot of spectral peak heights from the slice overlapping the tumor is shown in Fig. 7.2C and from the slice on the contralateral side of the gland in Fig. 7.2D. In both cases, [1-^{13}C]pyruvate arrived at about 20 s and reached a maximum at 24 s. [1-^{13}C]Lactate reached a maximum signal plateau at about 30 s after the end of injection.

For the patients who had unambiguous regions of tumor, the maximum SNRs of [1-^{13}C]pyruvate and [1-^{13}C]lactate in slices containing tumor were 101.3 (range, 31.6 to 192.1) and 19.5 (range, 12.5 to 33.5), respectively. Fitting the time course of changes in peak heights using a previously published two-compartment kinetic model [Zierhut *et al.*, 2010] resulted in an estimated mean T_1 of [1-^{13}C]pyruvate and [1-^{13}C]lactate of 29.2 ± 5 s and 25.2 ± 5 s (SD), respectively, and a mean [1-^{13}C]pyruvate to [1-^{13}C]lactate conversion rate constant of 0.013 ± 0.003 s^{-2} (SD) (range, 0.009 to 0.016).

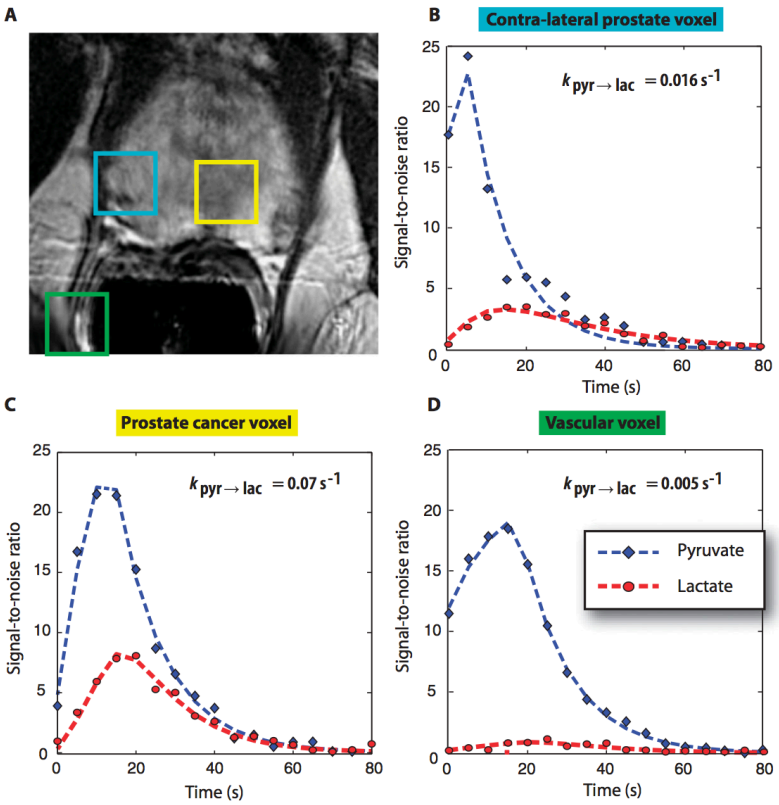

Figure 7.3: ^{13}C dynamic MRSI data. Images are from a representative patient with a current PSA of 3.6 ng/ml, who had biopsy-proven prostate cancer in the left apex (Gleason grade 3 + 4) and received the highest dose of hyperpolarized [1-^{13}C]pyruvate (0.43 ml/kg). (A) A focus of mild hypointensity can be seen on the T_2-weighted image, which was consistent with the biopsy findings. (B to D) 2D localized dynamic hyperpolarized [1-^{13}C]pyruvate and [1-^{13}C]lactate from spectral data that were acquired every 5 s from voxels overlapping the contralateral region of prostate (turquoise), a region of prostate cancer (yellow), and a vessel outside the prostate (green).

7.3.5 2D dynamic MRSI

A concern with the 1D localized dynamic MRSI data was that the contribution from hyperpolarized signals in tissues outside the prostate could confound the interpretation of estimated parameters. Therefore, five patients in phase 2 were studied with 2D spatially localized dynamic data. One of these patients had a PSA of 3.6 ng/ml and biopsy-proven prostate cancer in the left apex (Gleason grade 3 + 4) with an associated focus of reduced signal intensity on the anatomic images obtained during the MR staging examination (Fig. 7.3A). Hyperpolarized [1-^{13}C]pyruvate and [1-^{13}C]lactate from voxels in the prostate (Fig. 7.3B), the tumor (Fig. 7.3C), and a vessel outside the prostate (Fig. 7.3D) demonstrated a similar time course of delivery of the agent. There was increased conversion of [1-^{13}C]pyruvate to [1-^{13}C]lactate in the tumor (Fig. 7.3C), with the [1-^{13}C]pyruvate reaching a maximum by 18 $\pm$ 4 s and the [1-^{13}C]lactate reached a maximum at 27 $\pm$ 2 s after the start of acquisition, which was 5 s after the end of injection. After adjusting for additional delay, the timings of maximal signal are similar to those for the 1D dynamic data. Overall, the rate constant (mean $\pm$ SD) was 0.045 $\pm$ 0.025 s^{-1} for [1-^{13}C]pyruvate to [1-^{13}C]lactate in tumor voxels and 0.009 $\pm$ 0.003 s^{-1} for voxels coming from regions that included blood vessels.

7.3.6 Single-time point MRSI

The purpose of the single-time point spatially localized data was to compare the relative levels of [1-^{13}C]lactate and [1-^{13}C]pyruvate in regions of tumor versus normal prostate and surrounding tissue. For the phase 1 study, the MRSI acquisitions were initially started at about 30 s after the end of the injection. The maximum SNR for [1-^{13}C]pyruvate peaks in the prostate for the three patients evaluated in phase 1 with single-time point spatially localized MRSI doses of 0.14, 0.28, and 0.43 ml/kg were in the range of 4.5 to 8.4, 6.5 to 10.6, and 14.3 to 25.4, respectively. Hence, although [1-^{13}C]lactate peaks were observed in tumor voxels at the two lower doses, the higher levels of [1-^{13}C]pyruvate at 0.43 ml/kg allowed for a more

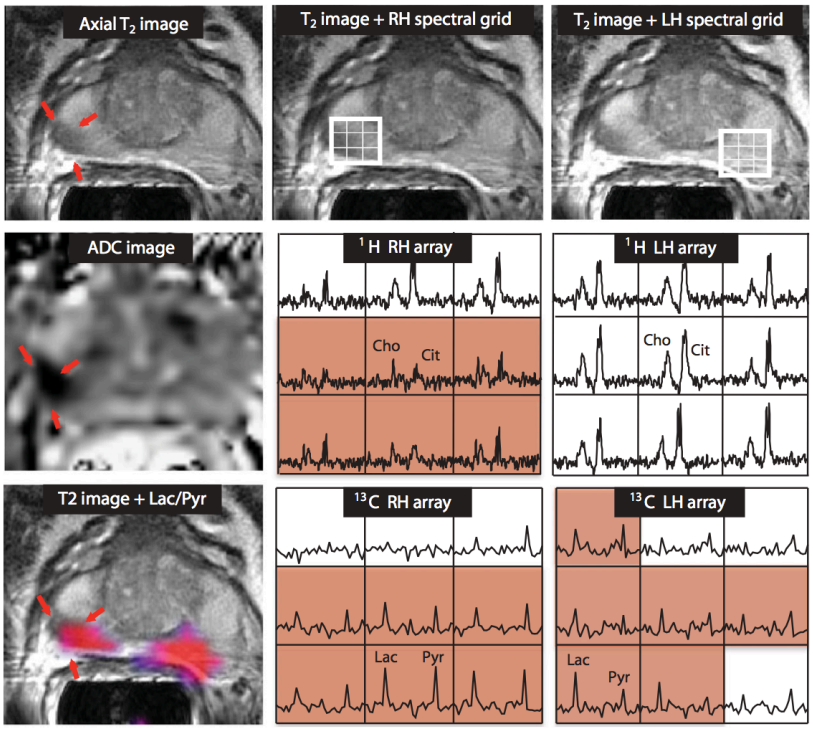

Figure 7.4: 2D single-time point MRSI data. Images were obtained from a patient with serum PSA of 9.5 ng/ml, who was diagnosed with bilateral biopsy-proven Gleason grade 3 + 3 prostate cancer and received the highest dose of hyperpolarized [1-^{13}C]pyruvate (0.43 ml/kg). The axial T_2-weighted image shows a unilateral region of reduced signal intensity (red arrows), which is consistent with a reduction in the corresponding ADC. The ^{1}H spectral arrays supported these findings, with voxels with reduced citrate and elevated choline/citrate (highlighted in pink) on the right side of the gland and voxels with normal metabolite ratios on the left side. The ^{13}C spectral arrays show voxels with elevated levels of hyperpolarized [1-^{13}C]lactate/[1-^{13}C]pyruvate (highlighted in pink) on both the right and left sides of the prostate. The location of colored regions in the metabolite image overlay had a ratio of [1-^{13}C]lactate/[1-^{13}C]pyruvate greater than or equal to 0.6.

reliable estimate of the ratio of [1-^{13}C]lactate/[1-^{13}C]pyruvate. In the following discussion on variations in this ratio in the prostate gland, we focus on the results from single-time point MRSI data that were obtained at the highest dose during phases 1 and 2 of the study.

Representative 2D MRSI data are shown in Fig. 7.4. The patient had a serum PSA of 9.5 ng/ml and bilateral biopsy-proven Gleason grade 3 + 3 prostate cancer. The T_2 images, apparent diffusion coefficient (ADC) images, and ^{1}H spectra from the staging examination demonstrated an abnormal lesion, but only on the right side of the gland (Fig. 7.4). The ^{13}C spectra were acquired from 33 to 45 s after the end of the injection, and the corresponding [1-^{13}C]lactate/[1-^{13}C]pyruvate image overlay, which highlights in color regions with a ratio of more than 0.6, demonstrated bilateral areas of hyperpolarized [1-^{13}C]lactate. The median [1-^{13}C]lactate/[1-^{13}C]pyruvate ratios were 0.94 (range, 0.85 to 1.25) on the right side and 1.35 (range, 0.73 to 4.39) on the left side of the gland. The median [1-^{13}C]lactate/[1-^{13}C]pyruvate ratio in a region of the central gland - which was not thought to include tumor - was 0.45 (range, 0.31 to 0.49). The median SNRs of [1-^{13}C]lactate in the right and left regions of suspected tumor were 7.6 and 6.7, with the corresponding median SNRs of [1-^{13}C]pyruvate being 7.8 and 5.4, respectively. MR-guided biopsy that was performed subsequent to the ^{13}C study confirmed the presence of bilateral cancer corresponding to these abnormalities, with Gleason grade 3 + 4 on the right and Gleason grade 3 + 3 with high-grade prostatic intraepithelial neoplasia on the left side of the gland. The fact that the hyperpolarized imaging method was able to detect bilateral cancer, whereas conventional anatomic imaging methods were only able to visualize unilateral cancer, is an exciting finding, which may be especially important in monitoring patients like this who are thought to have slow-growing cancers and are being followed with active surveillance before starting treatment.

One concern in interpreting the data from the patient in Fig. 7.4 was that the SNR of the [1-^{13}C]pyruvate peak was relatively low in some voxels, making it difficult to obtain an accurate estimate of the ratio of [1-^{13}C]lactate/[1-^{13}C]pyruvate for tumor versus normal tissue. For this reason, subsequent data sets were obtained starting at the earlier time of 25 s

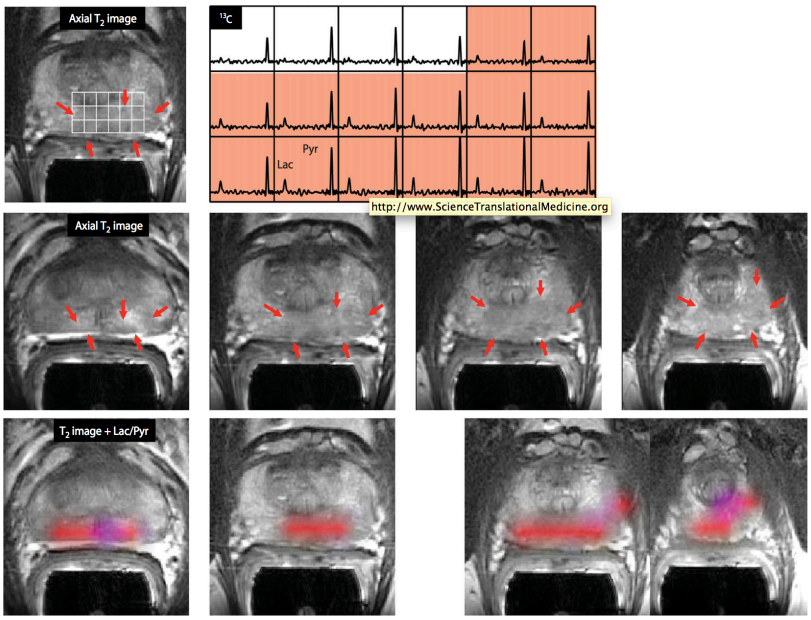

Figure 7.5: 3D single-time point localized MRSI data. Images were obtained from patient A in Table 2, who had a serum PSA of 4.5 ng/ml, was originally diagnosed with bilateral biopsy-proven Gleason grade $3 + 3$ prostate cancer, and received the highest dose of hyperpolarized [1-^{13}C]pyruvate (0.43 ml/kg). The upper panel shows an axial T_2-weighted images and corresponding spectral array with the area of putative tumor highlighted by pink shading. A region of tumor was observed on the T_2-weighted images (red arrows), as well as on ADC images and ^{1}H MRSI data. A region of relatively high hyperpolarized [1-^{13}C]lactate was observed in the same location as the abnormalities that had been observed on the multiparametric ^{1}H staging exam. The lower panels show axial T_2 images with and without metabolite overlays for different axial slices from the same patient. The colored regions in these overlays have a ratio of [1-^{13}C]lactate/[1-^{13}C]pyruvate ≥ 0.2. These demonstrated a large volume of bilateral cancer.

after the end of injection rather than at 33 s. For data acquired in this time window, peaks of [1-^{13}C]pyruvate were observed in most of the gland, and the criteria used to define regions of suspected tumor within the prostate gland were an SNR of [1-^{13}C]pyruvate >10.0, a clearly visualized peak corresponding to [1-^{13}C]lactate peak with an $SNR > 3.0$, and the ratio of the peak heights of 0.2 or higher. An example of 3D localized ^{13}C MRSI data acquired and evaluated in this manner is seen in Fig. 7.5. The results from the corresponding MR staging examination are shown in fig. S1. This patient (patient A in Table 2) had serum PSA of 4.5 ng/ml and a diagnosis of bilateral biopsy-proven Gleason grade 3 + 3 cancer. The ^{13}C spectral data showed large peaks corresponding to [1-^{13}C]pyruvate throughout the spectral grid with lower, but still clearly detected, [1-^{13}C]lactate peaks in the highlighted region. The median estimates for levels of [1-^{13}C]pyruvate, [1-^{13}C]lactate, and [1-^{13}C]lactate/[1-^{13}C]pyruvate for tumor voxels identified on multiple slices as being tumor were 41.0, 13.6, and 0.28, respectively. The color metabolite overlays highlight regions with [1-^{13}C]lactate/[1-^{13}C]pyruvate that were higher than the cutoff value on multiple slices. The patient had a follow-up MR-guided biopsy that demonstrated that the lesion had progressed to Gleason 3 + 4 prostate cancer.

Results from three other patients who had areas of elevated [1-^{13}C]lactate/[1-^{13}C]pyruvate are shown in Fig. 7.6. The same acquisition timing was used to obtain the MRSI data and the same cutoff criteria applied to define voxels with abnormal metabolite ratios as for patient A. For two of the cases (patients B and D), bilateral regions of suspected tumor were identified, and for the third case, there was a unilateral focus of suspected tumor. The median ratios of [1-^{13}C]lactate/[1-^{13}C]pyruvate ranged from 0.28 to 0.38, the median SNR for [1-^{13}C]lactate ranged from 4.8 to 8.4, and the median SNR for [1-^{13}C]pyruvate ranged from 13.5 to 30.0. The locations highlighted in color on the metabolite overlay images were consistent either with the original biopsies from these patients or with abnormalities that were identified in the images from their MR staging examinations.

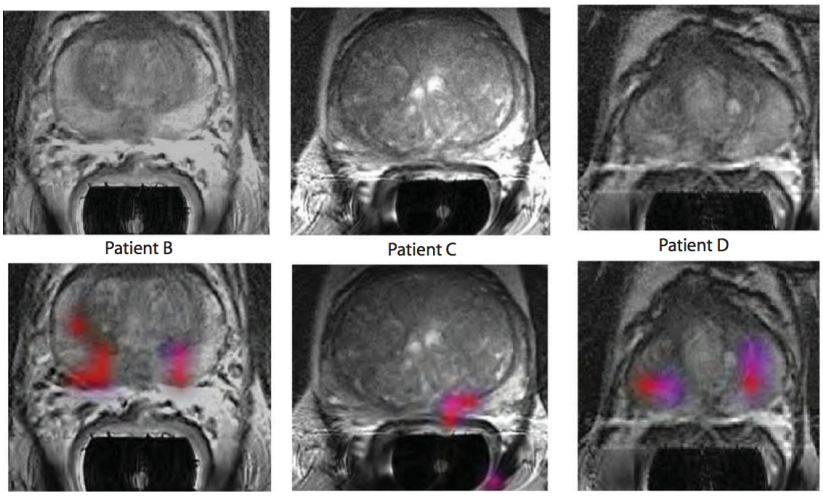

Figure 7.6: Further representative examples of 3D single-time point MRSI data. The axial T2-weighted images and overlays of hyperpolarized [1-^{13}C]lactate/[1-^{13}C]pyruvate are from the three patients labeled as B to D in Table 2. All three of the patients had biopsy-proven Gleason grade 3 + 3 prostate cancer and received the highest dose of hyperpolarized [1-^{13}C]pyruvate (0.43 ml/kg). Patient B had a current PSA of 5.1 ng/ml, patient C had a PSA of 9.8 ng/ml, and patient D had a PSA of 1.9 ng/ml. The SNR and metabolite ratios in the regions highlighted in color on the image overlays are given in Table 2.

7.4 Discussion

First-in-man metabolic imaging with hyperpolarized [1-^{13}C]pyruvate was successfully applied in 31 patients with prostate cancer. There were no DLTs observed, and the highest dose, namely, 230 mM [1-^{13}C]pyruvate (0.43 ml/kg), was selected for evaluation of different MR data acquisition strategies in phase 2 of the study. The prototype polarizer and QC procedures used to prepare the hyperpolarized agent were complex, and the fact that 31 of 33 preparations were successful in producing material that was injected into the patients is encouraging. Future studies would benefit from the development of more robust and automated procedures for generating and preparing the hyperpolarized agent for human use. An improved system that can simultaneously polarize four samples and uses a disposable fluid path has been designed [Ardenkjær-Larsen *et al.*, 2011] and tested in preclinical studies [Hu *et al.*, 2013]. It is anticipated that clinical studies will take advantage of such technology to provide higher polarizations and faster agent delivery.

The kinetics of delivering the hyperpolarized agent and the increase in [1-^{13}C]lactate signal were consistent with those observed in preclinical models. The 1D dynamic MRSI data obtained in our study showed higher [1-^{13}C]lactate signal in slices including tumor, but also contained some signal from tissues outside of the prostate. The [1-^{13}C]lactate signal was low or undetectable in slices from regions of the prostate that did not include tumor. This agrees with previous patient prostate biopsy studies, which demonstrated very low lactate concentrations (30), and with preclinical studies, which demonstrated a low flux of hyperpolarized [1-^{13}C]pyruvate to lactate in normal prostate (17). The 2D dynamic MRSI data were able to distinguish signals from tumor and vessels, with the rate of [1-^{13}C]pyruvate to [1-^{13}C]lactate conversion being four to five times higher in tumor. This is consistent with the increased expression of MCT1, MCT4, and LDH-A, and increased activity of LDH in the tumor that was observed in pre- clinical studies [Keshari *et al.*, 2013; Albers *et al.*, 2008].

The 2D and 3D single-time point MRSI data had excellent SNRs and spectral quality. These data sets were acquired in 8 to 12 s and accurately reflected the presence, location, and size of cancer relative to surrounding healthy prostate tissues. Moving to the earlier spectral acquisition window of 25 s after injection, for the patients shown in Figs. 5 and 6, yielded higher hyperpolarized [1-^{13}C]pyruvate signals and more readily quantifiable [1-^{13}C]lactate/[1-^{13}C]pyruvate ratios (Table 2) than for the patient shown in Fig. 4. The marked changes in hyperpolarized [1-^{13}C]pyruvate signal with time and differences in kinetics suggest that the acquisition of spatially localized dynamic MR data is a promising approach for comparing metabolic parameters for tumor versus normal tissue.

Patients who participated in phase 2 of the study and who had regions of ab- normal signal on their previous multiparametric MR screening examinations also had elevated [1-^{13}C]lactate/[1-^{13}C]pyruvate relative to signals from normal prostate. In Fig. 4, our hyperpolarized imaging method highlighted a region of biopsy-proven tumor that was not observed during the staging examination; this is important because it shows the power of using more advanced technologies for characterizing tissues that appear normal on conventional anatomic images. There were two other subjects with findings of abnormal [1-^{13}C]lactate/[1-^{13}C]pyruvate in regions where the anatomic imaging was uncertain, but in those cases, no direct biopsy evidence was available to confirm that they corresponded to tumor.

There are several limitations of our study because it is first in human. Although ^{13}C data acquisition parameters had been investigated in phantom and preclinical studies, it was not possible to choose the most appropriate values without having results from human subjects. This led to adjustments in the timing parameters and spatial resolution being made during the course of the study. Although this did not influence the goals of phase 1 of the study, which were to establish the safety and feasibility of using hyperpolarized [1-^{13}C]pyruvate in humans, it did mean that the more detailed analysis of data was restricted to subjects participating in phase 2. Another limitation was that the population chosen for the study had relatively early-stage cancer, and it was not always possible to make exact correlations

between the imaging findings and pathologic findings. The choice of patients with early-stage disease who were on active surveillance was driven by the need to avoid complications in data interpretation associated with previous treatment and to have plenty of time to recruit and monitor them during a period when they were expected to have stable disease. Evidence from preclinical studies has shown that the magnitude of [1-^{13}C]lactate/[1-^{13}C]pyruvate increases with tumor grade [Albers *et al.*, 2008], and so we believe that our technology will be even more sensitive for evaluating patients with advanced and aggressive cancers.

When combined with findings from preclinical studies, the results of this first-in-man study suggest that hyperpolarized ^{13}C metabolic imaging may be valuable for initial diagnosis and for monitoring therapy. In addition to improved technology for generating and delivering hyperpolarized agents becoming available [Ardenkjær-Larsen *et al.*, 2011], designing new MR data acquisition sequences that use compressed sensing [Larson *et al.*, 2011], parallel imaging strategies, and multichannel ^{13}C radio frequency coils will help in translating these methods into the clinic. These developments will allow similar methods to be applied to more diverse populations of cancer patients who are undergoing surgical resection or image-directed biopsy. In addition to having the potential for more accurate diagnosis and staging, there have been a large number of studies using hyperpolarized agents in preclinical models of lymphoma, prostate, brain, liver, breast, and bone cancers. Other disease models that have been studied and show promise for translation to humans are cardiac disease and arthritis.

Chapter 8

Conclusion

8.1 Summary of Findings

This thesis presented several noteworthy findings in the field of hyperpolarized ^{13}C magnetic resonance imaging. In chapter 3 we showed that the liquid state T_2 of [^{13}C,^{15} N$_2$]urea was over 200 times greater than that of [^{13}C]urea, thus enabling projection angiography at sub-millimeter resolution using an endogenous contrast agent on a clinical scanner. This study also presented the first *in vivo* method for T_2 mapping of hyperpolarized ^{13}C compounds. Very large T_2 changes were observed in the kidney with both [^{13}C]urea and [^{13}C,^{15} N$_2$]urea. The T_2 of [^{13}C]urea was found to decrease slightly in the kidney compared to the vasculature, while [^{13}C,^{15} N$_2$]urea showed a very large T_2 increase within the kidney. This difference was attributed to the differential correlation time dependence of each isotope due to the scalar coupling of the second kind relaxation pathway which strongly attenuates the T_2 of [^{13}C]urea.

The long intra-renal signal component T_2 of [^{13}C,^{15} N$_2$]urea was explored in more depth in Chapter 4. The T_2 increase was shown to report directly on glomerular filtration thus enabling for the first time direct differentiation of the vascular and renal tubular signal components. Urea T_2 mapping showed differential contrast in antidiuresis and diuresis states

thus providing a method for non-invasive, millimeter resolution monitoring of the urea transporters UT-A1 and UT-A3. Finally, a 3D steady state free precession (SSFP) sequence was developed to utilize the long T_2 of the tubular urea signal were utilized for the encoding (1.2 mm)^3 resolution images of the urea within the kidney.

Chapters 5 and 6 focused on the development of echo planar imaging (EPI) methods for rapid ^{13}C imaging. Chapter 5 developed a simultaneous EPI method for encoding [1-^{13}C]pyruvate and [1-^{13}C]lactate. This study also presented a preliminary signal optimization model for apply differential flip angles on exchanging spins. Chapter 6 developed a spin echo preparation sequence for generating single shot diffusion-weighted images. Low power adiabatic RF pulses were developed for compatibility with current clinical ^{13}C transmitter coils, and magnetostatic simulations were used to estimate the field of view over which these pulses were expected to perform. A bipolar diffusion preparation offered b values of ~ 1000 s/mm^2 and echo times less than 200 ms.

Finally, the first hyperpolarized ^{13}C in-man clinical trial is presented in 7. This study showed the first direct detection of pyruvate metabolism in human subjects, and differential contrast in tumor regions showed promise for the use of hyperpolarized magnetic resonance imaging as a method for detection and staging of prostate cancer as well as a possible disease monitoring tool for the growing percentage of patients electing active surveillance.

8.2 Future Directions

Several of the methods presented in this work are under further development at UCSF. The extremely short TR possible with preclinical imaging systems can be utilized for full 3D encoding of 1 mm^3 isotropic resolution hyperpolarized ^{13}C images. Figure 8.1 shows an example of this high resolution [^{13}C,^{15}N$_2$]urea imaging in mice. This imaging strategy is currently being explored as a method for perfusion evaluation in nephropathy models. This is clinically significant since Gd-based MRI contrast are contraindicated for patients with

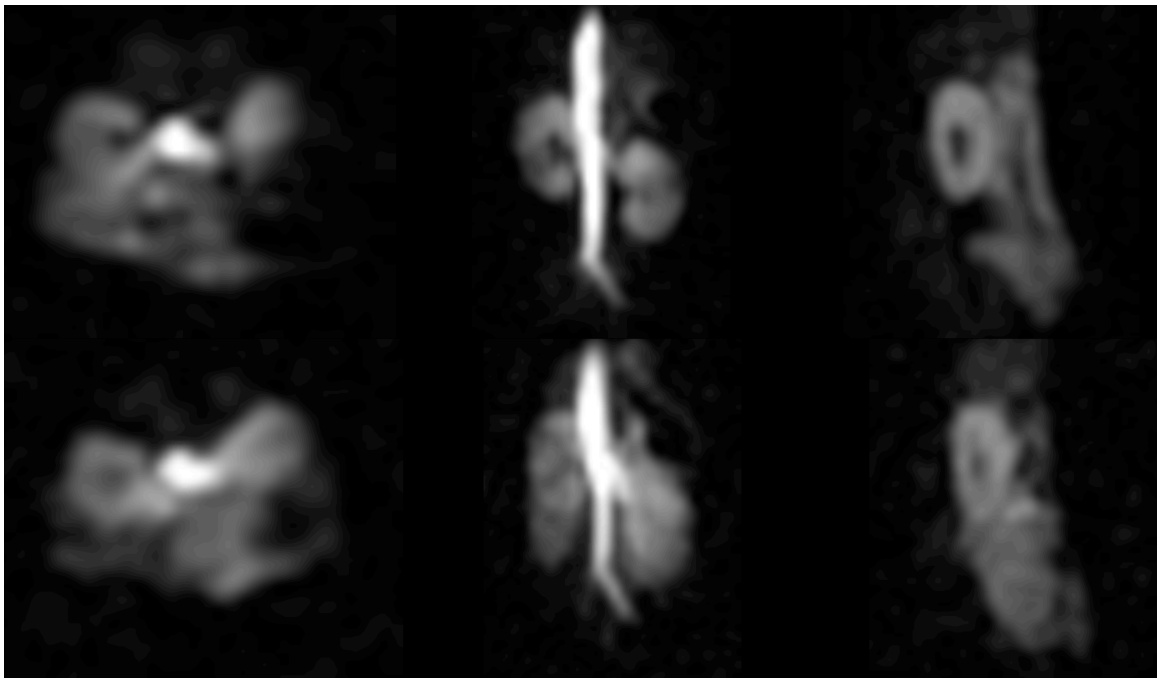

Figure 8.1: Axial (left), coronal (center), and sagittal (right) 1 mm^3 isotropic resolution of hyperpolarized [^{13}C,^{15}N$_2$]urea in two mice acquired at 14.1 T. The bottom images are in a transgenic mouse model with necrosis of the renal peri-tubular vasculature. The top images were acquired in a normal mouse. Diffuse urea uptake in the regions surrounding the kidney (bottom, center) could indicate the potential utility of monitoring altered perfusion with the high resolution imaging strategies presented in Chapters 3 and 4 .

renal dysfunction. However, urea has been proven to be tolerated in high doses even in patients with end stage renal failure

Other possible future applications for urea renography include the perfusion assessment of renal carcinoma patients after cryoablation since many of these subjects are unable to receive Gd contrast. Hyperpolarized urea could be utilized for imaging renal artery stenosis, which is a common source of renovascular hypertension. Furthermore, urea renography could provide a radiation-free imaging method for assessing congenital renal disorders in children.

The diffusion weighted spin echo EPI sequence presented in Chapter 6 is currently being studied as a method for *in vivo* hyperpolarized ^{13}C apparent diffusion coefficient (ADC) map-

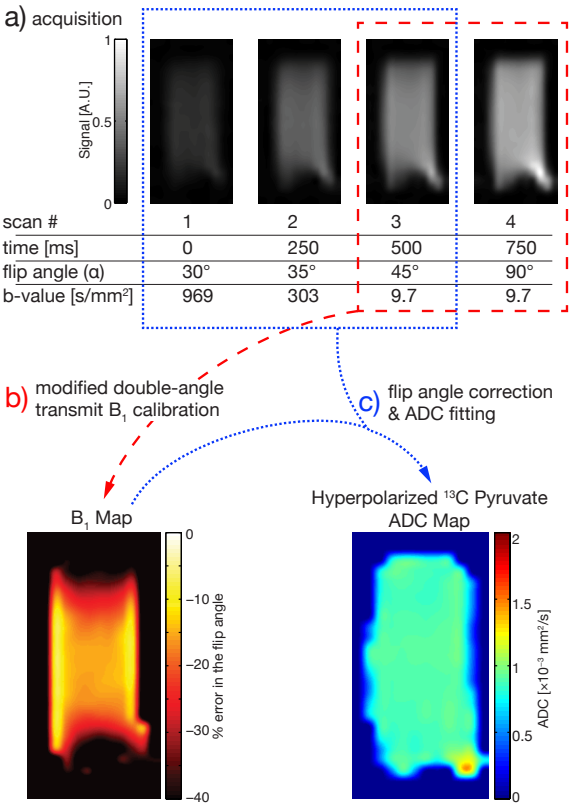

Figure 8.2: A method for hyperpolarized ^{13}C apparent diffusion coefficient (ADC) mapping based on the spin echo EPI sequence described in Chapter 6. The fast EPI readout is utilized for the acquisition of multiple b value images over a time scale short compared to T_1. Furthermore, since the residual M_z changes after each excitation, a novel built-in B_1 calibration is performed using the final 2 acquisitions. This estimated flip angle is then utilized for the correction of the diffusion-weighted images to improve ADC estimation accuracy.

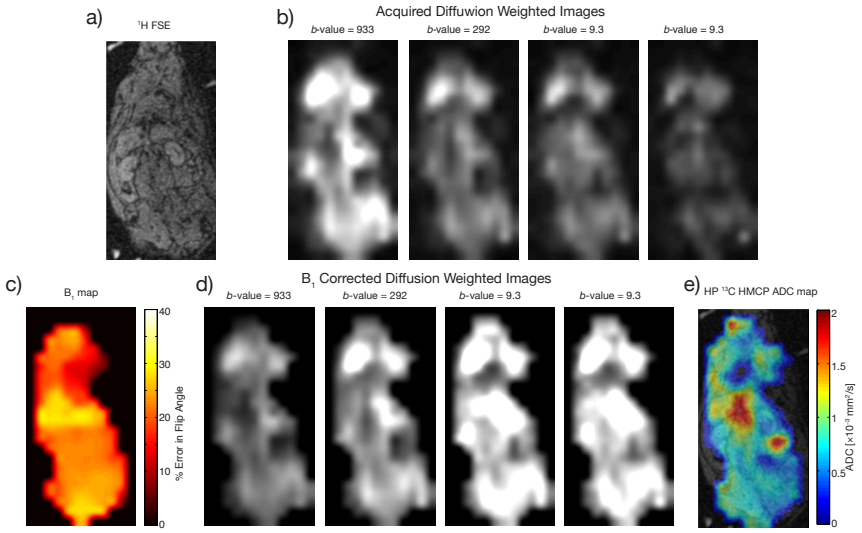

Figure 8.3: Hyperpolarized ^{13}C ADC mapping using the method shown in Figure 8.2. a) ^{1}H localizer. b) ^{13}C HMCP images acquired with various b values. c) Flip angle map. d) Flip angle corrected ^{13}C images. e) ADC map. This image represents the first hyperpolarized ^{13}C ADC map acquired on a clinical system using clinical transmitter and gradient hardware.

ping. The ADC of many common hyperpolarized ^{13}C molecular probes have been measured in aqueous solution [Koelsch *et al.*, 2013]. However, *in vivo* ADC values of hyperpolarized ^{13}C compounds are still unknown. Furthermore, since early studies have shown increased contrast-to-noise with the use of high diffusion weighting [Larson *et al.*, 2012], the determination of *in vivo* ADCs could yield novel image contrast and inform on cellularity and cell membrane transport. Figure 8.2 shows a schematic for this technique, and Figure 8.3 shows initial ADC maps. Using the spin echo EPI, this technique is directly translatable to clinical ^{13}C imaging studies. Potential future studies would study the correlation of hyperpolarized ^{13}C ADC values and tumor histology and transporter expression.

The T_2 mapping sequence described in Chapters 3 and 4 could provide an extremely powerful method for quantification of the ^{13}C signal. Chapter 4 presents only an initial utilization of the T_2 heterogeneity of ^{13}C compounds. However, prior single-voxel T_2 measurements showed significant contrast in tumor models [Yen *et al.*, 2010]. The SSFP T_2

mapping sequence would very likely be a useful tool for cancer imaging due to high SNR and spatial resolution. Both ADC and T_2 mapping are appealing for hyperpolarized compounds since they offer reliable imaging metrics which do not depend on absolute signal, and, therefore, are more immune to the inevitable variations of polarization and sample transport than SNR measurements.

Dynamic nuclear polarization of ^{13}C labeled compounds offers a unique and exciting potential for the monitoring of real-time metabolism. Although this enhancement is between 4 and 5 orders of magnitude above thermal polarization, image quality is still limited somewhat by the low γ of the ^{13}C nucleus and substantially by the mM concentrations of the contrast agent *in vivo*. Medical applications of ^{13}C imaging will require high resolution signal-to-noise-ratio, and contrast-to-noise ratio for diagnostic utility. Improved methods for meeting all of these requirements are presented in this thesis.

Bibliography

[Abragam, 1983] Anatole Abragam. *Principles of Nuclear Magnetism*. Oxford University Press, 1983.

[Albers *et al.*, 2008] Mark J Albers, Robert Bok, Albert P Chen, Charles H Cunningham, Matt L Zierhut, Vickie Yi Zhang, Susan J Kohler, James Tropp, Ralph E Hurd, Yi-Fen Yen, Sarah J Nelson, Daniel B Vigneron, and John Kurhanewicz. Hyperpolarized ^{13}C lactate, pyruvate, and alanine: noninvasive biomarkers for prostate cancer detection and grading. *Cancer Res*, 68(20):8607–15, 2008.

[Anderson *et al.*, 1930] Arthur K. Anderson, Hannah E. Honeywell, Albert C. Santy, and Svend Pedersen. The composition of normal rat blood. *J Biol Chem*, 86(1):157–160, 1930.

[Ardenkjær-Larsen *et al.*, 2003] Jan H Ardenkjær-Larsen, Björn Fridlund, Andreas Gram, Georg Hansson, Lennart Hansson, Mathilde H Lerche, Rolf Servin, Mikkel Thaning, and Klaes Golman. Increase in signal-to-noise ratio of $>$ 10,000 times in liquid-state NMR. *Proc Natl Acad Sci U S A*, 100(18):10158–63, Sep 2003.

[Ardenkjær-Larsen *et al.*, 2009] Jan H Ardenkjær-Larsen, S Macholl, and H Johannesson. Dynamic nuclear polarization with trityls at 1.2 K. *Appl Magn Reson*, 34:509–522, 2009.

[Ardenkjær-Larsen *et al.*, 2011] Jan H. Ardenkjær-Larsen, Andrew M. Leach, Neil Clarke, John Urbahn, Denise Anderson, and Timothy W. Skloss. Dynamic nuclear polarization polarizer for sterile use intent. *NMR Biomed*, 24(8):927–932, 2011.

[Beauregard *et al.*, 2010] J. M. Beauregard, S. G. Williams, T. R. DeGrado, P. Roselt, and R. J. Hicks. Pilot comparison of ^{18}F-fluorocholine and ^{18}F-fluorodeoxyglucose PET/CT with conventional imaging in prostate cancer. *J Med Imaging Radiat Oncol*, 54(4):325–332, 2010.

[Bhattacharya *et al.*, 2005] P. Bhattacharya, K. Harris, A.P. Lin, M. Mansson, V.A. Norton, W.H. Perman, D.P. Weitekamp, and B.D. Ross. Ultra-fast three dimensional imaging of hyperpolarized ^{13}C in vivo. *MAGMA*, 18:245–256, 2005.

[Bill-Axelson *et al.*, 2008] Anna Bill-Axelson, Lars Holmberg, Frej Filen, Mirja Ruutu, Hans Garmo, Christer Busch, Stig Nordling, Michael Hggman, Swen-Olof Andersson, Stefan Bratell, Anders Spangberg, Juni Palmgren, Hans-Olov Adami, Jan-Erik Johansson, and for the Scandinavian Prostate Cancer Group Study Number 4. Radical prostatectomy versus watchful waiting in localized prostate cancer: the scandinavian prostate cancer group-4 randomized trial. *J Natl Cancer Inst*, 100(16):1144–1154, 2008.

[Bloch, 1946] F. Bloch. Nuclear induction. *Phys Rev*, 70(7):460–473, 1946.

[Bloembergen *et al.*, 1948] N. Bloembergen, E. M. Purcell, and R. V. Pound. Relaxation effects in nuclear magnetic resonance absorption. *Phys Rev*, 73(7):679–712, 1948.

[Braham, 1983] J. Braham. Urea permeability of human red cells. *J Gen Physiol*, 82:1–23, 1983.

[Brindle *et al.*, 2011] Kevin M. Brindle, Sarah E. Bohndiek, Ferdia A. Gallagher, and Mikko I. Kettunen. Tumor imaging using hyperpolarized ^{13}C magnetic resonance spectroscopy. *Magn Reson Med*, 66(2):505–519, 2011.

[Carr and Purcell, 1954] H. Y. Carr and E. M. Purcell. Effects of diffusion on free precession in nuclear magnetic resonance experiments. *Phys Rev*, 94:630–638, 1954.

[Chen *et al.*, 2007] Albert P. Chen, M. J. Albers, C. H. Cunningham, Susan J. Kohler, Yi-Fen Yen, Ralph E. Hurd, James Tropp, Robert Bok, John M. Pauly, S. J. Nelson, John Kurhanewicz, and Daniel B. Vigneron. Hyperpolarized C-13 spectroscopic imaging of the TRAMP mouse at 3T-initial experience. *Magn Reson Med*, 58:1099–1106, 2007.

[Cheng, 2008] Nian-Sheng Cheng. Formula for the viscosity of a glycerol-water mixture. *Ind Eng Chem Res*, 47(9):3285–3288, 2008.

[Chiavazza *et al.*, 2013] Enrico Chiavazza, Eugen Kubala, Concetta V. Gringeri, Stephan Duwel, Markus Durst, Rolf F. Schulte, and Marion I. Menzel. Earth's magnetic field enabled scalar coupling relaxation of ^{13}C nuclei bound to fast-relaxing quadrupolar ^{14}N in amide groups. *J Magn Reson*, 227(0):35 – 38, 2013.

[Chubar *et al.*, 1998] Oleg Chubar, Pascal Elleaume, and Joel Chavanne. A three-dimensional magnetostatics computer code for insertion devices. *J Synchrotron Rad*, 5(3):481–484, 1998.

[Collins and Wang, 2011] Christopher M. Collins and Zhangwei Wang. Calculation of radiofrequency electromagnetic fields and their effects in MRI of human subjects. *Magn Reson Med*, 65(5):1470–1482, 2011.

[Conolly *et al.*, 1988] S. M. Conolly, D. G. Nishimura, A. Macovski, and G. H. Glover. Variable-rate selective excitation. *J Magn Reson*, 78(3):440–458, 1988.

[Cooperberg *et al.*, 2011] Matthew R. Cooperberg, Peter R. Carroll, and Laurence Klotz. Active surveillance for prostate cancer: Progress and promise. *J Clin Oncol*, 29(27):3669–3676, 2011.

[Cunningham *et al.*, 2007] C. H. Cunningham, Albert P. Chen, M. J. Albers, John Kurhanewicz, Yi-Fen Yen, Ralph E. Hurd, John M. Pauly, S. J. Nelson, and Daniel B. Vigneron. Double spin-echo sequence for rapid spectroscopic imaging of hyperpolarized ^{13}C. *J Magn Reson*, 187(2):357–362, 2007.

[Cunningham *et al.*, 2008] Charles H Cunningham, Albert P Chen, Michael Lustig, Brian A Hargreaves, Janine Lupo, Duan Xu, John Kurhanewicz, Ralph E Hurd, John M Pauly, Sarah J Nelson, and Daniel B Vigneron. Pulse sequence for dynamic volumetric imaging of hyperpolarized metabolic products. *J Magn Reson*, 193(1):139–46, Jul 2008.

[Dafni *et al.*, 2002] H. Dafni, L. Landstrom, B. Schlechter, F. Kohen, and M. Neeman. MRI and fluorescence microscopy of the acute vascular response to VEGF165: vasodilation, hyperpermeability and lymphatic uptake, followed by rapid inactivation of the growth factor. *NMR Biomed*, 15:120–131, 2002.

[Dafni *et al.*, 2010] Hagit Dafni, Peder E.Z. Larson, Simon Hu, Hikari A.I. Yoshihara, Christopher S. Ward, Humsa S. Venkatesh, Chunsheng Wang, Xiaoliang Zhang, Daniel B. Vigneron, and Sabrina M. Ronen. Hyperpolarized ^{13}C spectroscopic imaging informs on hypoxia-inducible factor-1 and Myc activity downstream of platelet-derived growth factor receptor. *Cancer Res*, 70(19):7400–7410, 2010.

[Deppe and Wild, 2012] Martin H. Deppe and Jim M. Wild. Variable flip angle schedules in bSSFP imaging of hyperpolarized noble gases. *Magn Reson Med*, 67(6):1656–1664, 2012.

[Feinberg and Oshio, 1994] D A Feinberg and K Oshio. Phase errors in multi-shot echo planar imaging. *Magn Reson Med*, 32(4):535–9, Oct 1994.

[Finer *et al.*, 1972] E. G. Finer, F. Franks, and M. J. Tait. Nuclear magnetic resonance studies of aqueous urea solutions. *J Amer Chem Soc*, 94(13):4424–4429, 1972.

[Finkelstein, 1976] A. Finkelstein. Water and nonelectrolyte permeability of lipid bilayer membranes. *J Gen Physiol*, 68:127–135, 1976.

[Gardner and Scott, 1980] M. D. Gardner and R. Scott. Age- and sex-related reference ranges for eight plasma constituents derived from randomly selected adults in a Scottish new town. *J Clin Pathol*, 33:380–385, 1980.

[Golman *et al.*, 2003] Klaes Golman, Jan H. Ardenkjær-Larsen, J. Stefan Petersson, Sven Mansson, and Ib Leunbach. Molecular imaging with endogenous substances. *Proc Natl Acad Sci U S A*, 100(18):10435–10439, 2003.

[Golman *et al.*, 2006a] Klaes Golman, René Zandt, Mathilde Lerche, Rikard Pehrson, and Jan Henrik Ardenkjær-Larsen. Metabolic imaging by hyperpolarized ^{13}C magnetic resonance imaging for in vivo tumor diagnosis. *Cancer Res*, 66(22):10855–10860, 2006.

[Golman *et al.*, 2006b] Klaes Golman, René Zandt, and Mikkel Thaning. Real-time metabolic imaging. *Proc Natl Acad Sci U S A*, 103(30):11270–11275, 2006.

[Gomori *et al.*, 1987] John M. Gomori, Robert I. Grossman, Charlotte Yu-Ip, and Toshio Asakura. NMR relaxation times in blood: Dependence on field strength, oxidation state, and cell integrity. *J Comput Assist Tomogr*, 11(4):684–690, 1987.

[Grant *et al.*, 2011] Aaron K. Grant, Elena Vinogradov, Xiaoen Wang, Robert E. Lenkinski, and David C. Alsop. Perfusion imaging with a freely diffusible hyperpolarized contrast agent. *Magn Reson Med*, 66(3):746–755, 2011.

[Greenberg *et al.*, 1995] NM Greenberg, F DeMayo, MJ Finegold, D Medina, WD Tilley, JO Aspinall, GR Cunha, AA Donjacour, RJ Matusik, and JM Rosen. Prostate cancer in a transgenic mouse. *Proc Natl Acad Sci U S A*, 92:3439–3443, April 1995.

[Gryff-Keller and Kubica, 2012] Adam Gryff-Keller and Dominika Kubica. Scalar relaxation of the second kind: A potential source of information on the dynamics of molecular movements. 1. investigation of solution reorientation of N-methylpyridone and 1,3-dimethyluracil using measurements of longitudinal relaxation rates in the rotating frame. *J Phys Chem A*, 116(39):9632–9638, 2012.

[Guyton, 1956] A. C. Guyton. *Textbook of Medical Physiology*. W. B. Saunders, 1956.

[Hahn, 1950] E. L. Hahn. Spin echoes. *Phys Rev*, 80:580–594, 1950.

[Han *et al.*, 2003] M. Han, A. W. Partin, M Zahurak, S. Piantadosi, J. I. Epstein, and P. C. Walsh. Biochemical (prostate specific antigen) recurrence probability following radical prostatectomy for clinically localized prostate cancer. *J Urol*, 169(2):517 – 523, 2003.

[Hennig *et al.*, 1986] J. Hennig, A. Nauerth, and H. Friedburg. RARE imaging: a fast imaging method for clinical MR. *Magn Reson Med*, 3:823–833, 1986.

[Hu *et al.*, 2008] S. Hu, M. Lustig, A. P. Chen, J. Crane, A. Kerr, D. A. C. Kelley, R. E. Hurd, J. Kurhanewicz, S. J. Nelson, John M. Pauly, and D. B. Vigneron. Compressed sensing for resolution enhancement of hyperpolarized ^{13}C flyback 3D-MRSI. *J Magn Reson*, 192(2):258–264, June 2008.

[Hu *et al.*, 2009] S. Hu, P. E. Larson, A. B. Kerr, D. A. C. Kelley, J. Tropp, J. M. Pauly, J. Kurhanewicz, and D. B. Vigneron. Application of HSn low peak B1 adiabatic refocusing pulses to hyperpolarized ^{13}C spectroscopic imaging applications. In *Proceedings of the 17th Annual Meeting of ISMRM*, page 333, Honolulu, 2009.

[Hu *et al.*, 2013] Simon Hu, Peder E.Z. Larson, Mark VanCriekinge, Andrew M. Leach, Ilwoo Park, Christine Leon, Jenny Zhou, Peter J. Shin, Galen Reed, Paul Keselman, Cornelius von Morze, Hikari Yoshihara, Robert A. Bok, Sarah J. Nelson, John Kurhanewicz, and Daniel B. Vigneron. Rapid sequential injections of hyperpolarized [1-^{13}C]pyruvate in vivo using a sub-kelvin, multi-sample DNP polarizer. *Magn Reson Imaging*, 31(4):490–496, 2013.

[Jezzard and Balaban, 1995] Peter Jezzard and Robert S. Balaban. Correction for geometric distortion in echo planar images from B_0 field variations. *Magn Reson Med*, 34(1):65–73, 1995.

[Johansson *et al.*, 2004a] E. Johansson, S. Mansson, R. Wirestam, J. Svensson, J.S. Petersson, K. Golman, and F. Stahlberg. Cerebral perfusion assessment by bolus tracking using hyperpolarized ^{13}C. *Magn Reson Med*, 51(3):464–472, 2004.

[Johansson *et al.*, 2004b] E. Johansson, L. E. Olsson, S. Mansson, J.S. Petersson, K. Golman, F. Stahlberg, and R. Wirestam. Perfusion assessment with bolus differentiation: A technique applicable to hyperpolarized tracers. *Magn Reson Med*, 52(5):1043–1051, 2004.

[Johansson *et al.*, 2004c] J. Johansson, O. Andren, and S. Andersson. Natural history of early, localized prostate cancer. *JAMA*, 291(22):2713–2719, 2004.

[Johnson *et al.*, 1972] WJ Johnson, WW Hagge, RD Wagoner, RP Dinapoli, and JW Rosevear. Effects of urea loading in patients with far-advanced renal failure. *Mayo Clin Proc*, 47(1):21–29., 1972.

[Josan *et al.*, 2011] Sonal Josan, Yi-Fen Yen, Ralph Hurd, Adolf Pfefferbaum, Daniel Spielman, and Dirk Mayer. Application of double spin echo spiral chemical shift imaging to rapid metabolic mapping of hyperpolarized [1-^{13}C]-pyruvate. *J Magn Reson*, 209(2):332 – 336, 2011.

[Kerr *et al.*, 2008] A. B. Kerr, P. E. Larson, M. Lustig, C. H. Cunningham, A. P. Chen, D. B. Vigneron, and J. M. Pauly. Multiband spectral-spatial design for high-field and hyperpolarized C-13 applications. In *Proceedings of the 16th Annual Meeting of ISMRM*, page 226, Toronto, 2008.

[Keshari *et al.*, 2013] Kayvan R. Keshari, Renuka Sriram, Mark Van Criekinge, David M. Wilson, Zhen J. Wang, Daniel B. Vigneron, Donna M. Peehl, and John Kurhanewicz.

Metabolic reprogramming and validation of hyperpolarized 13c lactate as a prostate cancer biomarker using a human prostate tissue slice culture bioreactor. *Prostate*, 73(11):1171–1181, 2013.

[Kettunen *et al.*, 2010] Mikko I Kettunen, De-En Hu, Timothy H Witney, Rebekah McLaughlin, Ferdia A Gallagher, Sarah E Bohndiek, Sam E Day, and Kevin M Brindle. Magnetization transfer measurements of exchange between hyperpolarized [1-^{13}C]pyruvate and [1-^{13}C]lactate in a murine lymphoma. *Magn Reson Med*, 63(4):872–880, 2010.

[Kettunen *et al.*, 2013] Mikko I. Kettunen, Brett W. C. Kennedy, De-en Hu, and Kevin M. Brindle. Spin echo measurements of the extravasation and tumor cell uptake of hyperpolarized [1-^{13}C]lactate and [1-^{13}C]pyruvate. *Magn Reson Med*, 70(5):1200–1209, 2013.

[Kim *et al.*, 2007] Seung-Jean Kim, K. Koh, M. Lustig, S. Boyd, and D. Gorinevsky. An interior-point method for large-scale l1-regularized least squares. *IEEE J Sel Top Signa*, 1(4):606–617, 2007.

[Koelsch *et al.*, 2013] Bertram L. Koelsch, Kayvan R. Keshari, Tom H. Peeters, Peder E. Z. Larson, David M. Wilson, and John Kurhanewicz. Diffusion MR of hyperpolarized ^{13}C molecules in solution. *Analyst*, 138:1011–1014, 2013.

[Kundel *et al.*, 1986] H. L. Kundel, B. Schlakman, P. M. Joseph, J. E. Fishman, and R. Summers. Water content and NMR relaxation time gradients in the rabbit kidney. *Invest Radiol*, 21(1):12–17, 1986.

[Kurhanewicz and Vigneron, 2008] John Kurhanewicz and Daniel B. Vigneron. Advances in MR spectroscopy of the prostate. *Magn Reson Imaging Clin N Am*, 16(4):697–710, 2008.

[Kurhanewicz *et al.*, 2011] John Kurhanewicz, Daniel B Vigneron, Kevin Brindle, Eduard Y Chekmenev, Arnaud Comment, Charles H Cunningham, Ralph J Deberardinis, Gary G Green, Martin O Leach, Sunder S Rajan, Rahim R Rizi, Brian D Ross, Warren S Warren, and Craig R Malloy. Analysis of cancer metabolism by imaging hyperpolarized nuclei: prospects for translation to clinical research. *Neoplasia*, 13(2):81–97, Feb 2011.

[Larson *et al.*, 2008] Peder E Z Larson, Adam B Kerr, Albert P Chen, Michael S Lustig, Matthew L Zierhut, Simon Hu, Charles H Cunningham, John M Pauly, John Kurhanewicz, and Daniel B Vigneron. Multiband excitation pulses for hyperpolarized ^{13}C dynamic chemical-shift imaging. *J Magn Reson*, 194(1):121–7, Sep 2008.

[Larson *et al.*, 2010] Peder E Z Larson, Robert Bok, Adam B Kerr, Michael Lustig, Simon Hu, Albert P Chen, Sarah J Nelson, John M Pauly, John Kurhanewicz, and Daniel B Vigneron. Investigation of tumor hyperpolarized [1-^{13}C]-pyruvate dynamics using time-resolved multiband RF excitation echo-planar MRSI. *Magn Reson Med*, 63(3):582–91, Mar 2010.

[Larson *et al.*, 2011] Peder E Z Larson, Simon Hu, Michael Lustig, Adam B Kerr, Sarah J Nelson, John Kurhanewicz, John M Pauly, and Daniel B Vigneron. Fast dynamic 3D MR spectroscopic imaging with compressed sensing and multiband excitation pulses for hyperpolarized ^{13}C studies. *Magn Reson Med*, 65(3):610–9, 2011.

[Larson *et al.*, 2012] P. E. Z. Larson, A. B. Kerr, G. D. Reed, R. E. Hurd, J. Kurhanewicz, J. M. Pauly, and D. B. Vigneron. Generating super stimulated-echoes in MRI and their application to hyperpolarized C-13 diffusion metabolic imaging. *IEEE T Med Imaging*, 31(2):265–275, 2012.

[Lau *et al.*, 2010] A. Z. Lau, A. P. Chen, N. R. Ghugre, V. Ramanan, W. W. Lam, K. A. Connelly, G. A. Wright, and C. H. Cunningham. Rapid multislice imaging of hyperpolarized ^{13}C pyruvate and bicarbonate in the heart. *Magn Reson Med*, 64(5):1323–31, 2010.

[Lau *et al.*, 2011] Angus Z Lau, Albert P Chen, Ralph E Hurd, and Charles H Cunningham. Spectral-spatial excitation for rapid imaging of DNP compounds. *NMR Biomed*, 24(8):988–996, 2011.

[Lee and Blaufox, 1985] H. B. Lee and M. D. Blaufox. Blood volume in the rat. *J Nucl Med*, 26(1):72–76, 1985.

[Leupold *et al.*, 2009] Jochen Leupold, Sven Månsson, J Stefan Petersson, Jürgen Hennig, and Oliver Wieben. Fast multiecho balanced SSFP metabolite mapping of ^{1}H and hyperpolarized ^{13}C compounds. *MAGMA*, 22(4):251–6, August 2009.

[Levin *et al.*, 2007] Y.S. Levin, D. Mayer, Y.-F. Yen, R.E. Hurd, and D.M. Spielman. Optimization of fast spiral chemical shift imaging using least squares reconstruction: Application for hyperpolarized ^{13}C metabolic imaging. *Magn Reson Med*, 58(2):245–252, 2007.

[Lupo *et al.*, 2010] Janine M Lupo, Albert P Chen, Matthew L Zierhut, Robert A Bok, Charles H Cunningham, John Kurhanewicz, Daniel B Vigneron, and Sarah J Nelson. Analysis of hyperpolarized dynamic ^{13}C lactate imaging in a transgenic mouse model of prostate cancer. *Magn Reson Imaging*, 28(2):153–62, Feb 2010.

[Luz and Meiboom, 1963] Z. Luz and S. Meiboom. Nuclear magnetic resonance study of the protolysis of trimethylammonium ion in aqueous solution - order of the reaction with respect to solvents. *J Chem Phys*, 39(2):366–370, 1963.

[Maril *et al.*, 2004] N. Maril, R Margalit, J. Mispelterand, and H. Degani. Functional sodium magnetic resonance imaging of the intact rat kidney. *Kidney Int*, 65:927–935, 2004.

[Maril *et al.*, 2006] N. Maril, Y. Rosen, G. H. Reynolds, A. Ivanishev, L. Ngo, and R. R. Lenkinski. Sodium MRI of the human kidney at 3 tesla. *Magn Reson Med*, 56:1229–1234, 2006.

[McConnell, 1958] H. M. McConnell. Reaction rates by nuclear magnetic resonance. *J Chem Phys*, 28(3):430–431, 1958.

[Mcneal *et al.*, 1986] John E. Mcneal, Robert A. Kindrachuk, Fuad S. Freiha, David G. Bostwick, Elise A. Redwine, and Thomas A. Stamey. Patterns of progression in prostate cancer. *Lancet*, 327(8472):60–63, 1986.

[Mehta *et al.*, 2004] S. S. Mehta, D. P. Lubeck, N. Sadetskly, D. J. Pasta, and P. R. Carroll. Patterns of secondary cancer treatment for biochemical failure following radical prostatectomy: Data from CaPSURE. *J Urol*, 171(1):215 – 219, 2004.

[Meiboom and Gill, 1958] S. Meiboom and D. Gill. Modified spin-echo method for measuring nuclear relaxation times. *Rev Sci Instrum*, 29:688–691, 1958.

[Merritt *et al.*, 2007] Matthew E Merritt, Crystal Harrison, Charles Storey, F Mark Jeffrey, A Dean Sherry, and Craig R Malloy. Hyperpolarized ^{13}C allows a direct measure of flux through a single enzyme-catalyzed step by NMR. *Proc Natl Acad Sci U S A*, 104(50):19773–7, Dec 2007.

[Meyer *et al.*, 1990] Craig J. Meyer, John M. Pauly, Albert Macovski, and Dwight G. Nishimura. Simultaneous spatial and spectral selective excitation. *Magn Reson Med*, 15(15):287–304, 1990.

[Meyer *et al.*, 1995] Marc-Etienne Meyer, Olivier Yu, Bernard Eclancher, Daniel Grucker, and Jacques Chambron. NMR relaxation rates and blood oxygenation level. *Magn Reson Med*, 34:234–241, 1995.

[Mugler and Altes, 2013] John P. Mugler and Talissa A. Altes. Hyperpolarized ^{129}Xe MRI of the human lung. *J Magn Reson Imaging*, 37(2):313–331, 2013.

[Nagashima, 2008] Kaz Nagashima. Optimum pulse flip angles for multi-scan acquisition of hyperpolarized NMR and MRI. *J Magn Reson*, 190(2):183 – 188, 2008.

[Nelson *et al.*, 2013] Sarah J. Nelson, John Kurhanewicz, Daniel B. Vigneron, Peder E. Z. Larson, Andrea L. Harzstark, Marcus Ferrone, Mark van Criekinge, Jose W. Chang, Robert Bok, Ilwoo Park, Galen Reed, Lucas Carvajal, Eric J. Small, Pamela Munster, Vivian K. Weinberg, Jan Henrik Ardenkjaer-Larsen, Albert P. Chen, Ralph E. Hurd, Liv-Ingrid Odegardstuen, Fraser J. Robb, James Tropp, and Jonathan A. Murray. Metabolic imaging of patients with prostate cancer using hyperpolarized [1-^{13}C]pyruvate. *Sci Transl Med*, 5(198):198ra108, 2013.

[Ohliger *et al.*, 2013] Michael A. Ohliger, Peder E.Z. Larson, Robert A. Bok, Peter Shin, Simon Hu, James Tropp, Fraser Robb, Lucas Carvajal, Sarah J. Nelson, John Kurhanewicz, and Daniel B. Vigneron. Combined parallel and partial fourier MR reconstruction for accelerated 8-channel hyperpolarized carbon-13 in vivo magnetic resonance spectroscopic imaging (MRSI). *J Magn Reson Imaging*, 38(3), 2013.

[Olsson *et al.*, 2006] Lars E. Olsson, Chun-Ming Chai, Oskar Axelsson, Magnus Karlsson, Klaes Golman, and J. Stefan Petersson. MR coronary angiography in pigs with intraarterial injections of a hyperpolarized ^{13}C substance. *Magn Reson Med*, 55(4):731–737, 2006.

[Páges *et al.*, 2013] G. Páges, M. Puckeridge, G. Liangfeng, Y. L. Tan, C Jacob, M. Garland, and P. W. Kuchel. Transmembrane exchange of hyperpolarized ^{13}C-urea in human erythrocytes: Subminute timescale kinetic analysis. *Biophys J*, 105:1956–1966, 2013.

[Park *et al.*, 2006] Jang-Yeon Park, Lance DelaBarre, and Michael Garwood. Improved gradient-echo 3D magnetic resonance imaging using pseudo-echoes created by frequency-swept pulses. *Magn Reson Med*, 55(4):848–857, 2006.

[Park *et al.*, 2010] Ilwoo Park, Peder E Z Larson, Matthew L Zierhut, Simon Hu, Robert Bok, Tomoko Ozawa, John Kurhanewicz, Daniel B Vigneron, Scott R Vandenberg, C David James, and Sarah J Nelson. Hyperpolarized ^{13}C magnetic resonance metabolic imaging: application to brain tumors. *Neuro-Oncology*, 12(2):133–44, Feb 2010.

[Pauly *et al.*, 1991a] J. Pauly, P. Le Roux, D. Nishimura, and A. Macovski. Parameter relations for the Shinnar-Le Roux selective excitation pulse design algorithm. *IEEE T Med Imaging*, 10(1):53–65, 1991.

[Pauly *et al.*, 1991b] J. Pauly, D. Nishimura, and A. Macovski. A k-Space analysis of small-tip-angle excitation. *J Magn Reson*, 81:43–56, 1991.

[Peterson *et al.*, 2011] E. T. Peterson, M. R. Smith, J. J. Grudzinski, J. W. Gordon, and S. B. Fain. Determination of optimal model sampling parameters for hyperpolarized contrast agents. In *Proceedings of the 19th Annual Meeting of ISMRM*, page 1518, Montreal, 2011.

[Potts *et al.*, 1992] Jennifer R. Potts, Brian T. Bulliman, and Philip W. Kuchel. Urea exchange across the human erythrocyte membrane measured using ^{13}C NMR lineshape analysis. *Eur Biophys J*, 21:207–216–65, 1992.

[Provotorov, 1962] B. N. Provotorov. *Sov Phys JETP*, 15:611, 1962.

[Purcell *et al.*, 1946] E. M. Purcell, H. C. Torrey, and R. V. Pound. Resonance absorption by nuclear magnetic moments in a solid. *Phys Rev*, 69:37–38, 1946.

[Rabi *et al.*, 1954] I. I. Rabi, N. F. Ramsey, and J. Schwinger. Use of rotating coordinates in magnetic resonance problems. *Rev Mod Phys*, 26:167–171, 1954.

[Reed *et al.*, 2014] G. D. Reed, C. von Morze, R. Bok, B. L. Koelsch, K. J. Smith, H. Shang, P. E. Z. Larson, J. Kurhanewicz, and D. B. Vigneron. High resolution ^{13}C MRI with hyperpolarized urea: *in vivo* T_2 mapping and ^{15}N labeling effects. *IEEE T Med Imaging*, 33(2):362–371, 2014.

[Reeder *et al.*, 2007] Scott B. Reeder, Jean H. Brittain, Thomas M. Grist, and Yi-Fen Yen. Least-squares chemical shift separation for ^{13}C metabolic imaging. *J Magn Reson Imaging*, 26(4):1145–1152, 2007.

[Reese *et al.*, 2003] T.G. Reese, O. Heid, R.M. Weisskoff, and V.J. Wedeen. Reduction of eddy-current-induced distortion in diffusion MRI using a twice-refocused spin echo. *Magn Reson Med*, 49(1):177–182, 2003.

[Rosset *et al.*, 2004] A. Rosset, L. Spadola, and O. Ratib. OsiriX: an open-source software for navigating in multidimensional DICOM images. *J Digit Imag*, 17:205–216, 2004.

[Sands, 1999] J. M. Sands. Regulation of renal urea transporters. *J Am Soc Nephrol*, 10:635–646, 1999.

[Scheffler, 2003] Klaus Scheffler. On the transient phase of balanced SSFP sequences. *Magn Reson Med*, 270:781–783, 2003.

[Schilling *et al.*, 2013] Franz Schilling, Stephan Duwel, Ulrich Kollisch, Markus Durst, Rolf F. Schulte, Steffen J. Glaser, Axel Haase, Angela M. Otto, and Marion I. Menzel. Diffusion of hyperpolarized ^{13}C-metabolites in tumor cell spheroids using real-time NMR spectroscopy. *NMR Biomed*, 26(5):557–568, 2013.

[Schroeder *et al.*, 2008] Marie A Schroeder, Lowri E Cochlin, Lisa C Heather, Kieran Clarke, George K Radda, and Damian J Tyler. In vivo assessment of pyruvate dehydrogenase flux in the heart using hyperpolarized carbon-13 magnetic resonance. *Proc Natl Acad Sci U S A*, 105(33):12051–6, Aug 2008.

[Schulte *et al.*, 2013] Rolf F. Schulte, Jonathan I. Sperl, Eliane Weidl, Marion I. Menzel, Martin A. Janich, Oleksandr Khegai, Markus Durst, Jan Henrik Ardenkjaer-Larsen, Steffen J. Glaser, Axel Haase, Markus Schwaiger, and Florian Wiesinger. Saturation-recovery metabolic-exchange rate imaging with hyperpolarized [1-^{13}C] pyruvate using spectral-spatial excitation. *Magn Reson Med*, 69(5):1209–1216, 2013.

[Sharp and Tolan, 1976] Robert R. Sharp and John W. Tolan. Nuclear magnetic relaxation of ^{119}Sn, ^{35}Cl, and ^{127}I in two symmetric top molecules, $SnCl_3I$ and SnI_3Cl, in liquid mixtures. *J Chem Phys*, 65(2):522–530, 1976.

[Siegel *et al.*, 2012] Rebecca Siegel, Deepa Naishadham, and Ahmedin Jemal. Cancer statistics, 2012. *CA Cancer J Clin*, 62(1):10–29, 2012.

[Smith *et al.*, 2012] M.R. Smith, E.T. Peterson, J.W. Gordon, D.J. Niles, I.J. Rowland, K.N. Kurpad, and S.B. Fain. In vivo imaging and spectroscopy of dynamic metabolism using simultaneous ^{13}C and ^{1}H MRI. *IEEE T Bio-Med Eng*, 59(1):45–49, Jan 2012.

[Sonnenberg and Wilson, 1981] H. Sonnenberg and D. R. Wilson. Urea handling by the medullary collecting duct of the rat kidney during hydropenia and urea infusion. *Pflugers Arch*, 390(2):131–137, 1981.

[Svensson *et al.*, 2003] J Svensson, S Mansson, E Johansson, J S Petersson, and L E Olsson. Hyperpolarized ^{13}C MR angiography using TrueFISP. *Magn Reson Med*, 50(2):256–262, 2003.

[Tannus and Garwood, 1996] JA Tannus and M Garwood. Improved performance of frequency-swept pulses using offset-independent adiabaticity. *J Magn Reson A*, 120(2):133–137, 1996.

[Thulborn *et al.*, 1982] Keith R. Thulborn, John C. Waterton, Paul M. Matthews, and George K. Radda. Oxygenation dependence of the transverse relaxation time of water protons in whole blood at high field. *Biochim Biophys Acta*, 714:265–270, 1982.

[Tropp *et al.*, 2011] James Tropp, Janine M. Lupo, Albert Chen, Paul Calderon, Don McCune, Thomas Grafendorfer, Esin Ozturk-Isik, Peder E.Z. Larson, Simon Hu, Yi-Fen Yen, Fraser Robb, Robert Bok, Rolf Schulte, Duan Xu, Ralph Hurd, Daniel Vigneron, and Sarah Nelson. Multi-channel metabolic imaging, with SENSE reconstruction, of hyperpolarized [1-^{13}C] pyruvate in a live rat at 3.0 Tesla on a clinical MR scanner. *J Magn Reson*, 208(1):171 – 177, 2011.

[ure, 2005] Final report of the safety assessment of urea. *Int J Toxicol*, 24(3 suppl):1–56, 2005.

[von Morze *et al.*, 2011a] Cornelius von Morze, Peder E Z Larson, Simon Hu, Kayvan Keshari, David M Wilson, Jan Henrik Ardenkjær-Larsen, Andrei Goga, Robert Bok, John Kurhanewicz, and Daniel B Vigneron. Imaging of blood flow using hyperpolarized [^{13}C]urea in preclinical cancer models. *J Magn Reson Imaging*, 33(3):692–7, Mar 2011.

[von Morze *et al.*, 2011b] Cornelius von Morze, Galen Reed, Peter Shin, Peder E Z Larson, Simon Hu, Robert Bok, and Daniel B Vigneron. Multi-band frequency encoding method for metabolic imaging with hyperpolarized [1-^{13}C]pyruvate. *J Magn Reson*, 211(2):109–13, Aug 2011.

[von Morze *et al.*, 2012] Cornelius von Morze, Robert A. Bok, Jeff M. Sands, John Kurhanewicz, and Daniel B. Vigneron. Monitoring urea transport in rat kidney in vivo using hyperpolarized ^{13}C magnetic resonance imaging. *Am J Physiol-Renal*, 302(12):F1658–F1662, 2012.

[Wei *et al.*, 2002] John T. Wei, Rodney L. Dunn, Howard M. Sandler, P. William McLaughlin, James E. Montie, Mark S. Litwin, Linda Nyquist, and Martin G. Sanda. Comprehensive comparison of health-related quality of life after contemporary therapies for localized prostate cancer. *J Clin Oncol*, 20(2):557–566, 2002.

[Weinreb *et al.*, 2009] Jeffrey C. Weinreb, Jeffrey D. Blume, Fergus V. Coakley, Thomas M. Wheeler, Jean B. Cormack, Christopher K. Sotto, Haesun Cho, Akira Kawashima, Clare M. Tempany-Afdhal, Katarzyna J. Macura, Mark Rosen, Scott R. Gerst, and John Kurhanewicz. Prostate cancer: Sextant localization at MR imaging and MR spectroscopic imaging before prostatectomyresults of ACRIN prospective multi-institutional clinicopathologic study. *Radiology*, 251(1):122–133, 2009.

[Whittall and MacKay, 1989] Kenneth P Whittall and Alexander L MacKay. Quantitative interpretation of NMR relaxation data. *J Magn Reson*, 84(1):134 – 152, 1989.

[Wild *et al.*, 2006] Jim M. Wild, Kevin Teh, Neil Woodhouse, Martyn N.J. Paley, Stan Fichele, Nicola de Zanche, and Larry Kasuboski. Steady-state free precession with hyperpolarized ^{3}He: Experiments and theory. *J Magn Reson*, 183(1):13 – 24, 2006.

[Wind *et al.*, 1985] R. A. Wind, M. J. Duljvestlicn, C. van der Lugt, A. Manenschijn, and J. Vriend. Applications of dynamic nuclear polarization in ^{13}C NMR in solids. *Progr Nucl Magn Reson Spectrosc*, 17:33–67, 1985.

[Witney *et al.*, 2011] Timothy H. Witney, Mikko I. Kettunen, and Kevin M. Brindle. Kinetic modeling of hyperpolarized ^{13}C label exchange between pyruvate and lactate in tumor cells. *J Biol Chem*, 286(28):24572–24580, 2011.

[Yen *et al.*, 2009] Y-F. Yen, S.J. Kohler, A.P. Chen, J. Tropp, R. Bok, J. Wolber, M.J. Albers, K.A. Gram, M.L. Zierhut, I. Park, V. Zhang, S. Hu, S.J. Nelson, D.B. Vigneron, J. Kurhanewicz, H.A.A.M Dirven, and R.E. Hurd. Imaging considerations for in vivo ^{13}C metabolic mapping using hyperpolarized ^{13}C-pyruvate. *Magn Reson Med*, 62(1):1–10, 2009.

[Yen *et al.*, 2010] Yi-Fen Yen, Patrick Le Roux, Dirk Mayer, Randy King, Daniel Spielman, James Tropp, Kim Butts Pauly, Adolf Pfefferbaum, Shreyas Vasanawala, and Ralph Hurd. T_2 relaxation times of ^{13}C metabolites in a rat hepatocellular carcinoma model measured in vivo using ^{13}C-MRS of hyperpolarized [1-^{13}C]pyruvate. *NMR Biomed*, 23(4):414–423, 2010.

[Zhao *et al.*, 1996] L. Zhao, R.V. Mulkern, C.H. Tseng, D. Williamson, S. Patz, R. Kraft, R.L. Walsworth, F.A. Jolesz, and M.S. Albert. Gradient-echo imaging considerations for hyperpolarized ^{129}Xe MR. *J Magn Reson B*, 113(2):179–183, 1996.

[Zierhut *et al.*, 2010] Matthew L Zierhut, Yi-Fen Yen, Albert P Chen, Robert Bok, Mark J Albers, Vickie Zhang, Jim Tropp, Ilwoo Park, Daniel B Vigneron, John Kurhanewicz, Ralph E Hurd, and Sarah J Nelson. Kinetic modeling of hyperpolarized $^{13}C_1$-pyruvate metabolism in normal rats and TRAMP mice. *J Magn Reson*, 202(1):85–92, 2010.

Publishing Agreement

It is the policy of the University to encourage the distribution of all theses, dissertations, and manuscripts. Copies of all UCSF theses, dissertations, and manuscripts will be routed to the library via the Graduate Division. The library will make all theses, dissertations, and manuscripts accessible to the public and will preserve these to the best of their abilities, in perpetuity.

Please sign the following statement:

I hereby grant permission to the Graduate Division of the University of California, San Francisco to release copies of my thesis, dissertation, or manuscript to the Campus Library to provide access and preservation, in whole or in part, in perpetuity.

March 31 2014

Author Signature | Date